POLITECNICO
MILANO 1863

SCUOLA DI INGEGNERIA INDUSTRIALE
E DELL'INFORMAZIONE

Optical Properties of Germanium-Vacancy Centers in Diamonds Produced by Ion Implantation and Annealing Treatment

TESI DI LAUREA MAGISTRALE IN
ENGINEERING PHYSICS - INGEGNERIA FISICA

Author: **Francesco Maruca**

Student ID: 971697
Advisor: Prof. Roberto Osellame
Co-advisors: Prof. Fedor Jelezko, Dr. Lev Kazak
Academic Year: 2022-23

Abstract

A solid-state system combining a stable spin degree of freedom with an efficient optical interface is highly desirable as an element for integrated quantum optical and quantum information systems. Due to their properties, negatively charged group-IV color centers in diamond are appealing for quantum communication and computing purposes. In particular, Germanium-Vacancy centers are bright color centers in diamond with significant optical properties and controllable electronic spin states. They have remarkable features, such as large ground state splitting, high fluorescence yield and long coherence time at cryogenic temperatures. Moreover, they are promising candidates for integration with nanophotonic devices. One reliable technique to produce Germanium-Vacancy centers in diamond is ion implantation, followed by annealing treatment. However, implantation introduces lattice damage, which influences the properties of Germanium-Vacancy. Annealing treatment after implantation can be utilized to recover the damage. A critical challenge lies in identifying effective annealing parameters to repair the lattice. In the present work, an optical spectroscopy study of Germanium-Vacancy color centers is presented. The impact of annealing conditions, i.e., temperature and duration of the treatment, and implantation parameters on the optical properties of the formed centers is discussed.

Keywords: Diamonds, color centers, Germanium-Vacancy centers, ion implantation, annealing

Abstract in lingua italiana

Un sistema a stato solido che combini un grado di libertà di spin stabile con un'interfaccia ottica efficiente è altamente auspicabile come elemento per sistemi integrati di ottica quantistica e di informazione quantistica. Grazie alle loro proprietà, i centri di colore del gruppo IV carichi negativamente nel diamante sono interessanti per scopi di comunicazione e informatica quantistica. In particolare, i centri Germanio-Vacanza sono centri di colore brillanti nel diamante con proprietà ottiche significative e stati elettronici di spin controllabili. Hanno caratteristiche notevoli, come ampia separazione dello stato fondamentale, elevato rendimento di fluorescenza e lungo tempo di coerenza a temperature criogeniche. Inoltre, sono candidati promettenti per l'integrazione con dispositivi nanofotonici. Una tecnica affidabile per produrre centri Germanio-Vacanza nel diamante è l'impiantazione ionica, seguita da un trattamento di ricottura. Tuttavia, il processo di impiantazione ionica introduce danni nel reticolo, che influiscono sulle proprietà dei centri Germanio-Vacanza. Il trattamento di ricottura seguente all'impiantazione può essere utilizzato per riparare tali danni. Una sfida critica consiste nell'individuare parametri di ricottura efficaci per riparare il reticolo. Nel presente lavoro viene presentato uno studio di spettroscopia ottica di centri di colore Germanio-Vacanza. Viene discusso l'impatto delle condizioni di ricottura, cioè temperatura e durata del trattamento, e dei parametri di impiantazione ionica sulle proprietà ottiche dei centri formati.

Parole chiave: Diamanti, centri di colore, centri Germanio-Vacanza, impiantazione ionica, ricottura

Contents

Introduction

Quantum information processing is expected to give a considerable advantage over classical computers. In this context, over the past two decades color centers in diamond have emerged as promising systems for a variety of quantum applications [1–20]. These impurities are optically active and fluoresce in the visible spectrum, whence the name "color centers". Group-IV defects in diamond have gained considerable interest in the field of quantum information, as they fulfill essential criteria for quantum nodes in a quantum network [21–25]. These defects offer an efficient spin-photon interface and the potential for long coherence times making them highly promising candidates [26].

The present thesis describes the investigation of the Germanium-Vacancy (GeV) center in diamond. A systematic examination of the optical properties of Germanium-Vacancy centers is presented. Specifically, the influence of implantation energies and annealing temperatures on the characteristics of these defects are investigated. The main goal is establishing a reliable method for producing high-quality GeV defects in diamond through ion implantation of germanium ions and subsequent annealing treatments, and drive their development to applications. Ion implantation is a promising technique for deterministic creation of Germanium-Vacancy defects. However, the process also results in damage produced in the diamond lattice. Annealing is a crucial step as it is expected to repair the lattice damage inflicted during the ion implantation process. Thus, particular attention is given to understanding how the properties of the produced centers change depending on the chosen parameters for ion implantation and annealing. For this purpose, the optical properties of the created GeV centers are probed using photoluminescence spectroscopy, Photoluminescence Excitation (PLE) and lifetime measurements conducted at both room and cryogenic temperatures.

The present work is organized as follows:

- Chapter 1 illustrates theoretical ideas and concepts regarding diamond as a host lattice for color centers, color centers fabrication strategies, Single Molecule Spectroscopy and group-IV defects in diamond, mainly focusing on the Germanium-Vacancy defect.

- Chapter 2 presents the investigated diamond samples as well as the utilized experimental methods, setups and equipment.

- Chapter 3 reports on the performed experimental investigations of Germanium-Vacancy defects, that is: photoluminescence spectroscopy, Photoluminescence Excitation spectroscopy and excited state lifetime spectroscopy.

- Chapter 4 summarizes the essential results of the work and provides an outlook on future developments.

1 | Theoretical background

1.1. Diamond as a host lattice

Diamond is a promising material for a variety of applications in science and technology. Notably, it is gaining interest due to the presence of color centers, which are optically active impurities in the diamond lattice. Color centers in diamond benefit from the physical properties of the diamond itself, e.g., transparency to visible light, chemical inertness and high thermal conductivity. This section is focused on discussing the general properties of diamonds. A classification of different types of diamond is given. Finally, diamond and color centers fabrication processes are presented.

1.1.1. General properties of diamond

Diamond is a metastable allotrope of carbon at room temperature and atmospheric pressure, in contrast to graphite which is the stable allotrope under those conditions. In nature diamond is formed only in high temperature and high pressure conditions. Diamonds can also be produced artificially by means of various growth techniques, e.g., High-Pressure and High-Temperature and Chemical Vapor Deposition growth.

With respect to the crystalline structure, the primitive (Bravais) cell of diamond is a Face-Centered Cubic (FCC) lattice unit cell with a two atom basis, where one carbon atom is located at the $(0, 0, 0)$ lattice position and the second at the $(1/4, 1/4, 1/4)$ position, with a lattice constant at room temperature of 3.567 Å [27]. In other words, those two carbon atoms act as origins for two interpenetrating FCC sublattices. The diamond lattice is shown in figure 1.1: atoms belonging to the two interpenetrating sublattices are depicted in black and blue, respectively. The bonds between carbon atoms are illustrated as grey rods, revealing the tetrahedral structure. The atoms are connected by covalent bonds along the $\langle 111 \rangle$ crystallographic direction and its permuted axes. This crystal structure belongs to the O_h^7 space group. In diamond, the carbon atoms have sp^3 hybridized orbits in comparison to the sp^2 hybridization of graphite or fullerene. This hybridization leads diamond to have the highest hardness among known materials. The strong bonds also

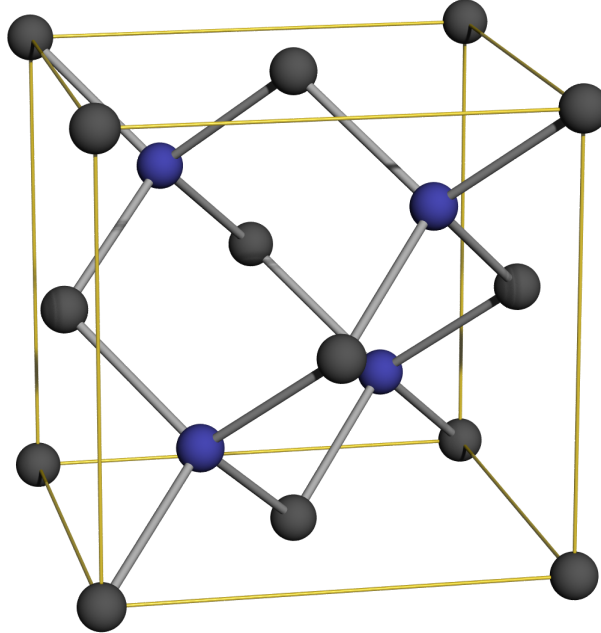make it resistant against oxidation and disintegration by acids, so diamond has a high chemical inertness.

Figure 1.1: Diamond lattice with the two FCC sublattices depicted in black and blue, the tetrahedral sp^3 bonds are depicted in grey. The lattice constant for each FCC sublattice is 3.567 Å, the length of the bonds is 1.54 Å [27].

The diamonds have a high electrical bandgap of 5.5 eV at room temperature [27], and they are classified as indirect semiconductors. The large bandgap makes diamond transparent for a broad range of radiation. However, in most diamonds, natural and synthetic, optical properties, such as absorption, are determined by the dominating defects and impurities contained in the diamond lattice. Moreover, the properties of the diamond lattice itself should be taken into account in order to comprehend why it is well suited as host environment for color centers, whose features are influenced by their surroundings. These properties are: refractive index, reflectivity, vibrational properties and thermal conductivity.

Refractive index n. The average of the refractive index n over the visible spectrum is 2.418 for diamond. The value of n varies from 2.463 at 400 nm in ultraviolet to 2.400 at 800 nm in infrared [28], whereas variations of n due to different types of diamond are negligible. An equally important parameter is the dispersion, $dn/d\lambda$, i.e., the dependence of the refractive index on wavelength λ

$$\frac{dn}{d\lambda} = -8.5 \cdot 10^{-5} \text{ nm}^{-1}. \tag{1.1}$$

It is also important to know the temperature T dependence, as well as the pressure P dependence of the refractive index. The general temperature dependence at constant pressure (or thermo-optical coefficient) and pressure dependence at constant temperature of the refractive index of diamond can be expressed as [28]

$$\left(\frac{1}{n}\right)\left(\frac{dn}{dT}\right)_P = 4.04 \cdot 10^{-6} \text{ K}^{-1}, \tag{1.2}$$

$$\left(\frac{1}{n}\right)\left(\frac{dn}{dP}\right)_T = -0.36 \cdot 10^{-12} \text{ Pa}^{-1}. \tag{1.3}$$

Equations 1.2 and 1.3 show that the refractive index of diamond varies negligibly both with temperature and with pressure. For example, in the far-infrared regime, at 300 K the index is $n = 2.38767$, while at 5.5 K it is $n = 2.38668$ [29], which demonstrates negligible changes. The behavior is similar in the other regions of the electromagnetic spectrum.

Reflectivity R. In microscopy and spectroscopy experiments the reflectivity as property of the diamond has to be considered, since it determines how much of the excitation power gets reflected and how much is transmitted. Therefore, it determines the excitation power at the position of the color centers. The typical range of wavelengths used in spectroscopic investigations of color centers in diamond is between 400 nm and 800 nm, in the visible range. At 400 nm the reflectivity of diamond is $R_{400} = 0.1785$, whereas at 800 nm it is $R_{800} = 0.1690$ [28], meaning that transmission of IR/red light is higher than for shorter wavelengths.

Vibrational properties. Phonon signatures can affect the spectroscopic investigations of color centers. Hence, it is important to distinguish phonons of the diamond crystal from the modes of the color centers. The estimation of the energy of phonons in the diamond lattice can be done based on the Debye model. According to the model, the Debye temperature Θ_D is

$$\Theta_D = \frac{\hbar \omega_D}{k_B}, \tag{1.4}$$

Where $\hbar$ is the Planck reduced constant, ω_D is the vibrational frequency of the phonons in the lattice and k_B the Boltzmann constant. The Debye temperature of diamond is $\Theta_D = 1860$ K [28]. This leads to a high vibrational energy of $E_D = \hbar \omega_D = 160.28$ meV

[28], and gives an upper limit for the energy of phonons in the diamond lattice. The phonon signatures have to be taken into account when side band features of any color center are studied. Note that multi-phonon peaks might have higher energies than the estimated upper limit [28].

Thermal conductivity. The thermal conductivity is a fundamental property of the diamond. The above mentioned phonons transport a significant amount of heat. Due to this, the thermal conductivity of diamond is very high and equal to 2200 $Wm^{-1}K^{-1}$ at room temperature [28]. In comparison, the thermal conductivity of copper is only equal to 400 $Wm^{-1}K^{-1}$ and for silver it is 420 $Wm^{-1}K^{-1}$. The high value of thermal conductivity implies that cooling and heating of diamond are very fast during the experiments.

1.1.2. Classification of different types of diamond

In nature diamonds do not occur in a chemically pure state: they always contain different impurity atoms. The presence of the impurities impacts on various properties of diamonds, e.g., optical absorption. The classification of diamonds is based on the type and amount of contained impurities. Historically, the first classification of diamonds was reported in [30], considering absorption as key parameter. A more recent classification is given in [31] based on the optical absorption of nitrogen, boron and hydrogen related defects and paramagnetic absorption of single substitutional nitrogen atoms. Diamonds are classified as type I or type II.

Type I. About 98% of natural available diamonds are classified as type I. The optical and paramagnetic absorption of type I diamonds are dominantly caused by P1 centers (substitutional nitrogen atoms). A typical density of nitrogen in type I diamond is of 200 to 4000 ppm. Further, in type I diamonds nitrogen defects are distributed non-uniformly. The authors in [32] reported that nitrogen atoms group to approximately 10 atoms per group (estimated by means of point-defect scattering experiments). A more precise estimate is given by IR spectroscopy [28].

Sub-classes of type I diamond are additionally labeled with a, b or c. Type Ia comprises diamonds containing substitutional N in form of non-paramagnetic aggregates, with concentrations of about 500 ppm up to 3000 ppm [28]. Type Ib diamonds contain a dominating amount of substitutional single nitrogen atoms, which are paramagnetic. This class was first discovered by means of IR absorption and reported in [31]. Typically, natural type Ib diamonds contain 40 to 100 ppm of nitrogen, whereas synthetic type Ib diamonds exhibit 300 ppm in nitrogen content. Most synthetic diamonds belong to the type Ib class. The majority (80%) of the nitrogen atoms in type Ib diamonds are located throughout

the crystal in isolated sites. The main optical characteristic of type Ib diamond occurs in the absorption spectra, that show a continuum for wavelengths below 500 nm [28]. Type Ic diamonds contain a high concentration of dislocations. Notably, type Ic does not relate to nitrogen. The main optical characteristics for this class are an absorption continuum below 900 nm and an absorption peak at 560 nm. IR characteristics are similar to type Ia diamonds [28].

Type II. Diamonds of this type do not show any optical and/or paramagnetic absorption related to nitrogen defects. Historically, type II diamonds were the ones showing optical transparency for wavelengths $\leq$ 230 nm [30]. The concentration of nitrogen in type II diamonds is typically below 1 ppm.

As for type I, diamonds of type II are sub-classified by IR absorption features. Type IIa diamonds show no specific IR absorption related to boron and hydrogen impurities and have the highest optical transparency among all diamond classes. A characteristic spectral feature is fundamental optical absorption continuum below 220 nm. Usually, diamonds with a nitrogen concentration below 1 ppm are classified as type IIa [28]. Type IIb comprises diamonds which show boron impurity-related optical absorption. Opposite to type IIa, which show an increasing absorption towards shorter wavelengths, for type IIb the absorption increases in the longer wavelengths range. Typically, natural type IIb diamonds exhibit a boron concentration lower than 10^{17} cm^{-1}, whereas synthetic type IIb diamonds can reach a boron concentration of 10^{20} cm^{-1}. Type IIc comprises diamonds with dominating hydrogen impurity-related absorption.

1.1.3. Introduction to different diamond fabrication processes

In nature, diamonds are formed in the upper mantle of the Earth, in an environment which features pressures around 70-80 kbar and temperatures around 1400-1600 °C [27]. The properties of natural diamonds depend on the environment and the growth conditions. As a consequence, the impurity incorporation is not uniform in natural diamonds, which are not reproducible in terms of impurities (and therefore color centers) concentration. For the scientific purposes, however, it is vital to have control on the impurity incorporation. In order to achieve it, several techniques were developed for the growth of diamond. In the following, a brief overview on diamond synthesis methods is given. Details from [33–35] are included.

High-Pressure High-Temperature diamonds. The first method that was developed to synthesize diamonds is called High-Pressure and High-Temperature (HPHT), based on the work of [36]. In this process, temperature and pressure conditions similar to

the ones of the natural growth process are utilized. This process can be described by taking into account the phase diagram of carbon, shown in figure 1.2, where the regions of natural stability of graphite/diamond and the two regions for technical synthesis of diamond, corresponding to HPHT and CVD (see below for details on CVD) respectively, are highlighted. In HPHT growth, a material containing carbon is placed inside a reactor and exposed to pressures and temperatures greater than 5 GPa and 1500 °C. In that region, diamond is a thermodynamically stable phase of carbon. However, in synthesizing diamond, kinetics plays an important role as well and, therefore, other parameters have to be taken into account. The energy that is needed to convert graphite into diamond is significant. This so called "solid to solid" transformation requires high temperature and pressure, which can be technically realized by means of different systems [36–38].

Synthesizing diamonds is possible in two ways: static and dynamic compression. In the static compression method, pressures up to 8-20 GPa and temperatures of 1000-3000 °C are required. Diamonds that are produced in this way have sizes smaller than 20 μm unless seed crystals are used and are hexagonal or cubic (typical diamond) [35]. In the dynamic compression technique, instead, the carbon source is loaded in a heating chamber and through the loading the pressure reaches 7 to 150 GPa. The loading time is in the order of microseconds. However the diamonds produced by this procedure are quite small and have a grain size lower than 100 nm [35].

The operating temperature can be reduced by addition of specific catalysts such as metals belonging to the group VIII of the periodic table (e.g., Fe, Co, Ni, etc.). In HPHT with catalyst the diamond is built up in a thermodynamically stable regime by using a locally carbon-rich melt. In this procedure one takes advantage of the fact that carbon and the used catalyst have eutectic relation. At a certain temperature and pressure the carbon is still solid, but the catalyst melts. Hence, diamond can be synthesized in lower temperature and pressure conditions with respect to the methods considered before. The growth of diamond in such a catalyst melt is possible because the chemical potential of graphite is much higher than for diamond. So graphite gets ablated more easily than diamond.

A major advantage of this HPHT method is the significant degree of control over the geometry and the quality of the diamond which is grown, as well as high yield of diamond material at relatively low costs. Most diamonds produced by the HPHT method are type Ib, but with the help of special selected getter mixtures (e.g., containing Ti, Al or Zn) one can obtain diamonds of type IIa by binding nitrogen to getter elements [39, 40]. With longer controlled periods of growth one can produce diamonds of sizes up to 8 mm [35].

Chemical Vapor Deposited diamonds. The method of Chemical Vapor Deposition (CVD) operates in a regime where graphite, not diamond, is the stable phase of carbon, as shown in figure 1.2. In this case, the actual process of building diamond is not driven by the thermodynamics of the system, but by the chemical dynamics.

This process requires a substrate material in order to grow a diamond. Typical substrate materials are Si, Mo, W, Ti, quartz, sapphire and diamond. The seed substrate is a small single crystal, usually immersed in a hydrogen and hydrocarbons gas mixture. Operating regimes are at temperatures of the substrate around 800 °C and pressures up to 1000 Pa. The growth starts with injecting the gas mixture heated up to 2000 K. The gas heating can be provided by a microwave plasma [41], a hot filament [42], an arc discharge [43], a welding torch, a laser, an electron beam, etc. Above 800 °C the mixture ionizes to chemically active radicals. The formed plasma reacts with the substrate and the diamond crystal starts to grow. The synthesis is performed with approximately 5% of carbon in the gas mixture [35]. To supply the carbon content CH_4 or C_2H_6 are used. Additional gases or elements can be added for explicit doping. Diamond is then produced through the decomposition of the hydrocarbons on the substrate, which has a temperature of 800 to 900 °C. During the process, both diamond and graphite are grown, but graphite gets etched by the hydrogen plasma. The same applies to the impurities that must be incorporated in the grown diamond. Thus, they have to be bound more strongly to the diamond lattice than graphite.
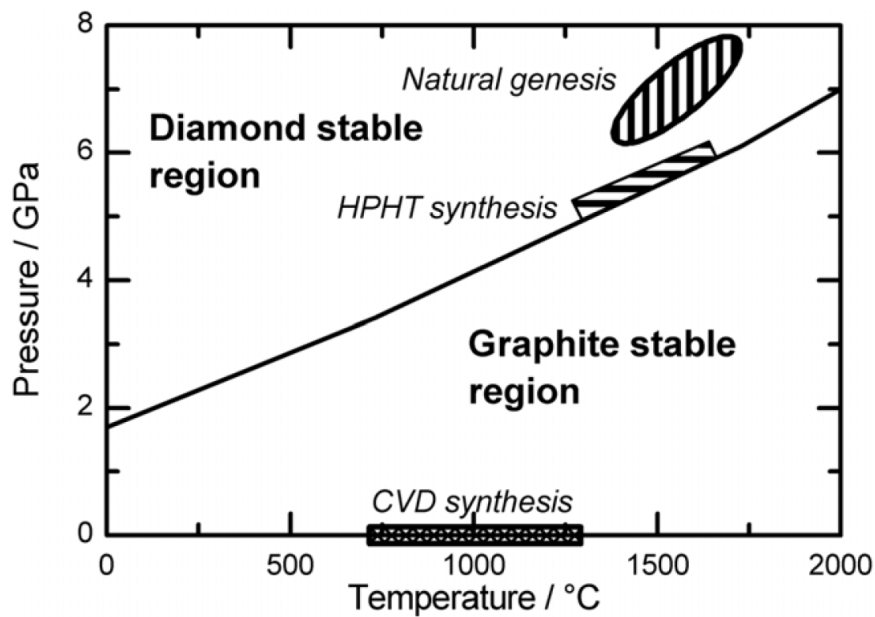

Figure 1.2: Phase diagram of carbon [34]. The regions for natural genesis, HPHT and CVD growth are highlighted.

The properties of the produced diamonds can be controlled by the choice of the substrate, the temperature of the plasma and the composition of the gases. With a change of the substrate one can control the diamond to be a single crystal or a polycrystal. Growth of a single crystal diamond is possible only when diamond itself is used as a substrate. The new diamond is then formed by homoepitaxial growth. The polycrystal growth, instead, is highly non-uniform in size and composition. CVD synthesized diamonds can reach lateral dimensions up to 90 mm [44]. The benefit of the CVD process is the possibility to grow large area diamonds. A disadvantage of this growth technique compared to HPHT is instead the higher cost. CVD synthetic diamonds are typically type IIa.

1.1.4.   Color centers fabrication strategies

In the present work, the major aspect to be addressed is the development of methods for the deterministic and ideally scalable fabrication of Germanium-Vacancy defects in diamond. Color centers are most commonly produced through either impurity incorporation during synthesis or via targeted ion implantation and subsequent annealing treatment.

Incorporation. Artificial synthesis of diamond is the first step towards optical or electrical applications of this material, as color centers can be formed during the growth process. For HPHT diamonds it is possible to incorporate impurity elements such as germanium through the addition of suitable germanium-containing precursors [45, 46], but this procedure mostly results in an arbitrary spatial distribution of the impurity atoms. It is also possible to incorporate impurity atoms during CVD diamond growth by controlling the gas mixture and related parameters, such as temperature and pressure. However, one of the main challenges of impurity incorporation during synthesis is demonstrating controlled growth of single emitters using HPHT and CVD growth [46].

Ion implantation. Another technique commonly used to incorporate impurity atoms into a diamond sample is ion implantation. The diamond target is exposed to an ion beam, allowing doping with varieties of different impurities [46]. Technically it can be realized with different ion sources, e.g., gas or solid state [47].

A scheme for the process utilizing a gas source is shown in figure 1.3a and it consists in generating an atomic beam from a gas mixture. The standard method is electron ionization: the gas mixture molecules are bombarded by electrons to produce ions, that are subsequently extracted by means of an acceleration field. The second method is shown in figure 1.3b and it is based on collision ionization. In this case, the atomic beam is used to obtain the impurity elements from a powder source (cathode).

Independent of the source, after the beam creation a mass filtering section is utilized to

enable control of isotope and ion choice for the impurity elements to be implanted. The filter contains two main components. The first part is built up with a capacitor embedded in a magnetic field. The second component is a basis slit apparatus to block undesired atoms. The sections placed after the mass filtering serve as focusing and beam steering elements, utilized to focus and change the direction of the beam.

Implantation critical parameters are dose and energy of the implanted ions. A great benefit of the implantation technique is that it gives the possibility to locate impurities at specific regions of the sample. The depth of the implanted impurities is defined by the kinetic energy of the ions in the target sample. The density of implanted ions is controlled by variation of the ion flux and implantation time, i.e., dose. However, this method has several limitations, the main one being that the ion beam has stochastic nature and straggling of the ions (i.e., scattering of the ions as they travel through the target material) takes place, hindering the deterministic implantation of impurity ions [46]. Straggling can be handled by reducing the implantation energy, but at the cost of lower creation yield of impurities. The authors in [48] report creation yields of Nitrogen-Vacancy (NV) centers in diamond which scale with implantation energy.
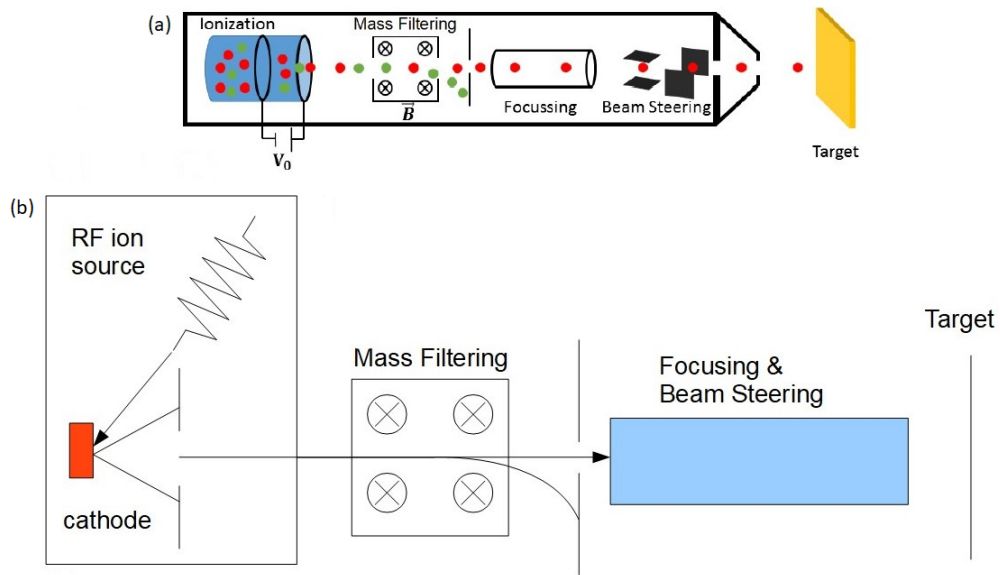

Figure 1.3: Schematic illustration of the ion implantation process [47]. (a) shows ion implantation with a gas source. The gas contains the desired impurity atoms. (b) differs in ion source. A Radio Frequency (RF) source accelerates light atoms targeted at a cathode, which contains the implantation element in compressed powder form. By means of impact ionization the implantation element atoms get accelerated and an ion beam is created. Spatial manipulation and element selection can be the same both in (a) and (b).

Annealing. In materials science, annealing is a heat treatment that can alter the physical and chemical properties of a material. It involves heating a material above its recrystallization temperature, maintaining a suitable temperature for an appropriate amount of time and then cooling. During the process, vacancies (i.e., point defects in a crystal where an atom is missing from one of the lattice sites) migrate in the crystal lattice and the number of dislocations decreases. As the material cools down, it recrystallizes.

Annealing has fundamental importance in producing high quality color centers in diamond [46, 49]. Many color centers in diamond, such as Germanium-Vacancy, Silicon-Vacancy, etc., consist of a foreign atom and a split vacancy. To create such defects, simple doping of the diamond is not sufficient. The annealing process activates the vacancies and increases the probability that they reach the impurity atoms. The vacancies will then be able to bind to the impurity atoms, to form the desired defects [46, 50]. At the same time, annealing is a common strategy to reduce the damage produced in the diamond lattice (created, for instance, by the ion implantation process), resulting in even better features of the obtained color centers [46, 49, 50].

1.2. Single Molecule Spectroscopy

Spectroscopy of color centers in diamond could be performed on the basis of Single Molecule Spectroscopy (SMS). This is a technique developed relatively recently for fluorescence spectroscopy, which allows experimental access to physical properties of optically active individual molecules or atoms [51]. The first low temperature experimental detection of single molecules was reported in [52], where experiments on pentacene molecules substitutionally doped into p-terphenyl at low temperature were performed. Later, the development of SMS created the opportunity to study color centers in diamonds. Nitrogen-related defects were first chosen and examined [53].

Optical excitation of molecules embedded in a host material leads to fluorescence. The typical fluorescence spectrum consists in two main components: the Zero Phonon Line (ZPL) and the Phonon Sideband (PSB). Together, ZPL and PSB constitute the fluorescence signature of individual light absorbing and emitting molecules. Both features in the recorded spectra result from electromagnetic transitions between an excited state and the ground state of the investigated molecule. The same features are relevant to the color centers in diamond. Impurities incorporated in solid matrices are coupled to the local environment. This leads to the blue-shifted excitations into the PSB, corresponding to phonon creation. Emission into the PSB is, on the other hand, red-shifted and corresponds to the annihilation of phonons.

These features can be explained on the basis of the diagram shown in figure 1.4. The ground and excited states are shown as a function of the configuration coordinate Q, i.e., a quantity which describes the configuration of the ions in the considered molecule [54]. The probability of transitions between different states can be obtained by the Frank-Condon principle [55, 56]. According to the Born-Oppenheimer approximation, the electronic transitions are significantly faster compared to the motion of the atoms in the lattice. Therefore, for the electronic transitions, the position of the atoms does not change and Q is constant for initial and final states, i.e., these can be represented as vertical transitions (see figure 1.4). In addition to the Franck-Condon principle, three other approximations are commonly introduced. The first one assumes that each lattice vibrational mode is well described by a quantum harmonic oscillator. Therefore, the vibrating carbon atoms in the diamond lattice can be represented as harmonic oscillators, i.e., parabolic shape of the potential wells in figure 1.4. Due to electron-phonon coupling, the electronic states include a number of vibrational states, indicated by n and n' in the ground and excited state, respectively. The harmonic oscillator assumption leads to the equal energy spacing between phonon energy levels. The second, low temperature approximation, assumes that

only the lowest (zero-point) lattice vibration n = 0 is excited. That means that electronic transitions do not originate from any of the higher phonon levels in the ground state, i.e., levels with n > 0. The third approximation is called linear coupling. This assumes that the interaction between the examined defect and the diamond lattice is the same in both the ground and the excited state. Specifically, the harmonic oscillator potential is equal in both states and shown as two equally shaped parabolic potentials in figure 1.4.
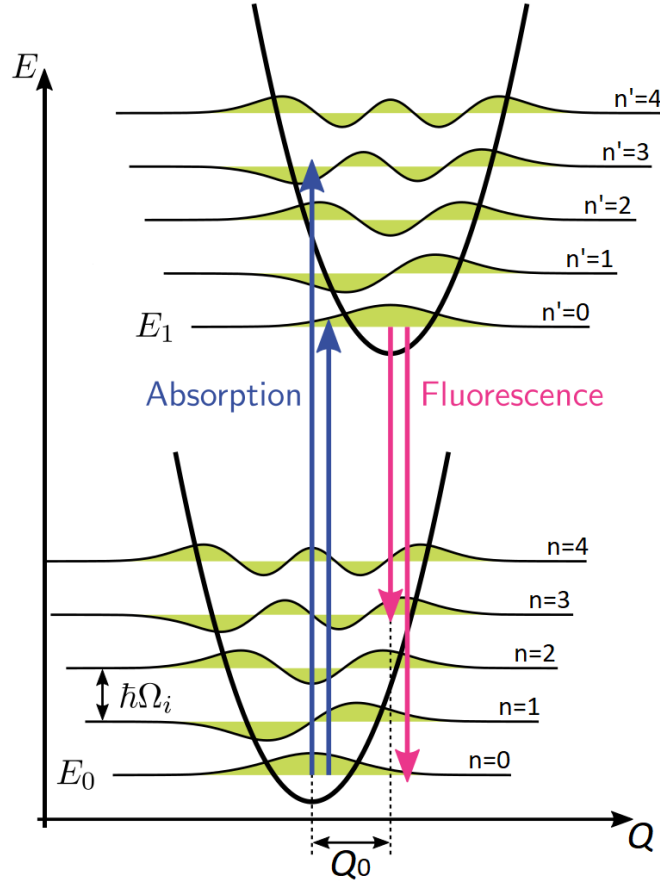
Figure 1.4: Energy diagram of electronic transitions with phonon coupling along the configuration coordinate Q, a normal mode of the lattice [55, 56]. The electronic states of the defect interact appreciably with only one normal mode Q of the lattice. The equilibrium position in the ground state is Q = 0. In the excited electronic state, the equilibrium position is at $Q = Q_0$ [54]. The energy difference between the ground and excited states is E_1-E_0 and the two potential energy curves are offset horizontally by the quantity Q_0. The blue arrows represent absorption without phonons and with three phonons, respectively. The downwards arrows represent the symmetric processes in emission. The n and n' levels indicate vibrational states for the ground and excited states of the color center, respectively. Transitions with n = n' = 0 belong to the ZPL. Transitions with n ≠ n' contribute to the PSB.

By taking into account all the considerations above, it is possible to follow optical excitation and luminescence pathways. The excitation from the ground state n to the excited state n' of the color center and resulting fluorescence to the ground state can follow different paths in terms of energy. The energy transitions originate at the lowest phonon energy level of the electronic states. According to the Frank-Condon principle, the highest transition probability is between states with the largest wave function overlap [54]. For example, in figure 1.4, the largest wave function overlap occurs between the two electronic states with n = 0 and n' = 3, respectively. The corresponding photon energy is $(E_1\text{-}E_0)+3\hbar\Omega_i$, where Ω_i is the characteristic vibrational frequency of the ith mode of the system and $\hbar\Omega_i$ represents the quantum of its vibrational energy. In the optical spectrum this will lead to increased absorption at a wavelength that is blue-shifted from the ZPL, i.e., the n = 0 -> n' = 0 transition. After the excitation, the system rapidly decays to the zero-point lattice vibrational level (n' = 0) by non-radiative processes. Therefore, the emission takes place from the n' = 0 state. Clearly, the largest overlap of wave functions is between the n' = 0 and n = 3 states, so that this transition is favoured compared to the zero phonon transition. That leads to higher probability of emission of photons with lower energy. On the luminescence spectra, this would result in a PSB that is red-shifted with respect to the ZPL. Note that the zero-phonon transitions are not phonon-mediated and have purely electromagnetic nature.

Figure 1.5 shows the typical absorption line shape for electronic transitions of individual color centers in diamond. The ZPL is located at a frequency ω' determined by the intrinsic difference in energy between ground and excited state as well as by the local environment. The PSB is shifted to higher frequencies in absorption and to lower frequencies in fluorescence. The frequency gap Δ between the peak of the ZPL and the peak of the PSB is determined by the Franck–Condon principle [55, 56].

The shape of the ZPL can be described by a Lorentzian profile [51]

$$I(\nu - \nu_0) = \frac{1}{4\pi^2} \frac{\Delta\nu_{\text{HOM}}}{(\nu - \nu_0)^2 + (\frac{\Delta\nu_{\text{HOM}}}{2})^2}, \tag{1.5}$$

Where $\Delta\nu_{\text{HOM}}$ represents the full width at half maximum (FWHM) of the Lorentzian line shape and $\nu - \nu_0$ determines the detuning of the exciting frequency ν with respect to the peak of the ZPL ν_0.

The temperature-dependent homogeneous line width $\Delta\nu_{\text{HOM}}$ is related to the excited state lifetime and described by the following equation [51]

$$\Delta\nu_{\text{HOM}} = \frac{1}{\pi}\left(\frac{1}{2T_1} + \frac{1}{T_2^*}e^{\left(-\frac{\Delta E}{k_B T}\right)}\right),\tag{1.6}$$

Where T is the temperature and ΔE is the energy of the considered transition, T_1 represents the fluorescence lifetime of the excited state and T_2^* represents the dephasing time of the optical transition.
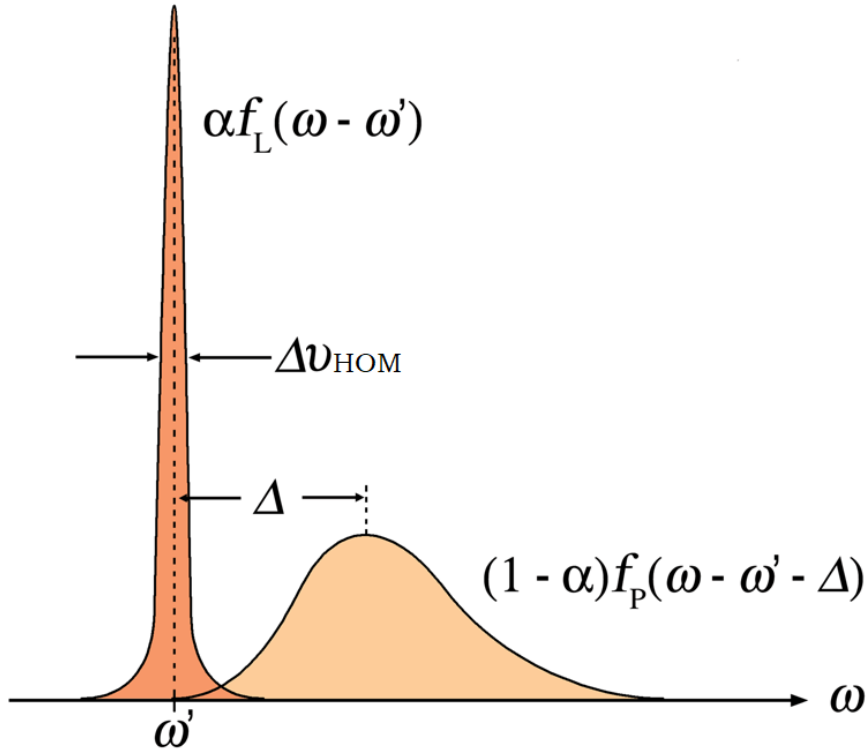

Figure 1.5: Schematic representation of the absorption line shape of an electronic excitation [55, 56]. The narrow component at the frequency ω' is the zero-phonon line and the broader feature is the phonon sideband. In emission, the relative positions of the two components are mirrored with respect to the center of the zero-phonon line at ω'. f_{L} and f_{P} refer to Lorentzian and Poissonian line shapes, α is the Debye-Waller factor and Δ is the frequency gap between the peak of the ZPL and the peak of the PSB.

Dephasing originates from interactions between the electrons with phonons of the system. At low temperature the parameter T_1 is temperature-independent. On the contrary, since the dephasing time is correlated directly to phonons, T_2^* depends on the temperature T. Thus, broadening of the spectral lines is expected at room temperature. The value of the broadening can be deduced from equation 1.6. For negligible phonon contributions at low temperature, the line width corresponds to the lifetime-limited value: the shape of the

ZPL is Lorentzian with a width determined by the excited state lifetime T_1 according to the Heisenberg uncertainty principle. In fact, equation 1.6 implies that, at absolute zero temperature (i.e., without the influence of the lattice), the natural line width (FWHM) of the color center ZPL is $\Delta\nu_{\text{HOM},0} = \frac{1}{2\pi T_1}$ [55, 56]. Nevertheless, the lattice reduces the lifetime of the excited state by introducing radiationless decay mechanisms. Above absolute zero temperature, thermal motions will introduce random perturbations to the defect's local environment. This leads to a shift in the energy of the electronic transition, introducing a temperature-dependent broadening of the line width (see equation 1.6). The measured width of a single color center's ZPL, the homogeneous line width, is then $\Delta\nu_{\text{HOM,T}} \geq \frac{1}{2\pi T_1}$ [55, 56].

The line shape of the PSB is described by a Poisson distribution as it expresses a discrete number of events, electronic transitions with phonons, during a period of time. At high temperatures, or in the case of strong interaction of the color centers with the lattice, the probability of multi-phonon transitions is high and the PSB can be approximated by a Gaussian distribution [55, 56].

The distribution of intensity between the ZPL and the PSB is characterized by the Debye-Waller factor α, which is defined as the ratio of intensity in the ZPL to the intensity in the whole emission wavelength range [57], and it is strongly dependent on temperature. At room temperature, the thermal energy is high enough to excite a large number of phonons. Decreasing the temperature, less and less phonons are excited. At cryogenic temperatures, then, the ZPL is very prominent while the PSB is strongly suppressed due to lack of phonon-mediated transitions [55, 56].

The SMS is a special case of fluorescence spectroscopy by which single molecules or crystal defects can be addressed. However, when the host matrix contains a large number of defects, each of them can contribute to the absorption and emission spectra. The spectra originating from a collection of color centers in the diamond lattice are called inhomogeneously broadened because each defect is surrounded by a varying environment which modifies the energy required for an electronic transition. Inhomogeneous broadening leads to an increase in the line width of an electronic transition that arises when different radiating or absorbing defects interact with different excitation wavelength components. The total fluorescence spectrum may contain peaks which are broader than those of single defects, since it shows an average over many differently emitting centers. The same is applied to absorption spectra. In an inhomogeneous distribution of color centers, individual ZPL and PSB positions are therefore shifted and overlapping, which results in inhomogeneous broadenings [55, 56].

Experimentally, both excitation and emission can be probed. A combination of confocal microscopy[1] and optical spectroscopy allows to detect photoluminescence signals from single molecules or color centers. However, probing the absorption at the single emitter level by standard methods is complicated, due to low detection efficiency. This problem can be overcome by implementing Photoluminescence Excitation spectroscopy. Within the framework of PLE experiments, instead of detecting the difference in the power delivered to and transmitted by the investigated color center, the luminescence intensity as a function of the excitation wavelength is analyzed. The absorption is traced by detecting emission away from the probed transition, i.e., detection of photon emission in the PSB by probing the ZPL transition. This allows to significantly improve the detection efficiency and to probe absorption with high precision [58].

Beside the spectral shapes and components, phenomena of intensity saturation occur. Intensity saturation arises from high power excitation. In case of resonant excitation, the system can be modeled as a three-level system [51]. Based on the rate equations for a three-level system, the intensity behavior can be calculated from the steady state conditions. The intensity-dependent line width $\Delta\nu_{\mathrm{FWHM}}(I)$ and recombination rate $R_{\mathrm{r}}(I)$ can be expressed as [51]

$$\Delta\nu_{\mathrm{FWHM}}(I) = \Delta\nu_{\mathrm{FWHM}}(0)\left(1 + \frac{I}{I_S}\right)^{\frac{1}{2}}, \tag{1.7}$$

$$R_r(I) = R_r(\infty)\frac{I/I_S}{1 + I/I_S}, \tag{1.8}$$

Where I is the excitation light intensity, I_S is the saturation intensity and $R_{\mathrm{r}}(\infty)$ the recombination rate at infinite power. The saturation power can be experimentally determined by detecting the fluorescence as a function of excitation power for a single center. By performing a background subtraction, pure color center fluorescence can be retrieved. This parameter can be used to optimize the signal-to-noise ratio in microscopic imaging or for investigation of excitation dynamics purposes.

To conclude, another important parameter in SMS experiments is the peak absorption cross section σ_{P}. Physically, σ_{P} is a rate which describes how well the incident excitation is absorbed by a defect in the host material. Mathematically, the absorption cross section σ_{P} is given as follows [51]

---

[1]The basic principles of confocal microscopy are described in section 2.2.1

$$\sigma_P = 2cT_2 \left(\frac{S}{N_{\text{TOT}}} \right)_{\text{ZPL}},$$

(1.9)

Where T_2 is the coherence time of the optical transition, defined as [59]

$$\frac{1}{T_2} = \frac{1}{2T_1} + \frac{1}{T_2^*},$$

(1.10)

c is the speed of light, N_{TOT} is the number density of absorbers producing the integrated absorption S. An increase in σ_P results in better microscopic imaging.

1.3.   Group-IV defects in diamond

In this section, some of the properties of group-IV element based color centers in diamond (i.e., Silicon-Vacancy, Germanium-Vacancy, Tin-Vacancy, Lead-Vacancy) are addressed, with emphasis on the Germanium-Vacancy color center, which is the defect investigated in the present work. Single negatively charged defects are discussed unless specifically mentioned. For instance, the GeV⁻ charge state of the defect is intended when the GeV center is discussed.

1.3.1.   Atomic structure of group-IV defects in diamond

Group-IV Vacancy defects are point defects in which a group-IV atom replaces two adjacent carbon atoms in the diamond lattice [60–62]. The impurity atom is located in between two vacant carbon spots in an interstitial lattice position. The resulting point defect is oriented along the $\langle 111 \rangle$ direction of the diamond lattice and possesses a D_{3d} symmetry. The atomic structure of group-IV defects is shown in figure 1.6. The inherent inversion symmetry results in no static electric dipole moment and first-order insensitivity to electric fields. For example, for the Silicon-Vacancy (SiV) center the absence of the first-order Stark effect leads to stable optical transitions, which do not exhibit noticeable spectral jumps and diffusion [60, 63]. As the symmetry of the defect governs its electronic structure, these features are common to all the remaining negatively charged group-IV defects, i.e., GeV, Tin-Vacancy (SnV) and Lead-Vacancy (PbV) [64].

Creation of group-IV defects can be performed in different ways. In the case of SiV and GeV centers, silicon or germanium atoms can be introduced into artificial diamond samples directly during the growth process (both HPHT and CVD) [46]. Alternatively, ion implantation and subsequent annealing at high temperatures, e.g., 1200 °C for silicon [49], can be utilized. SnV has only been synthesized via HPHT synthesis [46] and ion implantation [65], whereas formation of PbV defects by means of ion implantation only has been reported so far [66]. It is worth pointing out that, even though all group-IV based color centers share the same atomic structure, the size of the foreign atom increases with increasing atomic number (i.e., Si is the lightest and smallest atom in the group, while Pb is the heaviest and largest). The difference in sizes of the impurity atoms influences the properties of the formed color centers as well as the incorporation into the lattice and, thus, the ease of fabrication of high quality defects for applications.
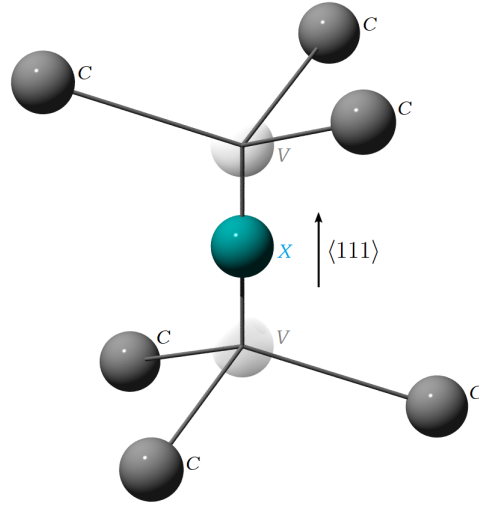
Figure 1.6: Illustration of a group-IV defect inside the diamond lattice. The carbon atoms of the diamond lattice are depicted by dark-gray spheres, the impurity atom (indicated by the letter X) by a blue sphere and the vacant lattice positions by partially transparent light-gray spheres. The resulting structure shows D_{3d} symmetry [63].

1.3.2.   Electronic structure of group-IV defects in diamond

Each color center formed by group-IV atom impurities shares a similar electronic structure, governed by their D_{3d} symmetry [67]. There are a total number of eleven electrons bound to the defect. Six of them come from the dangling carbon bonds making up the two split vacancies represented as light-gray spheres in figure 1.6, four electrons are provided by the sp^3 hybridized group-IV atom, and one additional electron is donated to the defect by a nearby donor, leading to the negative charge state of the center. The allowed irreducible representations for symmetry operations in the D_{3d} point group are: A_1, A_2 and E [68]. Due to inversion symmetry, any orbital wave function could either have an even (g, *gerade*) or an odd (u, *ungerade*) character. This allows the linear combinations of the electron molecular orbitals of the carbon dangling bonds with D_{3d} symmetry to take any of the following symmetries [68]: $a_{1,g}$, $a_{2,u}$, e_g and e_u. The electrons from the group-IV atom, on the other hand, transform like: $a_{1,g}$, $a_{2,u}$ and e_u. Odd states have lower energy than even states, and the A symmetry states reside at lower energies than the E symmetry states [67, 69]. In the presence of a group-IV atom in the defect, the energy of the carbon bonds is lowered so that they reside below the foreign element's levels with a negligible coupling [64]. The group-IV atom's orbitals are significantly higher in energy than the carbon ones and hence the latter are filled first [64]. As electrons have spin S = 1/2, taking the spin degeneracy of the levels into account, two electrons can fill each level and they are ordered

in the series: $(a_{2,u}, a_{1,g}, e_u, e_g)$, from lowest to highest energy. Filling the available levels from the lowest in energy with electrons, the level scheme is nearly filled up completely. The corresponding level occupation is the following: $a_{2,u}^2$, $a_{1,g}^2$, e_u^4, e_g^3, leaving only one hole in the e_g state [70] (see figure 1.7a). The described state represents the ground state of the defect. Since the hole can be on any of the two degenerate e_g states, the ground state has twofold orbital degeneracy, as well as twofold degeneracy from the spin state. Hence, the group-theoretical label of the fourfold degenerate ground state of the center is ^2E_g.

The excited state of the center is derived from the ground state formation by promoting an electron from the lower levels to the position of the ground state hole. This can also be represented as promoting the hole to the next lower energy levels. Figures 1.7b and 1.7c represent the electronic configurations of the first and second excited states, respectively. The first excited state is also an orbital doublet, but of ^2E_u symmetry. The second excited state, on the other hand, is an orbital singlet of $A_{1,g}$ symmetry that only has spin degeneracy. With these three mentioned levels (^2E_g, ^2E_u, $A_{1,g}$), the whole energy structure of the center can be described. In principle, there might also be a third excited $A_{2,u}$ level arising from the $a_{2,u}$ hole [71]. However, no signature of that has been observed. Thus, this level can be located in the conduction band of diamond. All described states are spin doublets due to the nature of the hole. As long as no ionization of the defect is considered, the system can be treated as a spin-1/2 system.
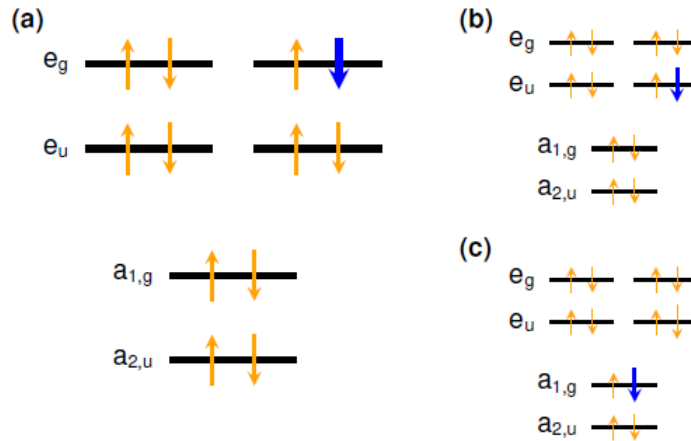
Figure 1.7: Electronic structure of a group-IV defect constructed from the electronic orbitals of the dangling bonds [71]. Orange arrows represent electrons with a certain spin while blue arrows denote missing electrons or holes. (a) A missing electron at the e_g orbital leads to a ^2E_g ground state of the center. (b) The next higher energetic configuration consists of a hole at e_u forming the ^2E_u excited state. (c) An even higher excitation of the hole to the $a_{1,g}$ orbital leads to a $A_{1,g}$ excited orbital singlet state.

The spin-orbit interaction lifts the degeneracy of the ground ^2E_g and excited ^2E_u states, which are therefore split into two levels each, see figure 1.8. The different spin-orbit interaction of the ground and excited states results in different splittings of the ground and excited state sub-levels. All four possible transitions between the ground and excited states are optically allowed, resulting in a fourfold fine structure of the ZPL, which can be observed at low temperatures. The transitions are named in order of decreasing energy with the letters A to D, as depicted in figure 1.8. The B and C transitions originate from a dipole that is aligned in parallel to the main symmetry axis of the defect, whereas the A and D transitions originate from a dipole which is perpendicularly aligned to the main symmetry axis of the defect. The dipole moment of transitions B and C is about four times stronger than the one of transitions A and D [61].
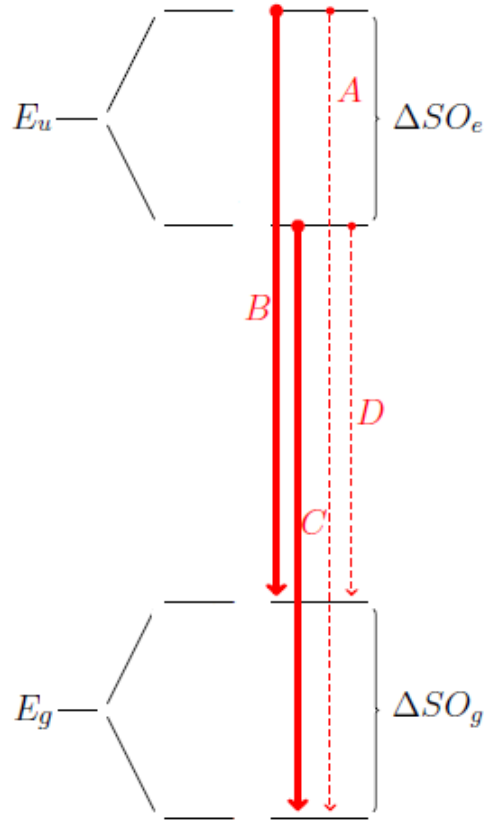
Figure 1.8: Spin-orbit split levels and optically active transitions of a negatively charged group-IV defect [72]. Transitions B and C are polarized perpendicular to the main symmetry axis of the defect and are shown in solid red lines. Transitions A and D are polarized parallel to the main symmetry axis and are depicted in dashed red lines. ΔSO_g and ΔSO_e denote ground and excited state splitting, respectively.

With increasing temperature, the spectral lines broaden. At room temperature all ZPL transitions merge, giving rise to the characteristic room temperature spectra of group-IV centers, see figure 1.9. The physical mechanism that aids in recording photoluminescence (PL) spectra is an A level that is excited by off-resonant excitation photons into the E states. Radiative decay processes from the ^2E_u excited state to the ^2E_g ground state then result in the characteristic ZPL emissions [71]. All negatively charged group-IV defects share these general properties. The different defects mainly differ in the absolute spectral position of the ZPL and the spin-orbit interactions due to the size of the group-IV impurity atoms, resulting in different ground and excited state splittings (denoted as ΔSO_g and ΔSO_e, respectively). The SiV center was first known by the energy of its most prominent spectral feature at 1.72 eV due to its occurrence in diamond films grown by CVD. Its ZPL at 737 nm appears as a relatively narrow spectral feature, which accounts for a significant amount of the overall fluorescence of the defect at ambient conditions. The GeV center spectrum has a prominent ZPL at 602 nm. The SnV center shows a ZPL peaked at a wavelength of 619 nm [62]. Finally, PbV defects feature a ZPL emission peaked at around 550 nm [73]. Examples of room temperature spectra are shown in figure 1.9.
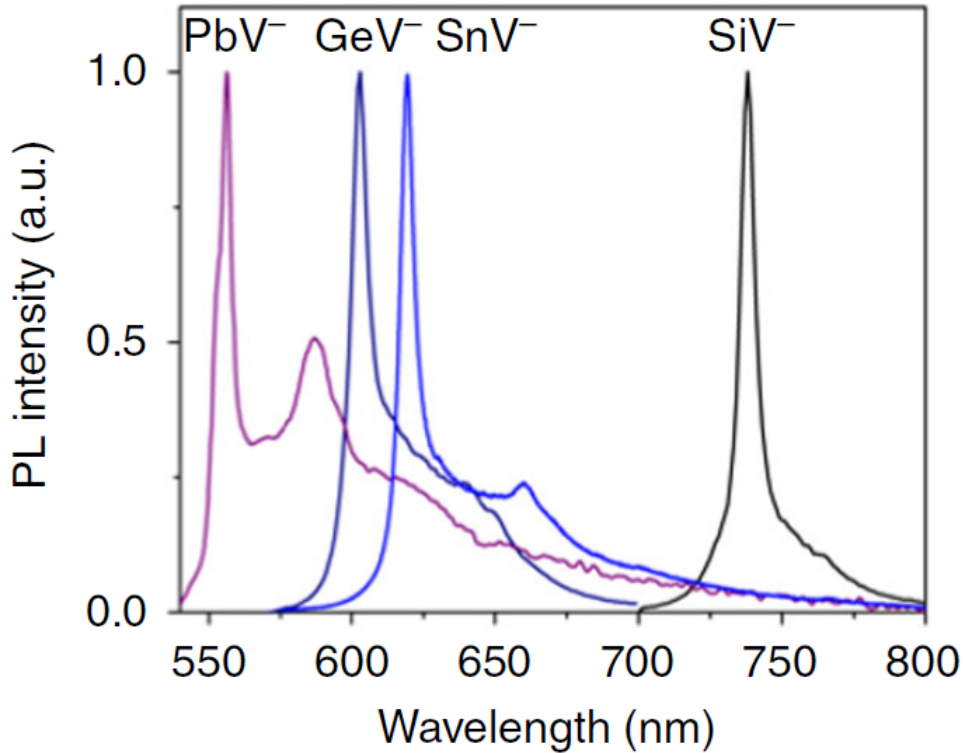
Figure 1.9: Typical room temperature photoluminescence spectra of SiV, GeV, SnV and PbV centers [46]. The negative charge state of the defects is here denoted explicitly.

Strain affects the energy levels of group-IV defects as well. Due to the D_{3d} symmetry, group-IV centers are susceptible to both axial (along the $\langle 111 \rangle$ direction) and transverse strain within the diamond lattice. That shifts the energy levels, thus shifting the ZPL or changing the ground and excited state splitting, respectively [49]. Strain within diamond samples containing group-IV defects is commonly introduced as a result of the lattice damage generated either during the growth process or by the ion implantation process and it is partially relieved by subsequent annealing treatments.

Without an external magnetic field, for group-IV color centers the spin sub-levels are energetically degenerate. The electron spin degree of freedom can be accessed by applying an external magnetic field $\mathbf{B}$, which lifts the spin degeneracy due to the Zeeman interaction

$$H_Z = \gamma_S \mathbf{S} \cdot \mathbf{B}, \tag{1.11}$$

Where the γ_S parameter is the electron gyromagnetic ratio and $\mathbf{S} = \frac{\hbar}{2}\boldsymbol{\sigma}$ is the spin operator with $\boldsymbol{\sigma}$ denoting the Pauli matrices. This results in four different transitions for each of the A, B, C and D transitions, as shown for transition C in figure 1.10.

Transitions C_2 and C_3 have different energies due to the difference in Zeeman interaction of the excited and ground state. Therefore, a spin selective transition can be addressed individually as long as the transition line widths are separated large enough, which is approximately double the inherent line width. For an external magnetic field aligned in parallel to the main symmetry axis of the defect, the spin projection onto this axis is a good quantum number. The selection rule for optical transitions is spin-conserving. Hence, transitions C_2 and C_3 are allowed. In contrast, transitions C_1 and C_4 should not be dipole allowed. However, even small strain in the crystal lattice mixes the spin states and the C_1 and C_4 transitions become partially allowed. If the mixing of spin states is small, the strength of these transitions is marginal compared to the spin-conserving ones. The relative strength of the transitions depends on the degree of spin mixing and is susceptible to the alignment of the external magnetic field $\mathbf{B}$ with the main symmetry axis of the color center. Rotations in the orientation of $\mathbf{B}$ result in a difference in the strength of the observed transitions. This correlation was experimentally shown for SiV in [60].
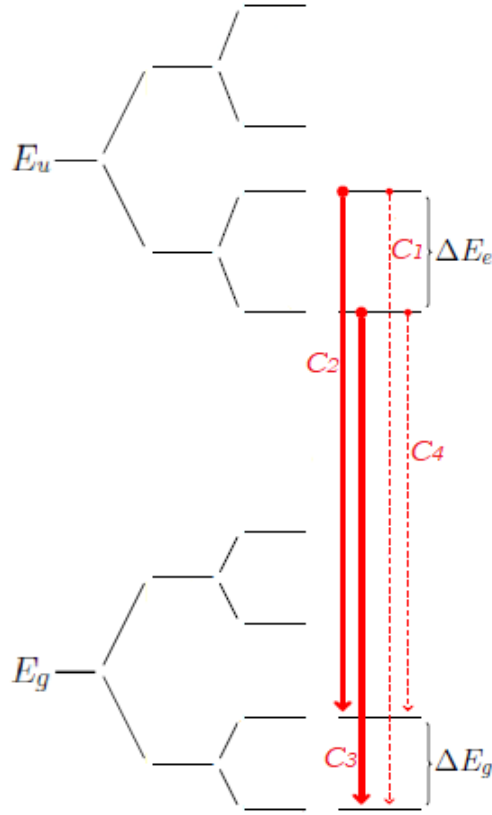
Figure 1.10: Energy level scheme of a group-IV defect in the presence of an external magnetic field [72]. Transition C is shown, split into four individual transitions. C_2 and C_3 denote spin-conserving transitions whereas C_1 and C_4 denote spin-flipping transitions. The latter are usually forbidden but become allowed if spin mixing takes place due to magnetic field or strain. Due to the difference in Zeeman splitting of the ground ($\mathbf{\Delta}E_g$) and excited state ($\mathbf{\Delta}E_e$), transitions C_2 and C_3 have different energies.

1.3.3. Germanium-Vacancy center in diamond

The Germanium-Vacancy center spectrum has a prominent ZPL at 602 nm and a phonon sideband extending roughly up to 670 nm [45, 74]. As well as for the other negatively charged group-IV color centers in diamond, the emission in the GeV ZPL is a significant amount of the overall fluorescence, see figure 1.9.

The energy level scheme of the GeV follows the general structure shown in figure 1.8. As a consequence, the fourfold fine structure of the ZPL is observable at low temperature, as shown in figure 1.11. From the energy difference in ZPL transitions, the spin-orbit splitting of the GeV can be determined. In [75] $\mathbf{\Delta}SO_g$ was found to be around 152 GHz and $\mathbf{\Delta}SO_e$ around 981 GHz. Due to relatively large splitting of the excited state sub-

levels, the occupation of the higher sub-level is low, due to a lack of mediating phonons. That leads to a strong pronunciation of the transitions originating from the lower excited state branch (transitions C and D in figure 1.11). At temperatures below 10 K the occupation of the upper branch and, thus, the intensity of the related transitions are reduced (transitions A and B in figure 1.11), so that they are barely observable [26].
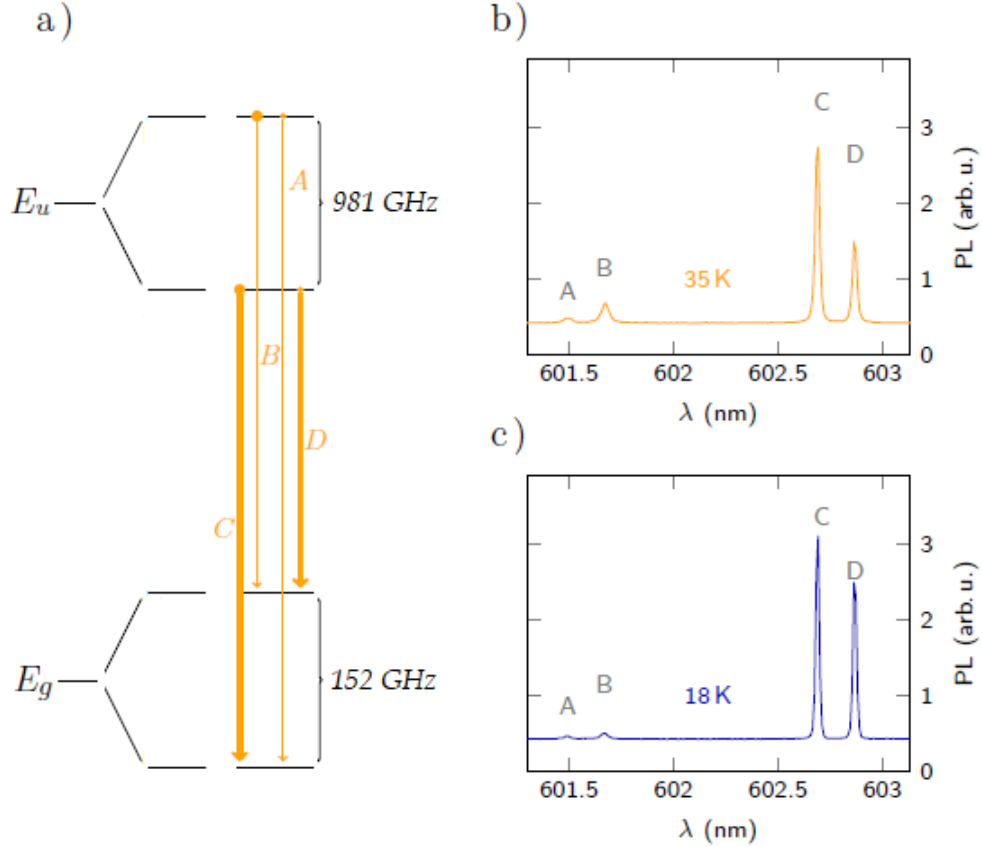
Figure 1.11: Low temperature spectra of a single GeV center [26]. (a) Typical spin-orbit split levels and optically active transitions of GeV defects. (b) All four ZPL transitions are identified at a temperature of 35 K. (c) Reducing the temperature to 18 K results in a stronger thermalization into the ground states and a significant reduction of the fluorescence from the higher energy transitions A and B. At a temperature of 5 K, no evidence of these transitions is observable in photoluminescence spectroscopy anymore.

An important parameter to determine the optical quality of a center is the lifetime of the ZPL fine structure transitions. As discussed in section 1.2, the excited state lifetime of a given transition relates to the corresponding line width according to equation 1.6. At absolute zero temperature, the natural line width (FWHM) of the color center ZPL is $\Delta\nu_{\mathrm{HOM,0}} = \frac{1}{2\pi T_1}$ [55, 56]. Above absolute zero temperature, the lattice reduces the

lifetime of the excited state by introducing a temperature-dependent broadening of the line width, which results in $\Delta\boldsymbol{\nu}_{\text{HOM,T}} \geq \frac{1}{2\pi T_1}$ [55, 56]. For the GeV center, T_1 lifetimes of 1.4-5.5 ns are reported in [74], which correspond to line widths of the transitions $\geq$ 29-114 MHz. By using resonant excitation single transitions are accessible: line widths for transition C of the GeV as narrow as 42 MHz were reported in [26], as shown in figure 1.12. These nearly lifetime-limited line widths promote the GeV as a source of indistinguishable single photons. This stems from the fact that the indistinguishability $\boldsymbol{\xi} \in [0, 1]$ of a single-photon source at short time scales can be measured by quantifying the extent to which an emitter's line width is lifetime-limited [59, 76]

$$\boldsymbol{\xi} = (2\pi T_1 \Delta\boldsymbol{\nu})^{-1} \, , \tag{1.12}$$

Where T_1 and $\Delta\boldsymbol{\nu}$ denote the emitters' lifetime and FWHM line width, respectively. Nearly lifetime-limited line width results in high degree of indistinguishability $\boldsymbol{\xi}$ of the GeV as single-photon source. Moreover, the line width of 42 MHz is about a factor of 2 smaller than reported for SiV [77], making the GeV a more promising candidate as source of indistinguishable single photons. The lifetime-limited line width for GeV centers equals 26 MHz [26]. That leads to the opportunity to obtain GeV centers with transition line widths narrower than the reported 42 MHz. Therefore, such GeVs would be even more promising as single-photon sources.
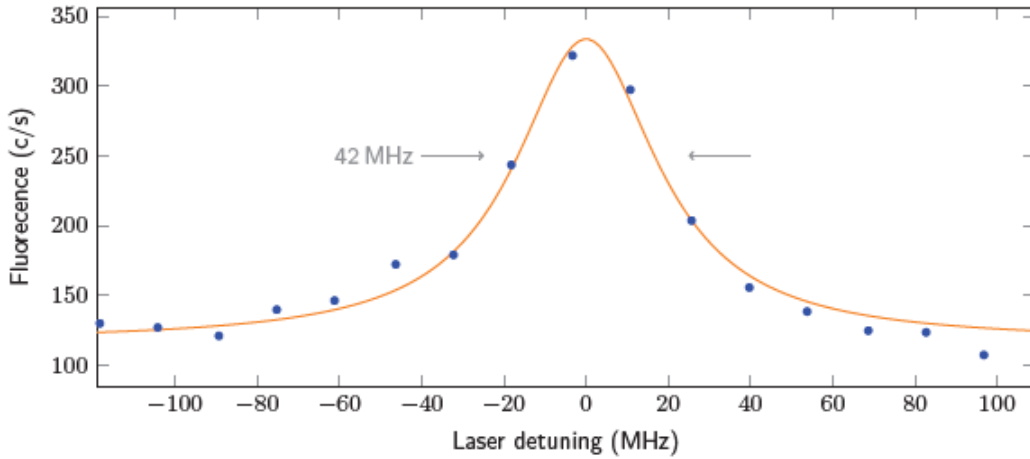
Figure 1.12: Resonant excitation of transition C of GeV at 5 K. Nearly lifetime-limited line width is observed. A Lorentzian fit (orange solid line) reveals a FWHM of 42 MHz [26].

The properties of the GeV defect are also influenced by isotopic effects: the absolute ZPL position is determined by the germanium isotope inherent to the defect. Germanium has five stable isotopes, listed in table 1.1. Explicit experimental proof for the presence of different isotopes in GeV centers is given by measuring GeV low temperature spectra in low-strain diamond samples. By varying all five isotopes, the corresponding energetic shifts in the ZPL can be calculated [78]. In the present work, ^{74}Ge is the only relevant isotope.

Table 1.1 (from [79])

Atomic mass m (^{m}Ge)	Natural abundance (%)
m=70	21.23
m=72	27.66
m=73	7.73
m=74	35.94
m=76	7.44

Table 1.1: Stable isotopes of germanium and relative natural abundance. The ^{74}Ge isotope, relevant for this work, is the most abundant in nature.

1.3.4. Comparison of GeV to different color centers in diamond

Within the framework of the present work, the properties of GeV color centers are studied. Therefore, it is essential to provide a comparison of GeV to other color centers, e.g., SiV, SnV, PbV and NV. Table 1.2 reports an overview of optical and electronic properties of group-IV (i.e., SiV, GeV, SnV, PbV) and NV defect centers in diamond.

At the beginning, it is worth comparing GeV with NV centers, as this is a well studied defect in diamond. Nitrogen-Vacancy and GeV centers in diamond feature different structural symmetries, shown in figure 1.13, which result in different properties. An NV center is formed by a nitrogen atom replacing a carbon atom of the diamond lattice, next to a vacancy, giving rise to a C_{3v} symmetry and a different energy level structure than the one shown in figure 1.7 for group-IV defects.

Table 1.2 (from [62])

	ZPL wavelength (nm)	Quantum efficiency (%)	Debye-Waller factor	Radiative lifetime (ns)	ΔSO$_{\mathrm{g}}$ (GHz)	T$_{operation}$ (K)
SiV	737	(1-10)/60	(0.65-0.9))	0.7	50	0.1
GeV	602	(12-25)	$\sim$0.6	(1.4-6)	170/152[75]	0.4
SnV	620	$\sim$80	0.57	(4.5-7)	850	1.8
PbV	520/555	Not known	Not known	>3/3.5	5700/3900	9.8/7.0
NV	637	>85	0.03	(11-13)	-	-

Table 1.2: Overview of optical and electronic properties of group-IV and NV defect centers in diamond. All listed numbers are approximate values. All defects are considered to be in the negative charge state. The Debye–Waller factor characterizes the fraction of radiative emission into the ZPL, while the quantum efficiency is defined as the amount of the radiative to the overall decay. ΔSO$_{\mathrm{g}}$ denotes splitting between orbital states in the optical ground state of group-IV color centers (see figure 1.8). T$_{operation}$ is the calculated operation temperature below which the expected orbital lifetime is above 100 ms. There are currently different findings about the exact parameters for the PbV center.

The NV center possesses a permanent electric dipole moment, making the optical transition frequencies sensitive to charge fluctuations in its environment. This sensitivity to electric fields has been used as a resource to tune different NV centers onto resonance, counteracting local strain inhomogeneities in the host diamond crystal which shift the transition frequencies of color centers [62]. However, it has also hindered the nanophotonic integration of NV centers due to degradation of their optical properties near surfaces [62]. For GeV centers, the inversion-symmetric D$_{3d}$ structure of the defects results in no permanent electric dipole and thus a first-order insensitivity to electric field fluctuations. As a consequence, tuning optical transition frequencies of GeV centers by electric fields is relatively inefficient. On the other hand, the vanishing permanent electric dipole makes these color centers excellent candidates for integration into photonic nanostructures [62]. Moreover, when it comes to applications of color centers as quantum nodes in quantum networks, GeV and in general group-IV defects show much better properties than the NV, which is instead well suited as a quantum sensor. Indeed, to generate entanglement, only the fraction of coherent photons emitted in the ZPL (for which no lattice vibrations assist the transitions) can be used. Importantly, all quantified ZPL emission fractions for GeV

defects are significantly larger than for the NV center, as the inversion symmetry causes their excited states to have larger overlap with the optical ground state. That results in a higher fraction of direct photon transitions. Taking into account that the fraction of photons emitted in the ZPL is given by the Debye-Waller factor, it is worth comparing these values. The Debye-Waller factor of GeV is 0.6, whereas for NV centers it is only 0.03 [62].
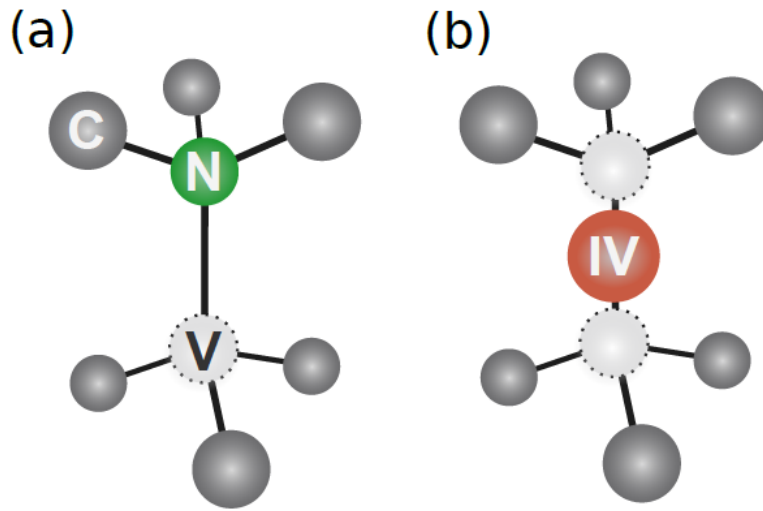

Figure 1.13: Schematic atomic structure of (a) NV and (b) group-IV color centers in diamond. The inversion symmetry of group-IV defects leads to a vanishing permanent electric dipole moment, making them suitable for integration in nanophotonic structures [62].

With respect to SiV centers, GeVs show a lower Debye-Waller factor. In addition, a significant amount of the observed individual transitions of the ZPL show a transform-limited line width for SiV centers. Furthermore, these transitions are spectrally stable over hours [77, 80, 81]. These optical properties make the SiV a promising candidate for single-photon source applications. Nevertheless, compared to other group-IV element based defects in diamond, a major drawback of SiV is the relatively low ground state splitting, as ΔSO_g increases for increasing size of the impurity atom. This is important for SiV as, due to the small ground state splitting, spin coherence suffers from phonon-mediated dephasing at temperatures above 10 mK. The optical transitions of GeV are narrower than in the case of SiV, owing to the larger ground state splitting and longer excited state lifetime. The better quantum efficiency of GeV results in an overall increase of flux of photons in the ZPL. Taking into account the longer excited state lifetime, this makes GeV centers good candidates as efficient light-matter interface. Furthermore, the approximately 3 times

larger spin-orbit coupling of its ground state manifold can be beneficial for its electron spin coherence time as it can be operated at elevated temperatures [62].

SnV centers show better properties when compared to GeVs. The SnV defect shows comparable Debye-Waller factor to the one of the GeV, but it has larger quantum efficiency, ground-state splitting and radiative lifetime [62]. Moreover, while most recent experiments with SiV and GeV centers require operation in dilution refrigerators (i.e., in the mK regime) in order to suppress thermal phonon population, the SnV centers can be operated at higher temperatures, i.e., utilizing standard liquid helium bath cryostats. That makes SnV centers particularly promising for uses as quantum network nodes [62]. However, the larger dimensions of the tin atom compared to silicon and germanium imply that it is more challenging to produce high quality SnV centers in diamond than SiV or GeV centers (ion implantation of heavy atoms such as Sn or Pb leads to large strain around the color centers inside the diamond crystal [73]). The situation becomes worse for PbV defects. In this sense, a trade-off is necessary between better physical properties and technical limitations, thus making the GeV defect the perfect candidate for future applications as a quantum node.

2 | Experimental methods

2.1. Diamond samples

The experiments discussed in this work aim at investigating fundamental optical properties of the probed GeV color centers and establishing the best way to produce high quality GeV centers in diamond in terms of the main parameters of the adopted germanium ion implantation process and annealing treatments. In this section, an overview of the investigated diamond samples is presented. The main features of the samples are discussed. The main parameters of the ion implantation processes and the annealing steps applied to the different samples are described as well.

In the present work, six 1×1 mm diamond samples were investigated. All the samples are commercially available elementsixᴛᴍ type-IIa electronic grade single crystal diamond samples, grown by CVD synthesis. They were grouped in two sets, called UU601 (in figure 2.1) and UU602 (in figure 2.2), respectively, each set consisting in three samples cut from the same substrate. The marked areas were produced by means of Focused Ion Beam (FIB) milling at the University of Ulm, Germany. ^{74}Ge ions were later implanted into the samples by means of ion implantation. The ion implantation process was performed at RUBION, Central Unit for Ion Beams and Radionuclides research institute in Bochum, Germany. The implantation parameters were: $\mathbf{10^{10}}$ ions/cm^2 implantation dose for all the samples, 95 keV and 350 keV implantation energy for samples belonging to the UU601 and UU602 sets, respectively. The processes resulted in the production of GeV centers (after appropriate annealing treatment) at depths estimated to be equal to $\mathbf{38.4 \pm 9.2}$ nm and $\mathbf{131.3 \pm 28.8}$ nm in average inside the diamond surfaces, respectively. The depths of the created color centers were estimated utilizing Monte-Carlo simulations performed by means of the SRIM software [82] (refer to figure 2.3). The standard deviations in the mean projected range (depth) values correspond to straggling of the ions. Ahead of each experiment and annealing step, the diamond samples were cleaned in a boiling acid mixture consisting in equal parts of nitric, perchloric and sulfuric acid to remove surface contaminants [83].

Samples UU601-1, UU601-2 and UU601-3 are shown in figure 2.1, whereas samples UU602-1, UU602-2 and UU602-3 are shown in figure 2.2. The six samples were subjected to different annealing processes in high-vacuum (pressure of 10^{-8} mbar), that is:

- Samples UU601-1 and UU602-1 were annealed at 850 °C for a total annealing time of 4 hours, in two separated steps (first for 1 hour and then for 3 additional hours at a later date), with a rump-up of 7 °C/min in both cases (see figures A.1 and A.2 for the annealing temperature versus time profile).

- Samples UU601-2 and UU602-2 were annealed at 1200 °C for a total annealing time of 2 hours, in two separated steps (first for 1 hour and then for 1 additional hour at a later date), with a rump-up of 7 °C/min in both cases (see figure A.3 for the annealing temperature versus time profile).

- Samples UU601-3 and UU602-3 were annealed at 1500 °C for a total annealing time of 1 hour, with a rump-up of 7 °C/min (see figure A.4 for the annealing temperature versus time profile).

An overview of the treatments the investigated samples were subjected to is given in table 2.1.
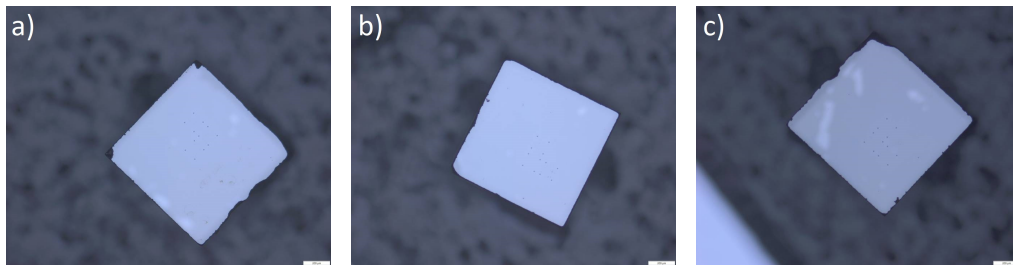
Figure 2.1: Microscope images of (a) sample UU601-1, (b) sample UU601-2 and (c) sample UU601-3. FIB markers are visible on the surfaces of the three samples.
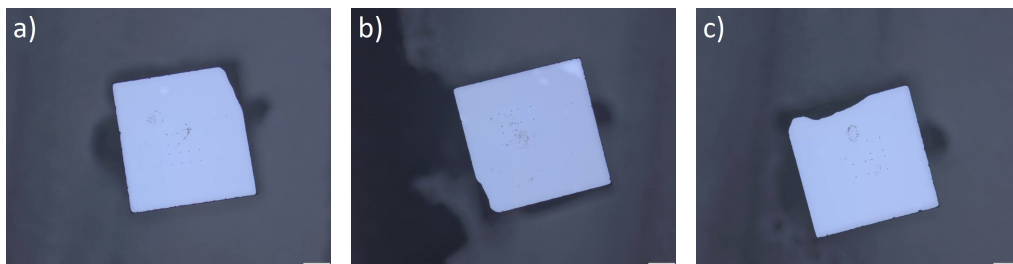
Figure 2.2: Microscope images of (a) sample UU602-1, (b) sample UU602-2 and (c) sample UU602-3. FIB markers are visible on the surfaces of the three samples.

Table 2.1

Sample	Implantation energy (keV)	Implantation depth (nm)	Annealing temperature (°C)	Annealing time (h)
UU601-1	95	38	850	1+3
UU601-2	95	38	1200	1+1
UU601-3	95	38	1500	1
UU602-1	350	131	850	1+3
UU602-2	350	131	1200	1+1
UU602-3	350	131	1500	1

Table 2.1: Overview of the investigated samples and relative treatments.
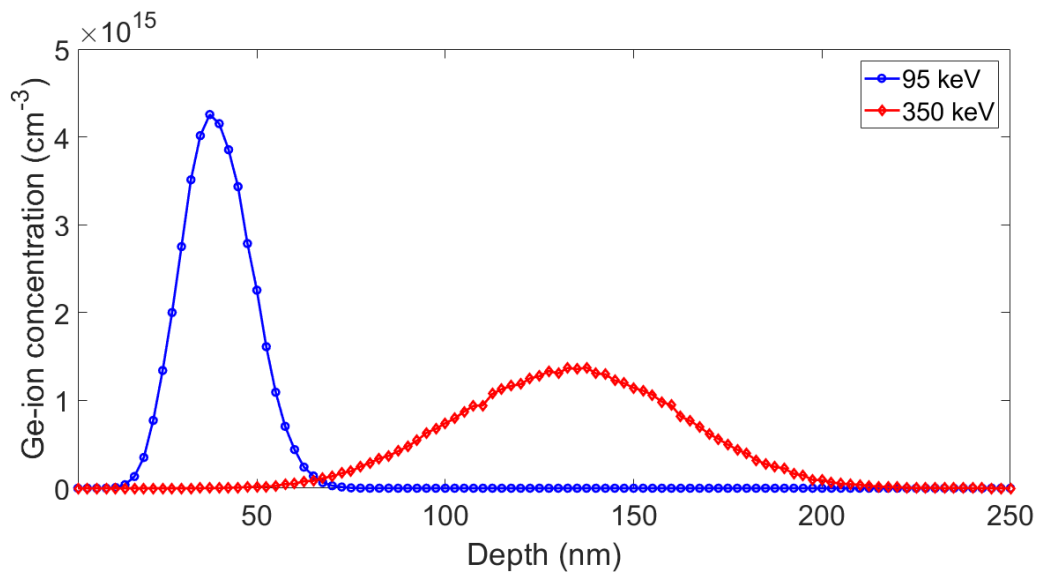
Figure 2.3: Ge ions concentration versus depth inside the diamond surface for samples (blue) UU601 and (red) UU602, according to SRIM Monte-Carlo simulations. It is assumed that the Ge ions do not move during the annealing treatments (due to short diffusion lenght), whereas the vacancies do. Consequently, the average depth of the created GeV color centers can be estimated to be the same as the implantation depth of the Ge ions.

2.2.   Experimental equipment and setups

In this section, a comprehensive overview of the utilized experimental equipment is provided. Basic working principles of confocal microscopy are discussed. The two home-built experimental confocal setups used for the realization of the performed experiments are described. An overview of the properties of the utilized cryogenic cooler and laser equipment is given as well. The experimental investigations discussed in the present work were performed in the laboratories of the Institute for Quantum Optics of the University of Ulm, Germany, by means of the equipment and setups presented below.

2.2.1.   Basic principles of confocal fluorescence microscopy

Confocal fluorescence microscopes are standard tools utilized to perform experiments with single color centers in diamonds. In fact, most of the scientific knowledge about group-IV defects in diamond has been gained using these devices [61, 77, 84]. The scheme of a confocal microscope setup is shown in figure 2.4. A laser beam is sent to a high numerical aperture (NA) objective through the beam sampler. The objective focuses the excitation light onto a specific volume of the sample. With respect to standard microscopy, the light is focused to the diffraction limited spot. Adjustment of the focal point is required during the experiments, as its position is influenced by the dependence of the refractive index n of diamond on excitation wavelength $\boldsymbol{\lambda}$ as well as on temperature T and pressure P (see section 1.1.1). Fluctuations in these parameters would result in the confocal setup focal alignment fluctuating during the measurements, which would in turn influence intensity and contrast of the recorded confocal maps. The emitted luminescence light coming from the investigated area of the sample is collected by the same objective. In other words, only the emitted light originating from the illuminated area is contributing to the detected signal. This enhances the sensitivity of confocal microscopes in comparison to conventional ones. To compensate the different wavelengths of excitation and luminescence light, chromatically-corrected objectives are typically used. The luminescence light follows the path of the excitation light and goes through the beam sampler. At the beam sampler, the majority of the collected light passes through. To achieve a high collection efficiency, a dichroic mirror or an appropriately chosen anti-reflection coating of the beam sampler can be used. Further, the light is focused on the pinhole by means of an achromatic lens. This configuration is used to block light which is not originating from the focal plane of the objective. The light passing through the pinhole can then be considered as originating from a point source. Hence, the geometry of the detection assembly can be chosen independently of the rest of the confocal microscope. In the present work, the light

transmitted through the pinhole was focused on a photodetector by a second lens. An Avalanche Photo Diode (APD) was used as a detector. In order to block the residual laser light and detect the light in the desired spectral region only, optical filters were installed in between the second lens and the APD. In case of an overlap of excitation wavelength and detection window, polarization-selective components could be used. As an optional element, a flip mirror can be placed in the optical path after the second lens. That mirror is used to transmit the luminescence light to a spectrometer.

Assuming that the setup is equipped with an infinitesimally small pinhole, the lateral and axial resolution of the confocal microscope is improved by a factor of $\frac{1}{\sqrt{2}}$ compared to standard microscopes, thus yielding a lateral FWHM of the point spread function of this system (which describes the response of a focused optical imaging system to a point source or point object) equal to [85]

$$FWHM_{(x,y)} = \frac{0.51\lambda_{exc}}{NA}, \tag{2.1}$$

Where λ_{exc} is the excitation wavelength and NA is the numerical aperture of the objective. Taking into account the refractive index n of the medium between the objective and the sample, the FWHM of the point spread function along the optical axis is given by [85]

$$FWHM_z = \frac{0.88\lambda_{exc}}{n - \sqrt{n^2 - NA^2}}. \tag{2.2}$$

However, since real pinholes are not infinitesimal, the actual resolution in z is reduced as follows [85]

$$FWHM_{z,real} = \frac{0.88\lambda_{exc}}{n - \sqrt{n^2 - NA^2}} \cdot \left(1 + \left(\frac{r_{pinhole}}{AU}\right)^2\right), \tag{2.3}$$

Where $r_{pinhole}$ is the radius of the pinhole and AU is the airy unit. The AU is the product of the objective magnification M and the radius of the airy disk. The airy disk represents the best focused spot of light produced by a perfect lens with circular aperture, only limited by diffraction of light. Using pinholes having smaller diameters can increase the z resolution of the microscope. However, the main benefit is an increased signal-to-noise ratio even though the collection efficiency of the setup is reduced. Note that, for some applications, the pinhole can be substituted by an optical fiber. In that case, the core of the fiber acts as a pinhole and the pinhole size is therefore given by the core diameter of the used fiber. To allow a confocal microscope to image a specific area of the investigated sample, some

kind of beam scanning mechanism must be implemented. This can be achieved by moving the sample with respect to the optical path or by moving the beam path (and, therefore, the illuminated volume) across the sample. For such purposes, piezoelectric scanners are usually utilized. In the context of the present work, two home-built confocal microscopes have been utilized.
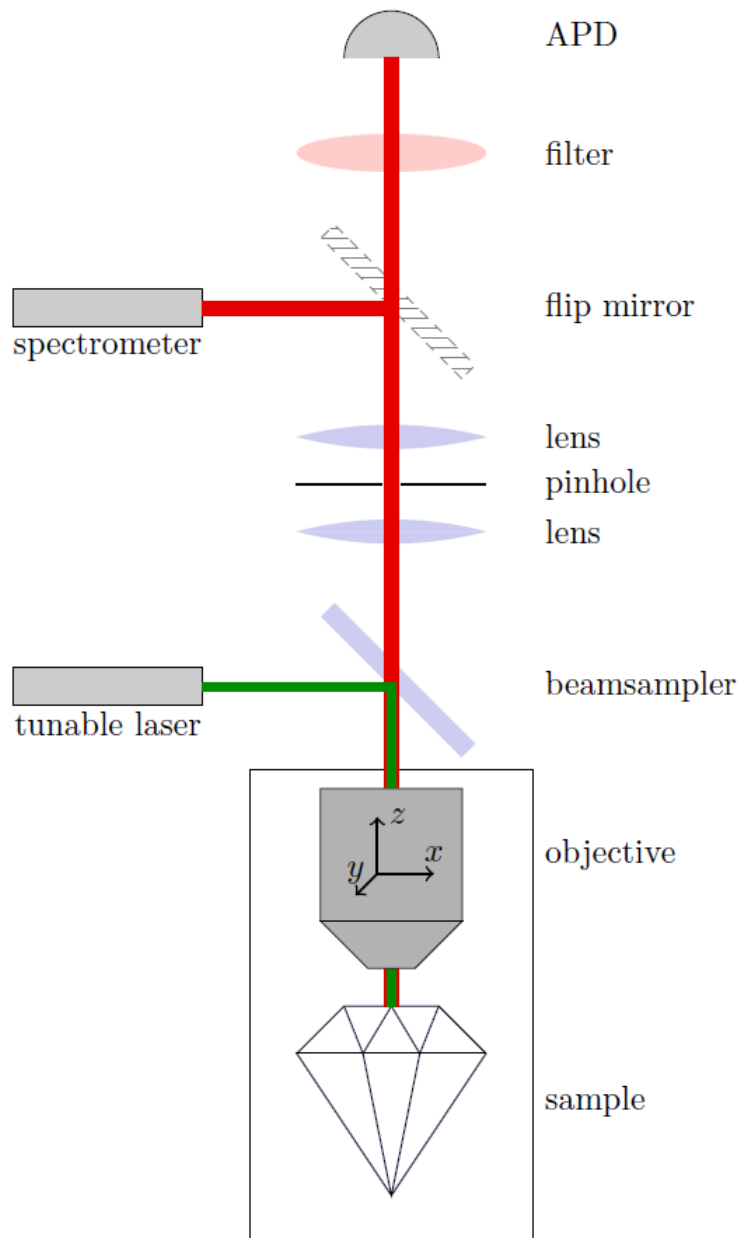
Figure 2.4: Sketch of a confocal microscope setup used to resolve single fluorescence sites in diamond samples [72].

2.2.2. Room temperature confocal setup

A home-built room temperature confocal setup, shown in figure 2.5, was used for all spectroscopy experiments performed at room temperature. On this setup, the off-resonant excitation light for the GeV defects is provided by a laser located on the same optical table and directed to the setup via a single-mode, polarization-maintaining fiber (Thor-Labs, PM-S405-XP). After the fiber the light is collimated by an aspheric lens. A 532/3 band-pass filter is placed as well, in order to filter the scattered light coming from the fiber. The beam is then guided towards the back aperture of the microscope objective (Olympus, MPlanoApo N 50x/ NA 0.95) by several mirrors and a beam sampler. The objective is mounted on a xyz piezo scanner (Npoint, NPXY200-Z25), in order to perform scanning of the sample. The traveling range of the scanner is 200 μm in the x and y directions and 25 μm in the z direction. Moving the objective results in a shift of the focal volume from which the fluorescence is collected by the same objective. An achromatic lens of focal length f = 75 mm is used to focus the fluorescence light through a 15 μm pinhole which ensures sufficient z-resolution and suppresses background light entering the detection assembly of the setup (see equation 2.3). A second achromatic lens of f = 75 mm is located at a distance of 2f from the pinhole in order to focus the transmitted light on the utilized APD (Excelitas Technology, SPCM-AQRH-14). In front of the APD, a 607/45 or a 600/40 band-pass filter are alternatively used. Upon photon arrival on the APD, a Transistor-Transistor Logic (TTL) pulse is created. The photon counting is performed using a data acquisition card (National Instruments, NI PCIe-6323). The same device is also used to control the piezo scanner via an analogue output signal. This allows synchronization of the detected signal and the objective position. A remotely-operated flip mirror, located inside of the detection assembly, is used to guide the signal to a spectrometer to record photoluminescence spectra. The spectrometer (Quantum Design, Andor) is equipped with a Czerny–Turner monochromator (Shamrock-500i). Three diffraction gratings (150 l/mm, blaze 1250 nm; 300 l/mm, blaze 500 nm, 600 l/mm, blaze 500 nm) are installed on a motorized turret which allows to change the grating remotely. The diffracted light is recorded by a CCD camera (Andor, iDus-DU416A-LDC-DD). The CCD chip is cooled down by a Peltier element to a temperature of - 80 °C, which allows to increase signal-to-noise ratio by reducing the thermal noise of the chip. For the experiments presented in this work, the 600 lines/mm grating at a blaze wavelength of 500 nm was used. The spectral resolution of the grating is 0.05 nm. At the spectrometer, the straight laser light is blocked alternatively by either a 561 long-pass or a 545 long-pass filter, placed in front of the spectrometer input. To control the performed experiments, a python based modular lab control software package, named Qudi [86], is used.
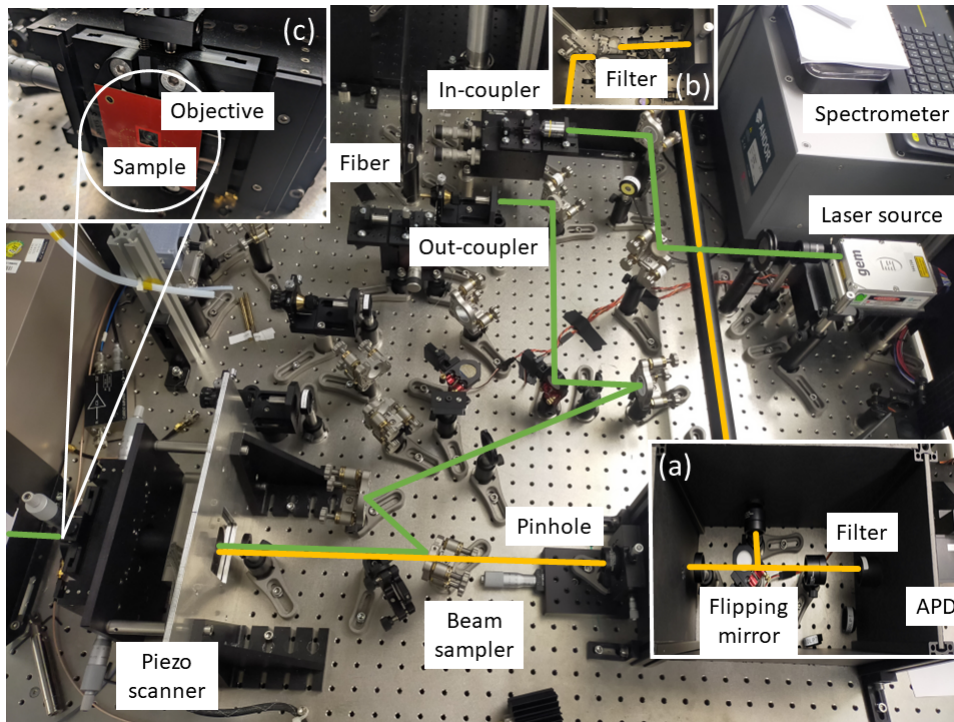
Figure 2.5: Home-built confocal setup used to perform room temperature spectroscopy experiments. The green path symbolizes the 532 nm excitation light coming from the laser source and directed to the diamond sample to be investigated. The orange path symbolizes the fluorescence light coming from the excited color centers. In the insets: (a) shows the optical path at the detection side, leading fluorescence light from the pinhole to the APD; (b) shows the optical path leading fluorescence light to the spectrometer; (c) shows the diamond sample mounting and utilized objective: the samples are glued on top of glass slides, themselves taped to a printed circuit board screwed to the piezo stage.

2.2.3. Cryogenic setup

The cryogenic experiments were performed on the setup shown in figure 2.6. The samples were installed in a continuous flow cryostat (CryoVac), shown in figure 2.7. The cryostat consists of two parts. The cold head is mounted on the piezo positioner, which allows approach to the objective. The objective is mounted on the piezo scanner (PI, P-562.3VD), that is placed on the second part of the cryostat. Note that the scanner is kept at room temperature during the operations. This allows to build a confocal setup that is similar to the room temperature one. The mounting of the samples is a two stage process. At the beginning, the samples are attached to a copper plate by means of silver paste. The silver paste is chosen as an adhesive to ensure good thermal conductivity. In the next step, the copper plate is attached to the cold head by means of a clamp. In order to provide

good thermal conductivity, vacuum grease (Apiezon) is placed in between cold head and copper plate. The cold head is then cooled down by continuous flow of liquid helium. This allows to reach temperatures down to 4 K. The temperature is monitored by a temperature controller (CryoVac, TIC500). The temperature controller includes a PID-controlled heater which could be used to heat the samples up to 250 K. The operation pressure of the cryostat is in the range of 10^{-7} mbar. The excitation light for cryogenic experiments is provided by several laser sources located on a separate optical table. The light is transmitted to the cryogenic setup by optical single-mode, polarization-maintaining fibers, similarly to the room temperature setup. After the fiber the light is collimated by an out-coupling objective (Olympus, E Plan, 4x, NA 0.1). Then, the light propagates through a set of $\lambda/2$ plates and polarizers (polarization beam splitter cube and Glan-Thompson prism) to ensure polarization stability during the experiments. The beam is guided inside the cryostat by several mirrors and a beam sampler. The excitation light is focused on the sample by the objective (Olympus, UMPlanFI, 100x, NA 0.95). The same objective is used to collect fluorescence light and guide it to the beam sampler. After the beam sampler, the luminescense light is focused by a lens of focal length f = 75 mm onto the 25 μm pinhole. A second lens of focal length f = 75 mm is placed at a distance of 2f from the pinhole to focus the light on the APD (Excelitas Technology, SPCM-AQRH-16). Similarly to the room temperature setup, an additional flip mirror is installed in order to guide the light to the spectrometer (Princeton Instruments). The spectrometer is equipped with a Czerny–Turner monochromator (Acton SP2500) and an actively cooled CCD camera (PIXIS 100BR). For the low temperature experiments, a grating with 1200 lines/mm, blaze wavelength 750 nm is used. The chosen grating provides a spectral resolution of 26 GHz. Within the framework of different measurements, different sets of filters were used after the out-coupler and in front of APD and spectrometer:

- Low temperature photoluminescensce spectroscopy: 532/3 band-pass clean-up filter, 607/45 band-pass at the detection and 561 long-pass in front of the spectrometer.

- Photoluminescensce Excitation spectroscopy: 532/3 band-pass clean-up filter, 633 short-pass and 561 long-pass filter in front of APD and spectrometer, respectively.

- Lifetime measurements: 532/10 band-pass clean-up filter, 604/45 and 600/10 band-pass filters at the detection side and 564 long-pass filter in front of the spectrometer.

The photon counting and hardware control are performed by a data acquisition card (National Instruments, NI PCIe-6323). In the lifetime measurements, photons were counted by means of a fast multiscaler card (Fast ComTec, MCS8A, 80 ps resolution). The scanning range of the piezo scanner which moves the objective is 200 μm in the x, y and z

directions. Control of the experiments is performed by means of the Qudi software.
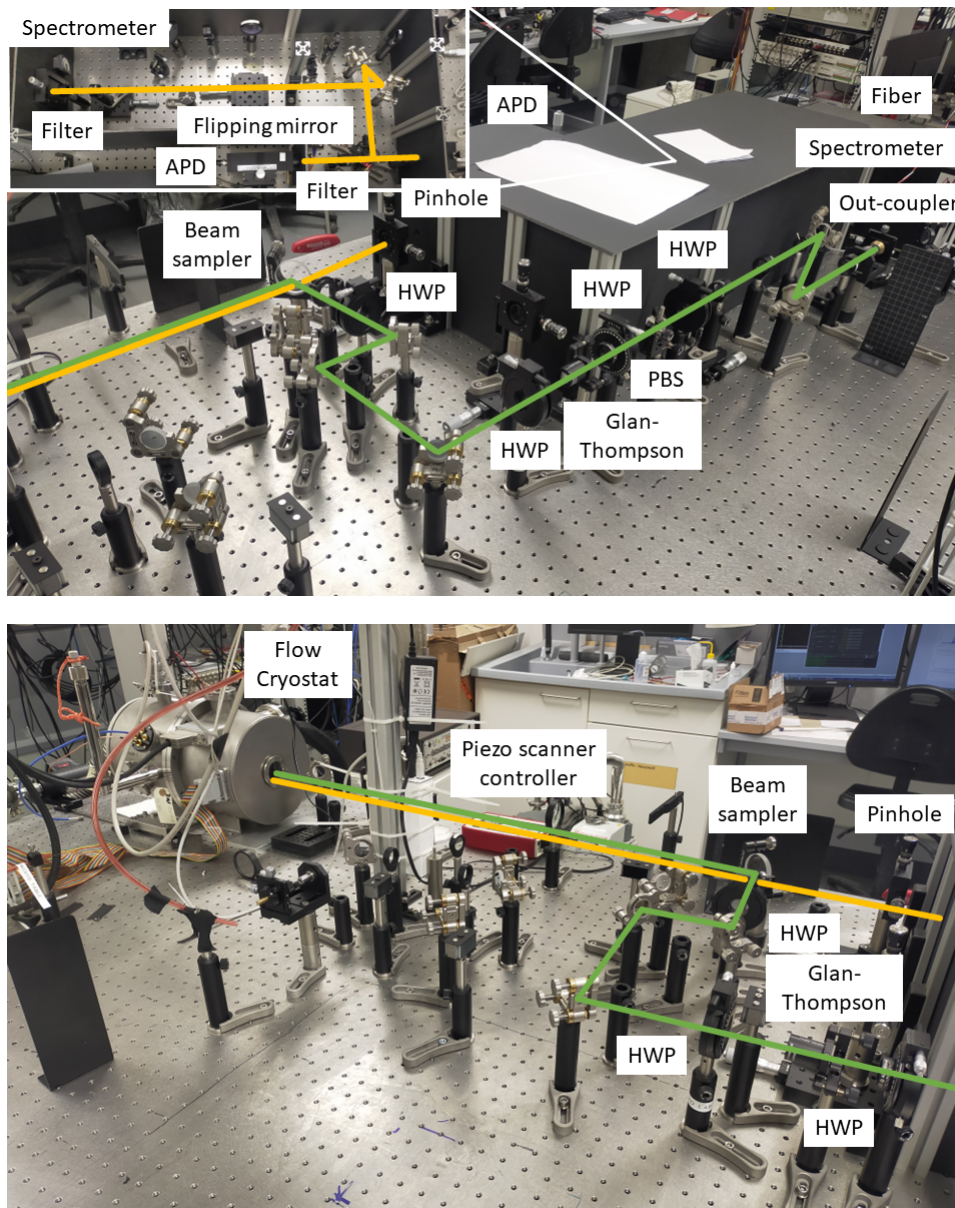
Figure 2.6: Overview of the low temperature setup. The right (top) and left (bottom) sides of the setup are shown separately for clarity. The green path symbolizes the excitation light coming from the laser sources (located on a different optical table) and guided to the continuous flow cryostat (see figure 2.7). The orange path symbolizes the fluorescence light coming from the excited color centers. The inset shows the optical path at the detection side, leading fluorescence light from the pinhole to the APD or to the spectrometer, alternatively. HWP and PBS stand for Half Wave Plate and Polarising Beam Splitter, respectively. HWPs, PBSs and the Glan-Thompson prism were used to fix and filter the polarization of the excitation light.
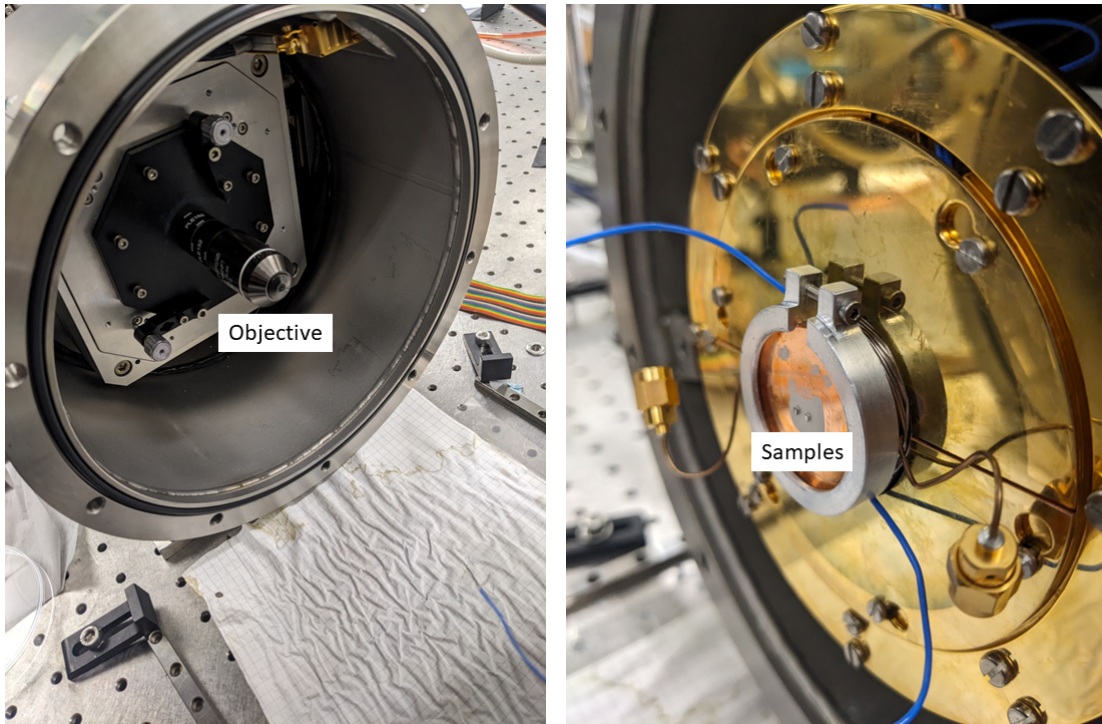
Figure 2.7: Pictures of the flow cryostat. (left) Room temperature part. The objective is mounted on a piezo-driven scanner. (right) Cold head. Two samples are attached to the copper plate by silver paste. The copper plate is mounted on the cold head.

2.2.4. Laser sources

In the present work, different types of laser systems were used. In the case of low temperature spectroscopy, the lasers were placed on a separate optical table to avoid any unfavourable influence on the experimental apparatus by stray light or vibrations caused by the laser systems. For both room temperature and low temperature photoluminescence spectroscopy, off-resonant excitation by a continuous wave (CW) 532 nm laser (Laser Quantum GEM) was used. The Photoluminescence Excitation measurements were performed utilizing a dye laser (Spectra Physics, Sirah, Matisse) operating with Rhodamine B in Ethylenglycol, pumped by a 532 nm laser. The laser has a line width below 120 kHz as well as long-term stability. To counteract long-term drifts of the reference cavity, a feedback signal generated from a wavelength meter (HighFinesse, WS-7) was used. The operation wavelength of the dye laser is around 602 nm. For the lifetime measurements a femtosecond optical parametric oscillator (OPO) system was used. The OPO system consists in two parts. The first one is a Ti:Sa oscillator (Spectra Physics, Tsunami) producing 150 fs long pulses at a central wavelength of 810 nm. The repetition rate of the oscillator is kept constant at 80 MHz by an actively stabilized cavity synchronized with an external

reference. The NIR pulses pump the OPO cavity (Spectra Physics, Radiantis Inspire) in which generation of shorter wavelengths takes place. The tuning range is between 400 nm and 650 nm. In the presented experiments, a wavelength of 532 nm was used. The power of the CW laser was attenuated by an Acousto-Optic Modulator (AOM) installed on the beam path. The power of the femtosecond laser was adjusted by various neutral density filters.
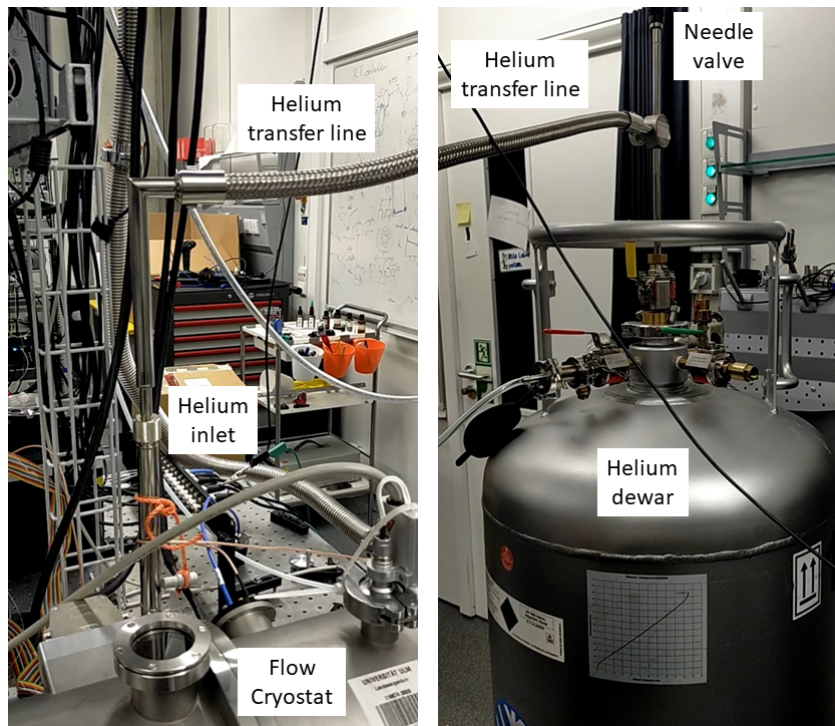
Figure 2.8: Equipment utilized to cool the diamond samples down to $\approx$ 4 K inside the CryoVac flow cryostat. The cool down procedure is carried out as follows. After checking vacuum pressure ($\approx 10^{-7}$ mbar) and the helium level inside the dewar, the helium pump is turned on and the transfer line is inserted into the dewar. The needle valve is opened to allow for the flow of helium. The other end of the transfer line is then inserted into the flow cryostat and the helium pump is opened to start the cool down. The cooling rate reaches 5 K/min after some time and, when the temperature of the diamond sample approaches 4 K, the needle valve is closed to stabilize the temperature of the sample.

3 | Results and discussion

3.1. Photoluminescence spectroscopy

This section is focused on photoluminescence spectroscopy at room and low temperatures. The room temperature measurements provide information on the formation of GeV centers upon different annealing treatments. In addition, inhomogeneous broadening of the line widths of the emitters is estimated from the obtained spectra. The low temperature investigations aim at estimating the strain in the diamonds after ion implantation and subsequent annealing. The impact of the implantation energy is discussed.

3.1.1. Room temperature photoluminescence spectroscopy

Room temperature PL spectroscopy was performed on all the six diamond samples after each annealing step, resulting in 10 experiments in total. The experiments were performed using off-resonant 532 nm excitation at a power of ≈ 500 μW. The measurements were taken in the corners of the L-shaped marked regions of the samples, see figures 2.1 and 2.2. The surveyed corner regions of the samples have a total size of 100 μm $\times$ 100 μm. During the spectroscopic investigations 4 to 6 sub-regions were chosen for each sample. Each sub-region has size of 20 μm $\times$ 20 μm. In each area, the GeV color centers were clearly identified and probed. Within the scanning areas the density of GeV centers is relatively low to clearly distinguish single defect sites. On the other hand, the density is sufficient to obtain statistical information. Room temperature (RT) spectroscopy was performed on the setup described in section 2.2.2.

Samples UU601-1 and UU602-1 were annealed and studied in two steps. After the first annealing step, i.e., 850 °C for 1 hour, no indication of formation of GeV centers was observed. The recorded spectra show a relatively strong background, observed throughout the samples surfaces. To clarify the feasibility of the annealing temperature of 850 °C to form GeV centers, the same samples were annealed for additional 3 hours. After the treatment, the confocal scannings reveal distinguishable sites, see figure 3.1a. The corresponding PL spectra show the presence of GeV features. However, the obtained GeV

spectra contain a strong background, that was only slightly mitigated by the additional annealing treatment. An example of spectrum is shown in figure 3.2a, where both GeV ZPL peak and the strong background feature are clearly visible. Note that the areas showing strong fluorescence signal in figure 3.1a do not correspond to GeVs.
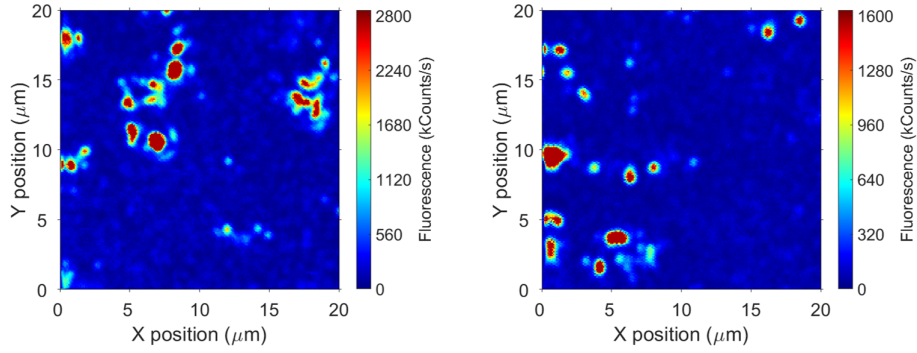
(a) RT confocal microscope images of samples (left) UU601-1 and (right) UU602-1.
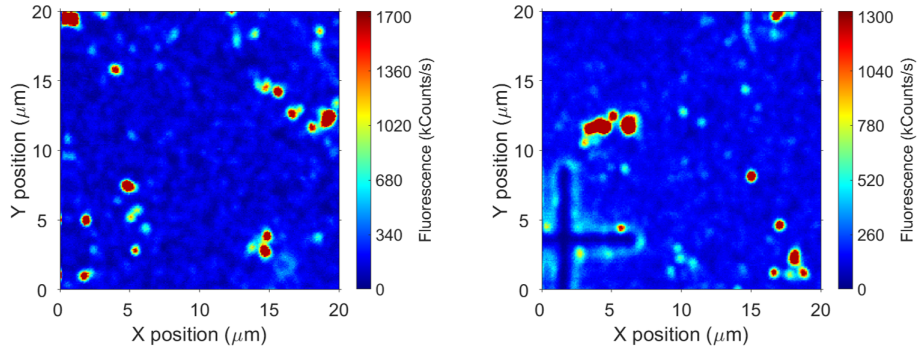
(b) RT confocal microscope images of samples (left) UU601-2 and (right) UU602-2.
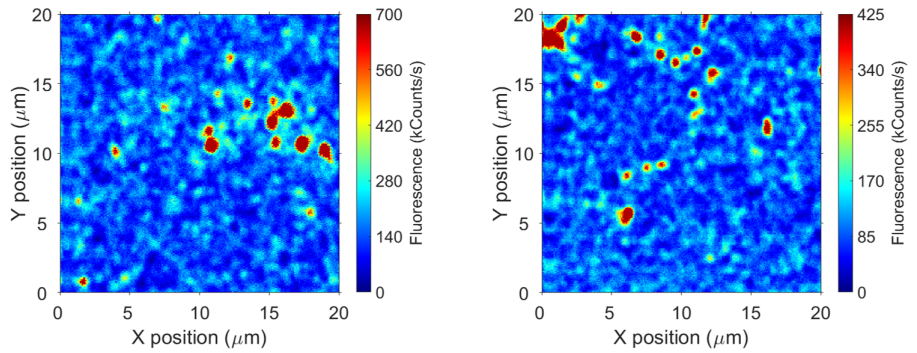
(c) RT confocal microscope images of samples (left) UU601-3 and (right) UU602-3.

Figure 3.1: RT confocal microscope images of (a) samples UU601-1 and UU602-1 (4 h annealing at 850 °C), (b) samples UU601-2 and UU602-2 (2 h annealing at 1200 °C) and (c) samples UU601-3 and UU602-3 (1 h annealing at 1500 °C). Single GeV sites can be resolved. The areas showing strong luminescence do not correspond to GeV centers.
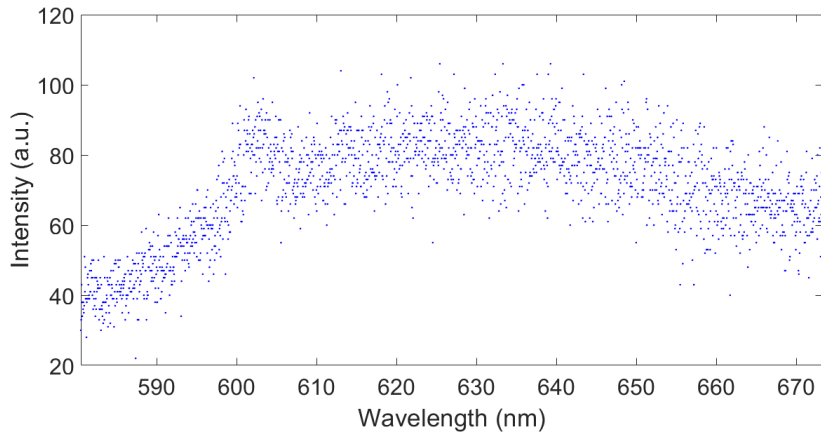
(a) RT GeV spectrum acquired from sample annealed at 850 °C for 4 hours.
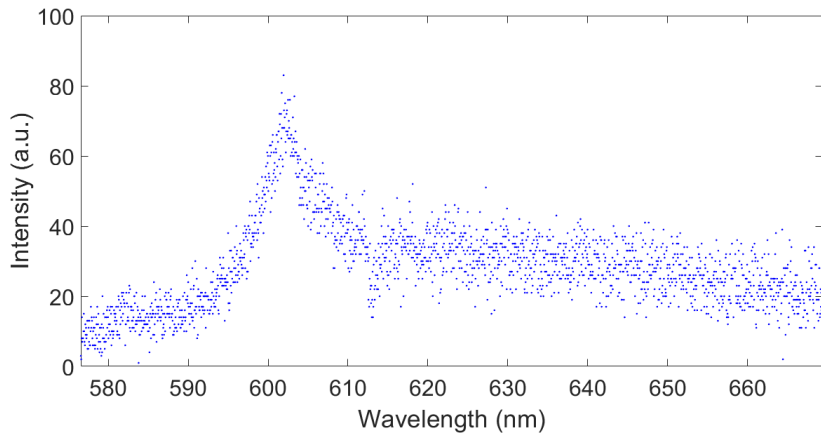
(b) RT GeV spectrum acquired from sample annealed at 1200 °C for 2 hours.
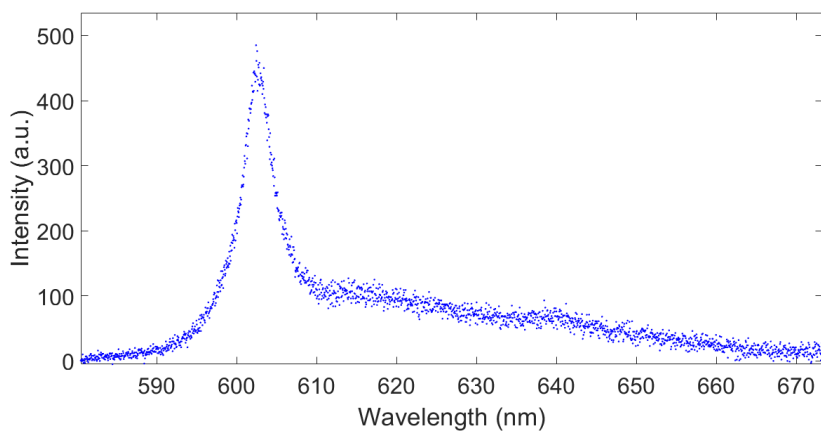
(c) RT GeV spectrum acquired from sample annealed at 1500 °C for 1 hour.

Figure 3.2: Examples of RT GeV spectra acquired from (a) sample UU602-1 (4 h annealing at 850 °C), (b) sample UU602-2 (2 h annealing at 1200 °C) and (c) sample UU602-3 (1 h annealing at 1500 °C). The characteristic RT GeV ZPL is visible in all three spectra, but it is more pronounced for high annealing temperatures.

Samples UU601-2 and UU602-2, as the previous samples, were annealed in two steps, both at 1200 °C for 1 hour. The presence of GeV centers was observed directly after the first annealing. The background present for samples UU601-1 and UU602-1 was present as well, but suppressed in comparison to the samples annealed at 850 °C. Examples of confocal maps are shown in figure 3.1b. The density and brightness of GeV sites also appeared to increase compared to the samples annealed at 850 °C. Similar results were obtained when measuring these two samples both after the first and the second annealing step at 1200 °C. However, the second treatment led to slightly improved optical features. Figure 3.2b shows an example of PL spectrum. Clearly, the ZPL line is more pronounced when compared to figure 3.2a. Moreover, the sample background reduced as well.

Samples UU601-3 and UU602-3, in comparison to the previous samples, were annealed at 1500 °C for 1 hour. The treatment led to increased density and brightness of the color centers, as shown in figure 3.1c. An example of PL spectrum is shown in figure 3.2c. Clearly the ZPL peak is generally sharper and more intense in comparison to the other cases. In addition, the background level is strongly reduced.

In order to compare the data obtained from measurements performed on the different samples, an analysis of the RT photoluminescence spectra is required. The relevant information is the ZPL peak position and corresponding line width. To extract the desired data, the acquired spectra were analyzed and fitted by means of a custom code implemented in the MATLAB software [87]. The fitting functions were chosen in a way that both ZPL and PSB are fitted, which allows to replicate the overall shapes of the spectra.

At room temperature, the inhomogeneous broadening causes a significant impact on ZPL line widths. Due to this, the line cannot be fitted by a simple Lorentzian profile. Instead, the Pseudo-Voigt profile might be used. In that regard, it is worth recalling that a (centered, i.e., peaked at zero) Voigt profile represents the convolution of a Lorentzian and a Gaussian profiles

$$V(x; \sigma, \gamma) \triangleq \int_{-\infty}^{+\infty} G(x'; \sigma) L(x - x'; \gamma) \, dx', \tag{3.1}$$

Where $G(x; \sigma)$ is the centered Gaussian profile and $L(x; \gamma)$ is the centered Lorentzian profile. The Gaussian profile centered in x_0 (mean or expectation of the distribution) is defined as follows

$$G(x; x_0, \sigma) \triangleq \frac{exp\left(-\frac{(x-x_0)^2}{2\sigma^2}\right)}{\sigma\sqrt{2\pi}}, \tag{3.2}$$

Where x is the shift from the line center and σ is the standard deviation of the distribution. The centered Lorentzian profile is

$$L(x; x_0, \gamma) \triangleq \frac{\gamma}{\pi((x - x_0)^2 + \gamma^2)}, \tag{3.3}$$

Where γ is the scale parameter, that specifies the half width at half maximum of the profile and x_0 is the location parameter, specifying the location of the peak of the distribution. In the present discussion, the Gaussian and Lorentzian components of the Voigt distribution would model the inhomogeneous and homogeneous broadening components of the color center's ZPL, respectively (see section 1.2). However, the implementation of a pure Voigt profile fit is challenging, due to the convolution integral of equation 3.1. Thus, it can be replaced by the normalized Pseudo-Voigt profile, which has a high level of accuracy and can be implemented more easily [88]. The Pseudo-Voigt profile can be written as

$$V_p(x; f) \triangleq \eta \cdot L(x; f) + (1 - \eta) \cdot G(x; f), \tag{3.4}$$

That is a linear combination of the Gaussian and Lorentzian curves instead of their convolution, with $\eta \in [0, 1]$ specifying the Lorentzian fraction making up the overall Pseudo-Voigt distribution and f total FWHM of the profile.

The PBS profile, as discussed in section 1.2, has a Poissonian character, that is well approximated by a Gaussian line shape at RT. However, unlike the standard normal distribution, which is always symmetric, the Poisson distribution can either be symmetric or asymmetric, depending on the value of its mean. A Poisson distribution with low mean is usually highly skewed, but if the mean is larger, the distribution spreads out and becomes more symmetric. To take this feature into account and avoid any loss of generality of the utilized model, a skewed Gaussian line shape (skew-normal distribution) was chosen to reproduce the shape of the PSB. The probability density function of a skew-normal distribution centered in x_0 is given by

$$G_S(x; x_0, \sigma; \beta) \triangleq \left(\frac{exp\left(-\frac{(x - x_0)^2}{2\sigma^2}\right)}{\sigma\sqrt{2\pi}} \right) \left(1 + erf\left(\frac{\beta(x - x_0)}{\sigma\sqrt{2}} \right) \right), \tag{3.5}$$

Where erf is the error function and $\beta \in (-\infty, +\infty)$ is a parameter related to the skewness of the distribution, i.e., a larger absolute value of the β parameter results in larger skewness of the distribution. The asymmetric Gaussian line shape reduces to a symmetric

Gaussian when $\beta = 0$.

Taking into account the considerations given above, in the present work the function below was used to fit the RT spectra

$$
\begin{aligned}
H \cdot \alpha \cdot ((1 - f_G) \cdot L(x; x_0, \gamma_0) + f_G \cdot G(x; x_0, \gamma_0)) + \\
+ H \cdot (1 - \alpha) \cdot G_S(x; x_1, \gamma_1; \beta),
\end{aligned}
\tag{3.6}
$$

Where the first and second line of equation 3.6 model the Germanium-Vacancy ZPL and PSB, respectively and:

- H is an amplitude parameter and can take any value in the interval $(0, +\infty)$.

- α is related to the percentage of light emitted into the GeV ZPL and can thus take any value in the interval $[0, 1]$.

- f_G is the Gaussian fraction in the Pseudo-Voigt profile used to model the ZPL part of the spectrum (it plays the role of the parameter $(1 - \eta)$ of equation 3.4) and can take any value in the interval $[0, 1]$.

- x_0 represents the center position of the peak of the ZPL in nm.

- γ_0 represents the FWHM of the ZPL in nm (it corresponds to the parameter f of equation 3.4).

- x_1 represents the center position of the peak of the PSB in nm, assuming symmetric Gaussian profile (i.e., for $\beta = 0$).

- γ_1 represents the standard deviation of the PSB asymmetric Gaussian distribution in nm (it corresponds to the parameter σ of equation 3.5).

- β is the shape parameter of the PSB asymmetric Gaussian profile, determining its skewness, and can take any value in the interval $(-\infty, +\infty)$.

The fitting function in equation 3.6 was used to analyze the GeV spectra collected from each sample. As mentioned before, it was not possible to record any GeV spectrum from samples UU601-1 and UU602-1 after the first annealing step. Thus, results for the second annealing step only are reported. Concerning samples UU601-2 and UU602-2, several GeV spectra were obtained from those samples after the first annealing treatment. However, the number of spectra was not sufficient to perform any statistical analysis. Hence, results for the second annealing step only are presented for those two samples as well. The results are shown in figure 3.3 and figure 3.4. From the obtained data, the average peak positions λ_0 and line widths $\Delta\lambda$ of the ZPLs were retrieved and they are summarized in table 3.1.
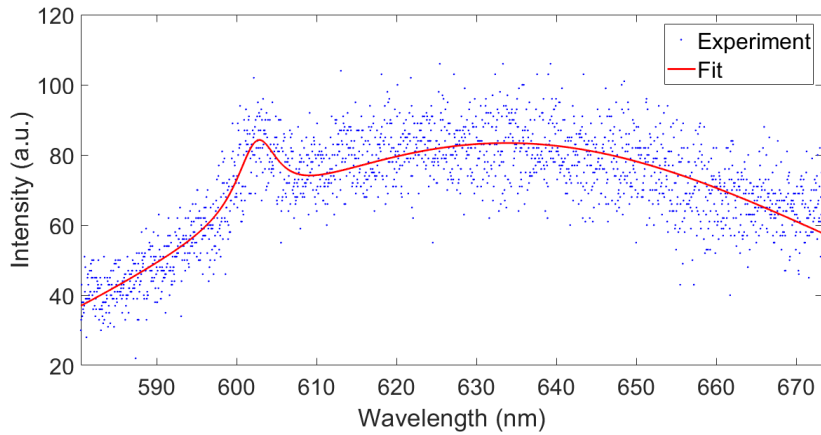
(a) GeV RT spectrum acquired from sample annealed at 850 °C for 4 hours (blue dotted line) and corresponding fit (red solid line).
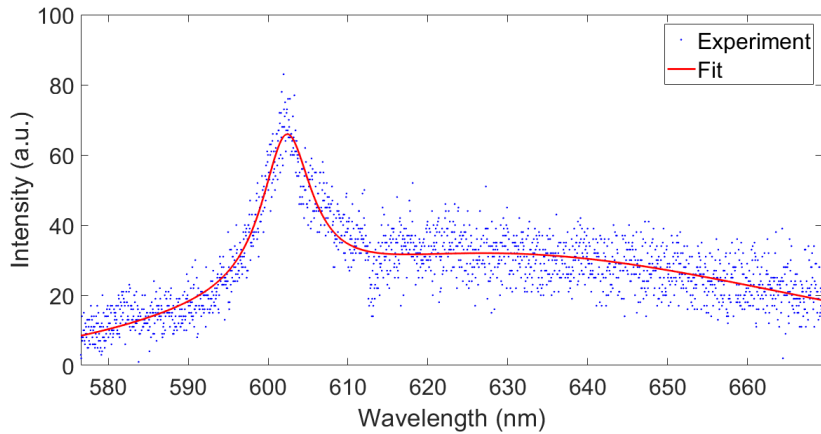
(b) GeV RT spectrum acquired from sample annealed at 1200 °C for 2 hours (blue dotted line) and corresponding fit (red solid line).
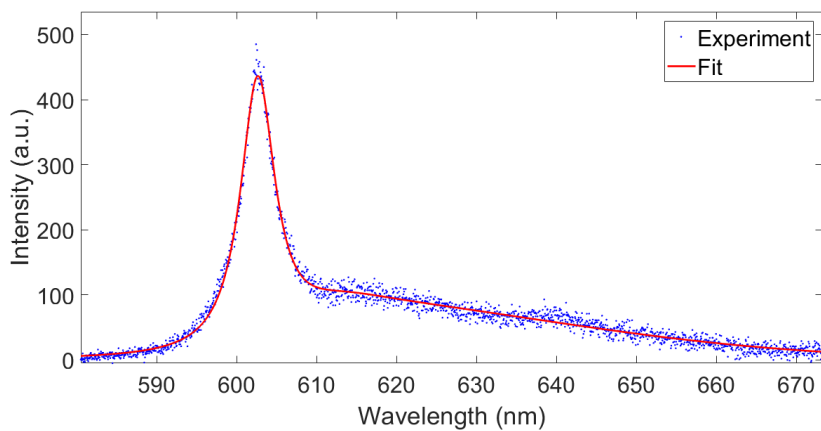
(c) GeV RT spectrum acquired from sample annealed at 1500 °C for 1 hour (blue dotted line) and corresponding fit (red solid line).

Figure 3.3: Examples of RT GeV spectra and corresponding fit for (a) sample UU602-1 (4 h annealing at 850 °C), (b) sample UU602-2 (2 h annealing at 1200 °C) and (c) sample UU602-3 (1 h annealing at 1500 °C).
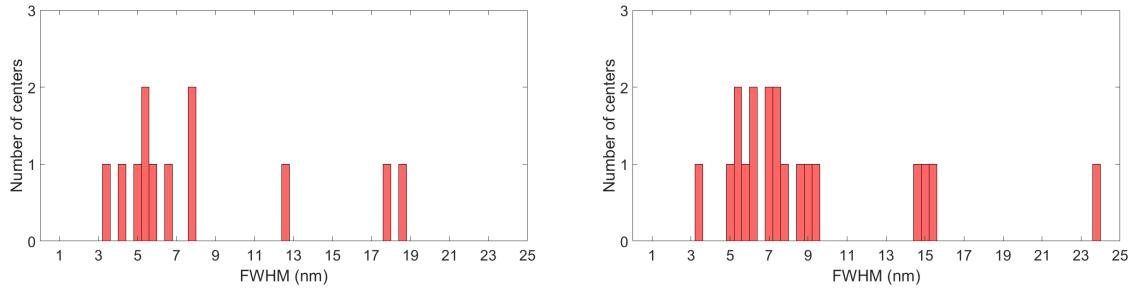
(a) Histograms of FWHMs $\boldsymbol{\Delta\lambda}$ of the fitted RT ZPLs for samples (left) UU601-1 (4 h annealing) and (right) UU602-1 (4 h annealing).
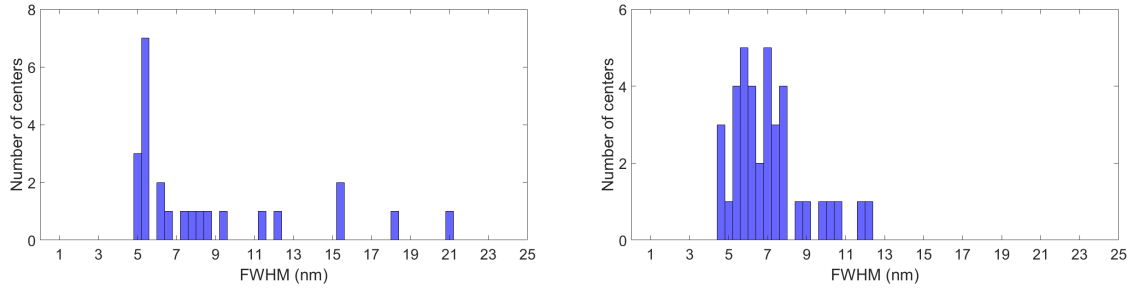
(b) Histograms of FWHMs $\boldsymbol{\Delta\lambda}$ of the fitted RT ZPLs for samples (left) UU601-2 (2 h annealing) and (right) UU602-2 (2 h annealing).
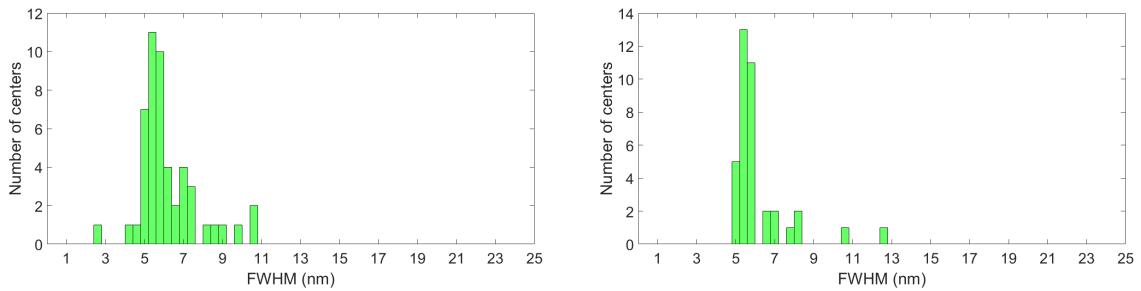
(c) Histograms of FWHMs $\boldsymbol{\Delta\lambda}$ of the fitted RT ZPLs for samples (left) UU601-3 and (right) UU602-3.

Figure 3.4: Histograms of FWHMs $\boldsymbol{\Delta\lambda}$ of the fitted RT ZPLs for GeV emitters within (a) samples UU601-1 and UU602-1 (4 h annealing at 850 °C), (b) samples UU601-2 and UU602-2 (2 h annealing at 1200 °C) and (c) samples UU601-3 and UU602-3 (1 h annealing at 1500 °C). GeV centers measured in samples annealed at 1500 °C show narrower inhomogeneous distributions of the ZPL FWHMs.

Table 3.1

Sample	Treatment	Average ZPL peak position λ_0 (nm)	Average ZPL FWHM $\Delta\lambda$ (nm)
UU601-1	850 °C 4h	**602.55 ± 1.96**	**8.39 ± 5.14**
UU601-2	1200 °C 2h	**603.63 ± 2.16**	**8.61 ± 4.65**
UU601-3	1500 °C 1h	**603.05 ± 1.26**	**6.19 ± 1.55**
UU602-1	850 °C 4h	**603.87 ± 1.94**	**8.96 ± 4.97**
UU602-2	1200 °C 2h	**602.40 ± 1.41**	**7.02 ± 1.95**
UU602-3	1500 °C 1h	**602.86 ± 0.49**	**6.15 ± 1.56**

Table 3.1: Average RT ZPL peak position λ_0 and FWHM $\Delta\lambda$ in nm for the six measured samples, resulting from the statistical analysis performed on the acquired RT GeV spectra. The spectra were fitted using the fit model reported in equation 3.6.

The room temperature experiments give a first overview on the formation of GeV centers in diamond following different treatments. In the low temperature annealing (850 °C) case, short annealing time (1 hour) is insufficient for formation of GeVs. Increasing the annealing time to a total of 4 hours leads to formation of centers. However, the PL spectroscopy shows that GeV emission is accompanied by strong background contributions. The presence of the background signal can be detected through the entire samples, indicating strong radiation damage that cannot be recovered by annealing at 850 °C. Thus, one can expect that the properties of the formed GeVs would be strongly affected by their surroundings, e.g., local strain. High strain results in the GeV centers being subject to slightly different local crystal environments, which modify the atomic structure of the defects. Thus, GeV centers will show different spectroscopic properties, i.e., shift in the GeV ZPL peak position and broad line widths, due to inhomogeneous broadening. This is confirmed by the obtained values of $\Delta\lambda$, which are larger compared to the other samples.

Increasing the annealing temperature leads to more efficient GeV formation. Indeed, even after 1 hour of annealing at 1200 °C, clear evidence of GeV color centers formation is observed. Both confocal microscopy and PL spectroscopy show reduced background compared to lower annealing temperature. The average line widths and ZPL peak positions still indicate the presence of high local strain. Moreover, the situation is only slightly improved when increasing the annealing time.

The samples annealed at temperatures of 1500 °C show a large number of bright GeVs. The PL spectra show prominent ZPLs and strongly suppressed background. Clearly, the GeV centers of samples UU601-3 and UU602-3 have narrower inhomogeneous distributions of the ZPL FWHMs than those produced in all the other samples. Moreover, the average line widths are in good agreement with what expected based on the results reported in previous works on GeV centers [74, 89]. This indicates reduced strain in the samples annealed at 1500 °C [74], i.e., better recovery of the implantation damage.

It is also worth pointing out that the implantation depth of the Ge ions does not play any significant role in determining the RT spectral features in all cases. The obtained average values for $\boldsymbol{\Delta\lambda}$ are comparable for samples subject to the same annealing treatments, irrespective of the depth of the implanted Ge ions. Minor differences can be attributed to the goodness of the collected data and statistical analysis itself.

3.1.2. Low temperature photoluminescence spectroscopy

Low temperature (LT) spectroscopy was performed on the samples after each annealing treatment. However, compared to the RT experiments, samples UU601-1 and UU602-1 were not measured after the first annealing step as the corresponding RT investigations did not show any presence of GeV centers. Hence, a total of 8 LT spectroscopy experiments were performed. The experiments were performed at a temperature T = 4 K using off-resonant 532 nm excitation at a power of $\boldsymbol{\approx}$ 500 $\boldsymbol{\mu}$W. The measurements were taken in the same corners of the L-shaped marked regions of the samples (refer to figures 2.1 and 2.2) probed in the RT spectroscopy measurements, following the exact same procedure in choosing the sub-regions to be investigated.

Samples UU601-1 and UU602-1. As in the case of RT spectroscopy, the confocal scans reveal the presence of GeV centers (see figure 3.5a). Single sites are clearly resolved. The PL spectra show characteristic spectral features of GeV color centers, i.e., lines close to 602 nm corresponding to C and D transitions (see section 1.3.3). However, the strong background, related to the lattice damage, contributes to the spectra. Moreover, from center to center, the peak positions appear to be strongly shifted in wavelength from the expected 602 nm. An example of spectrum is shown in figure 3.6a, where both GeV ZPL C and D transitions and the background contribution are visible.

Samples UU601-2 and UU602-2 were investigated after each annealing step and the presence of GeV defects was observed in all cases. Examples of confocal images are shown in figure 3.5b. The acquired spectra show clear signatures of GeV, see figure 3.6b. In comparison to the samples annealed at 850 °C, the background reduces, similarly to the

RT observations. In addition, the GeV ZPL peak positions appear to be closer to the expected 602 nm than for samples UU601-1 and UU602-1. Moreover, the peak centers are less separated.

(a) LT confocal microscope images of samples (left) UU601-1 and (right) UU602-1.

(b) LT confocal microscope images of samples (left) UU601-2 and (right) UU602-2 .

(c) LT confocal microscope images of samples (left) UU601-3 and (right) UU602-3.
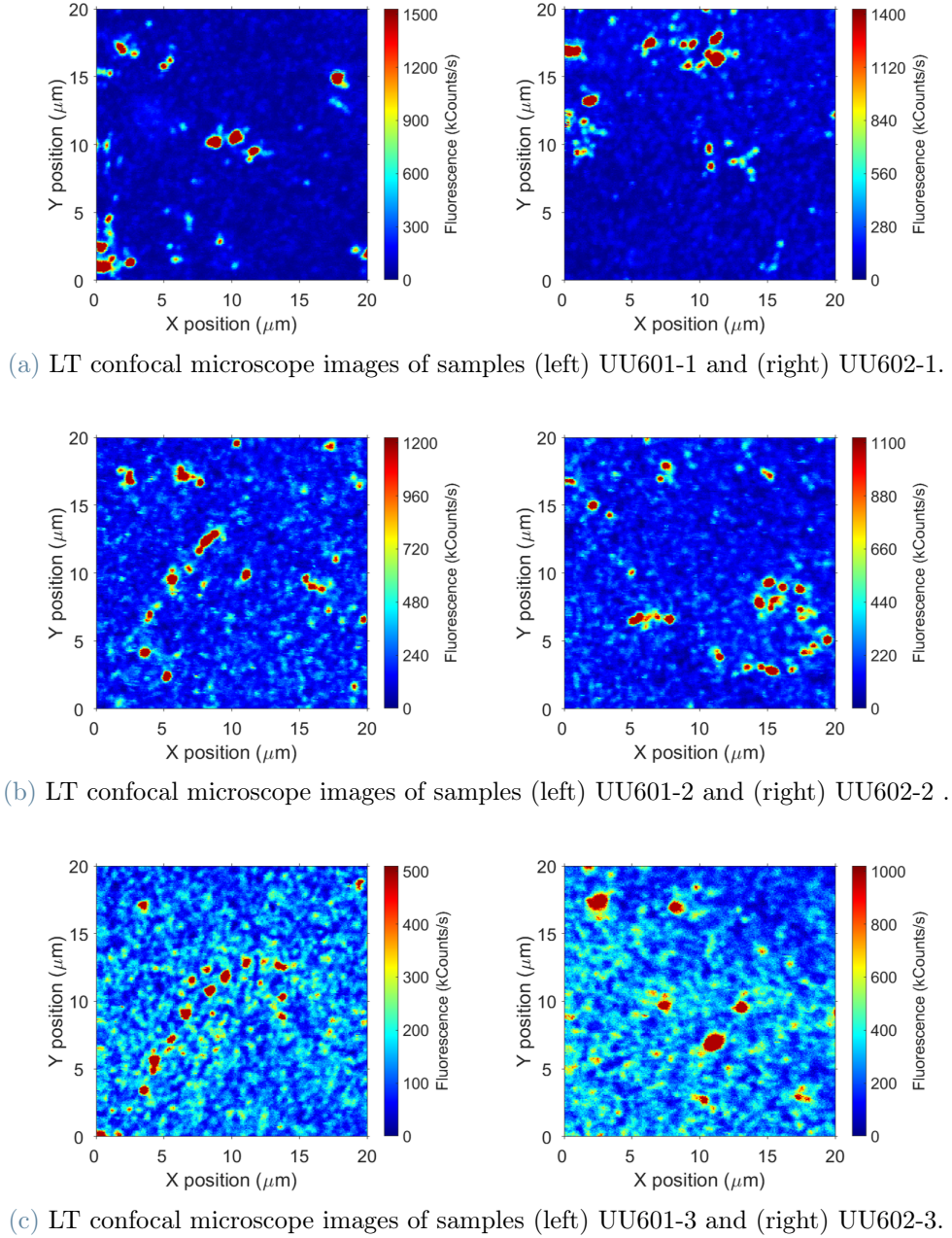
Figure 3.5: LT confocal microscope images of (a) samples UU601-1 and UU602-1 (4 h annealing at 850 °C), (b) samples UU601-2 and UU602-2 (2 h annealing at 1200 °C) and (c) samples UU601-3 and UU602-3 (1 h annealing at 1500 °C), which reveal the presence of single GeV color centers. The density of created emitters increases with increasing annealing temperature.
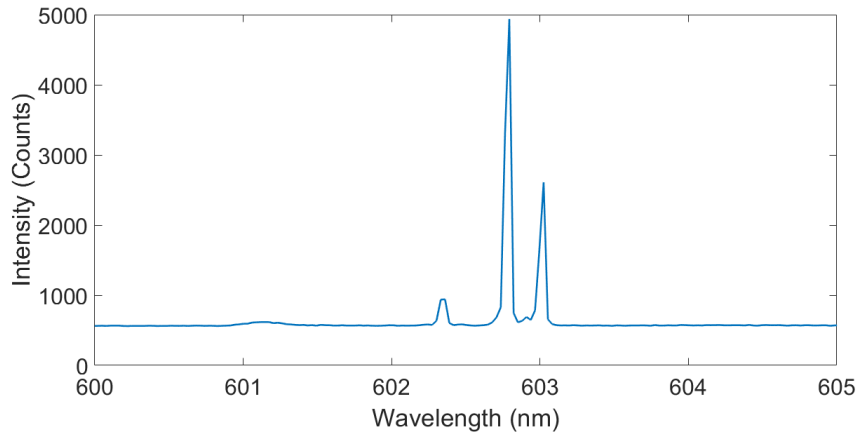
(a) LT GeV spectrum acquired from sample annealed at 850 °C for 4 hours.
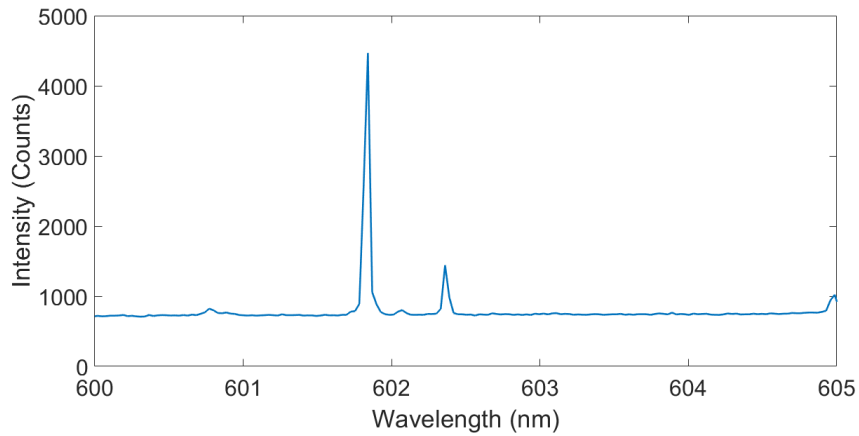
(b) LT GeV spectrum acquired from sample annealed at 1200 °C for 2 hours.
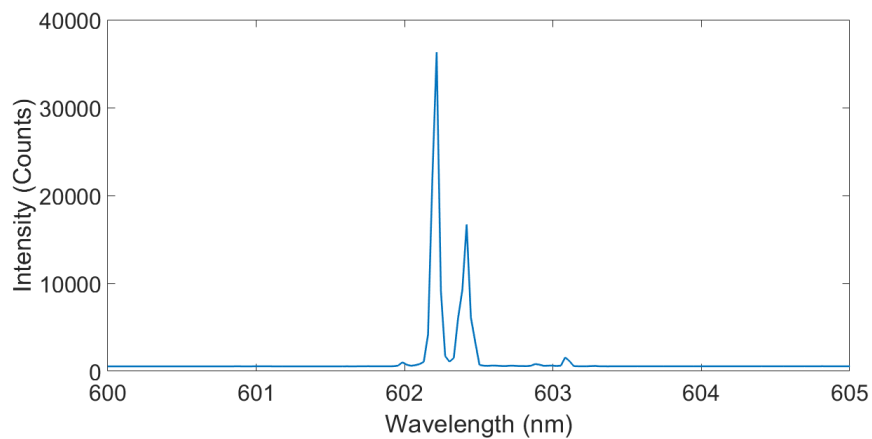
(c) LT GeV spectrum acquired from sample annealed at 1500 °C for 1 hour.

Figure 3.6: Examples of LT GeV spectra acquired from (a) sample UU602-1 (4 h annealing at 850 °C), (b) sample UU601-2 (2 h annealing at 1200 °C) and (c) sample UU602-3 (1 h annealing at 1500 °C). The C and D transitions of the GeV ZPL are clearly visible in all three spectra. The spectra acquired from samples annealed at T $\leq$ 1200 °C show a strong damage-related background.

Samples UU601-3 and UU602-3. The acquired confocal images show significantly higher density of GeV centers and higher PL yield, compared to the samples annealed at lower temperatures (see figure 3.5c). An example of PL spectrum is shown in figure 3.6c. The collected spectra generally show no damage-related background and ZPL peaks very close to 602 nm. Moreover, the peak positions are close to each other for different centers. Multiple spectra exhibit multiple GeV optical features, as shown in figure 3.7.
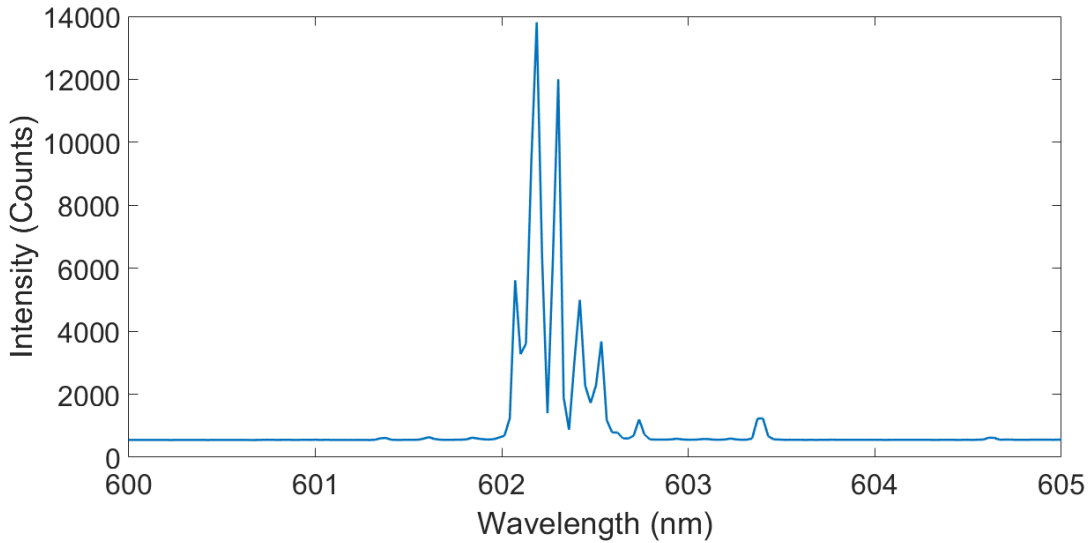
Figure 3.7: LT GeV spectrum acquired from sample UU601-3: optical features of several GeV emitters are visible.

The PL spectra recorded at low temperature allow to obtain the frequency difference of C and D transitions, that corresponds to the ground state splitting ΔSO_g discussed in section 1.3.4. In order to evaluate the ΔSO_g values for the different samples, the C and D peak positions of the probed single emitters were extracted from the acquired spectra to evaluate the histograms of inhomogeneous distributions. The widths of the distributions provide information on the similarity of the defects [49]. The histograms were built and analyzed using a custom code implemented in MATLAB, with a frequency bin width of 26 GHz, chosen to resemble the resolution of the spectrometer. Only the (background-corrected) spectra that clearly showed two peaks in the region of interest were kept and included in the statistical analyses.

In the case of the samples annealed at 850 °C and 1200 °C, the obtained transition frequency distributions have very wide widths > 100 GHz in all cases, regardless of the annealing treatment duration and implantation depth of the Ge ions (see figure 3.8). This indicates strong differences in the properties of the created emitters.
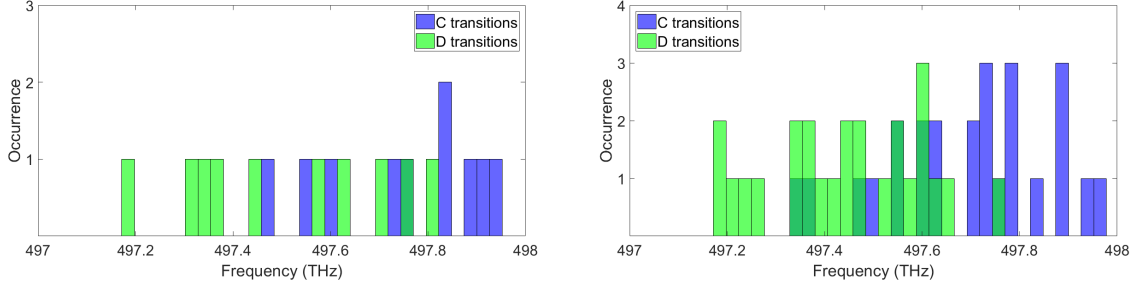
(a) GeV C and D transitions in samples (left) UU601-1 (4 h annealing) and (right) UU602-1 (4 h annealing).
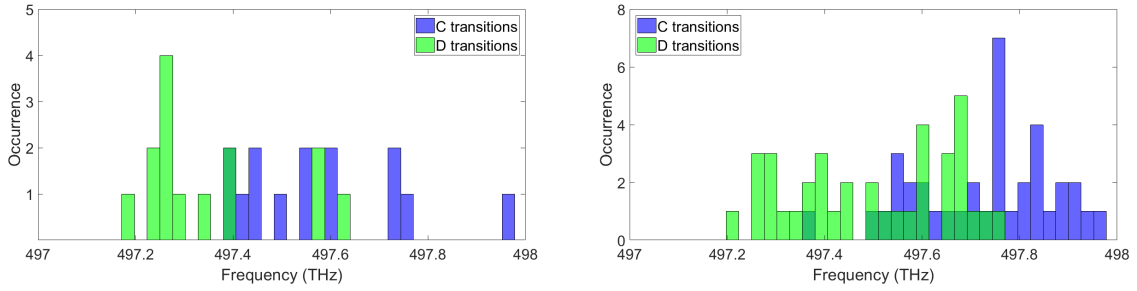
(b) GeV C and D transitions in samples (left) UU601-2 (1 h annealing) and (right) UU602-2 (1 h annealing).
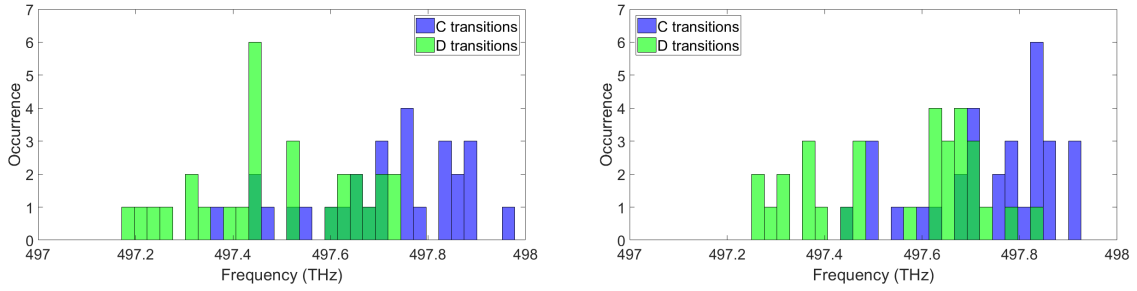
(c) GeV C and D transitions in samples (left) UU601-2 (2 h annealing) and (right) UU602-2 (2 h annealing).
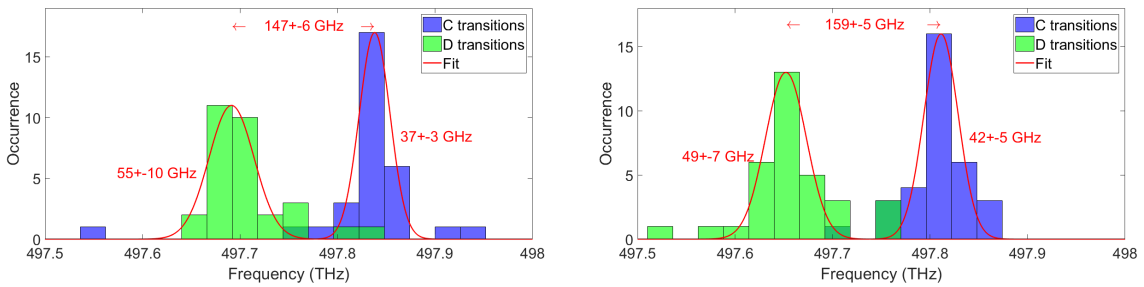
(d) GeV C and D transitions in samples (left) UU601-3 and (right) UU602-3 and corresponding fits.

Figure 3.8: Histograms (26 GHz bin width) of C and D transition frequencies for GeV centers in (a) samples UU601-1 and UU602-1 (4 h annealing at 850 °C), (b) samples UU601-2 and UU602-2 (1 h annealing at 1200 °C), (c) samples UU601-2 and UU602-2 (2 h annealing at 1200 °C) and (d) samples UU601-3 and UU602-3 (1 h annealing at 1500 °C). Higher annealing tempertures result in narrower widths of the inhomogeneous distributions of transition frequencies and smaller ground state splittings ΔSO_g.

On the other hand, the same analysis performed on samples UU601-3 and UU602-3 revealed narrow distributions of transition frequencies, shown in figure 3.8d. Based on Gaussian fits, the obtained histograms show transition frequency distributions having widths around 40 GHz. Moreover, the calculated values of $\mathbf{\Delta}SO_g$ are close to the low-strain reference splitting of 152 GHz. The obtained ground state splittings $\mathbf{\Delta}SO_g$ are summarized in table 3.2.

Table 3.2

Sample	Treatment	Average ground state splitting $\mathbf{\Delta}SO_g$ (GHz)
No strain		$152^{[75]}$
UU601-1	850 °C 4h	$\mathbf{334 \pm 72}$
UU601-2	1200 °C 1h	$\mathbf{262 \pm 35}$
UU601-2	1200 °C 2h	$\mathbf{252 \pm 49}$
UU601-3	1500 °C 1h	$\mathbf{147 \pm 6}$
UU602-1	850 °C 4h	$\mathbf{261 \pm 39}$
UU602-2	1200 °C 1h	$\mathbf{246 \pm 41}$
UU602-2	1200 °C 2h	$\mathbf{214 \pm 43}$
UU602-3	1500 °C 1h	$\mathbf{159 \pm 5}$

Table 3.2: Average calculated ground state splitting $\mathbf{\Delta}SO_g$ for the investigated samples as well as low-strain reference value [75].

The results achieved by low temperature photoluminescence spectroscopy support the findings obtained at room temperature. In the low temperature annealing cases, strong shift of ZPL peak positions for different centers and presence of large number of implantation defects which are not relieved by the annealing treatments are observed. That indicates a high longitudinal strain environment of GeV centers [90]. Increasing the annealing temperature leads to improvement of the environments surrounding the GeV centers, e.g., the C and D peaks concentrate close to 602 nm. In contrast to the RT spectroscopy, the measurements at cryogenic temperature provide an estimation of strain. The ground state splittings $\mathbf{\Delta}SO_g$ are related to transversal strain [49]. The gradual decrease of $\mathbf{\Delta}SO_g$ is reported in table 3.2. For the samples annealed at low temperature, the value of $\mathbf{\Delta}SO_g$ is almost a factor of two larger than the reported splitting of non-strained GeVs. At

higher annealing temperature, the average ground state splitting approaches the reported value of 152 GHz. Thus, samples annealed at 1500 °C have low transversal strain, indicating that these temperatures are beneficial for formation of high quality GeV centers. In addition, LT and RT measurements indicate an increase in the formation yield of Germanium-Vacancy centers at higher annealing temperatures. This is observable from the intense and dense confocal scans (see figures 3.1 and 3.5) and, in addition, several spectra obtained at LT show multiple peaks around 602 nm for high annealing temperatures (figure 3.7), thus indicating the presence of several emitters within the illuminated volume.

As in the case of RT investigations, no significant impact of implantation depth of Ge ions on the properties of the created GeV centers has been observed. The obtained average values of ΔSO_g for samples subject to analogous annealing treatments are comparable, regardless of the depth of the implanted Ge ions.

3.2.   Photoluminescence Excitation spectroscopy

The Photoluminescence Excitation measurements were performed at T = 4 K for all samples after each annealing step, except the first annealing of samples UU601-1 and UU602-1, since no GeV centers were observed. For the experiments, the wavelength of the excitation laser was tuned in each case to the wavelength of the C optical transition of the emitter, recorded in the corresponding GeV low temperature PL spectrum. The laser wavelength was then scanned around the transition to reconstruct the full PLE spectrum for the investigated emitter. To that purpose, the fluorescence in the PSB was recorded. PLE spectra are indeed typically measured on a carefully filtered sideband to eliminate the dominant laser light. The line widths of the measured PLE spectra were fitted with Lorentzian functions implemented in MATLAB. The same regions of the samples were investigated as in the experiments discussed above (sections 3.1.1 and 3.1.2).

In order to find the transition frequency of the probed color center, each experiment was first performed with the help of the off-resonant 532 nm light in addition to the resonant excitation. A low-power off-resonant excitation is introduced to the GeVs during resonant excitation to stabilize the GeV charge state. Recording PLE spectra without charge stabilization might be complicated, since changes in the charge state of the emitters quench the fluorescence [91]. However, the use of this method causes spurious effects such as spectral diffusion (see figure 3.9), deteriorating the spin-photon interfaces formed with the defects [92] as spectral jumps appear to degrade the fidelity of optical control of the emitters [93]. Therefore, after recording the PLE spectra, the same measurements were repeated with resonant excitation only. This allows to probe the spectral stability of the color centers.

Both resonant and off-resonant excitations were initially tuned to powers of ≈ 100 nW, then to ≈ 10 nW, to finally switch off the 532 nm light and repeat with powers down to ≈ 1 nW of resonant excitation light only to avoid phenomena such as blinking (see figure 3.10) and power broadening of the transition line widths (see equation 1.7) [26]. Examples of PLE spectra obtained in this way are shown in figure 3.11 for a GeV center in sample UU601-3. Clearly, the transition line width is decreasing with decreasing excitation power, whereas the peak center does not change.
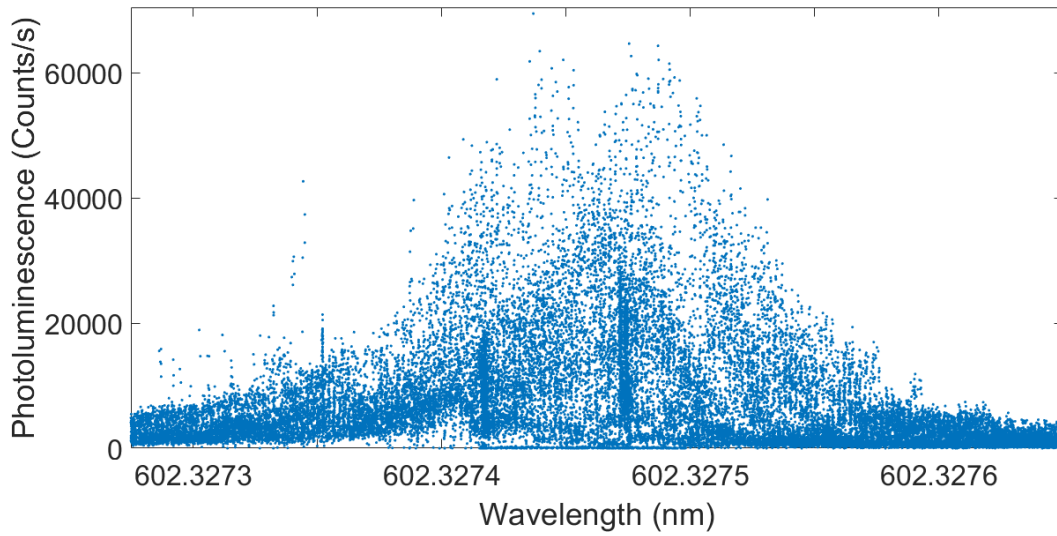
Figure 3.9: PLE spectrum of a GeV center found in sample UU602-3, investigated with ≈ 100 nW of resonant laser light plus ≈ 100 nW of green off-resonant repump. The emitter is affected by spectral diffusion (it switches between two discrete resonance frequencies), possibly product as a side effect of using the charge-stabilizing repump excitation [92].
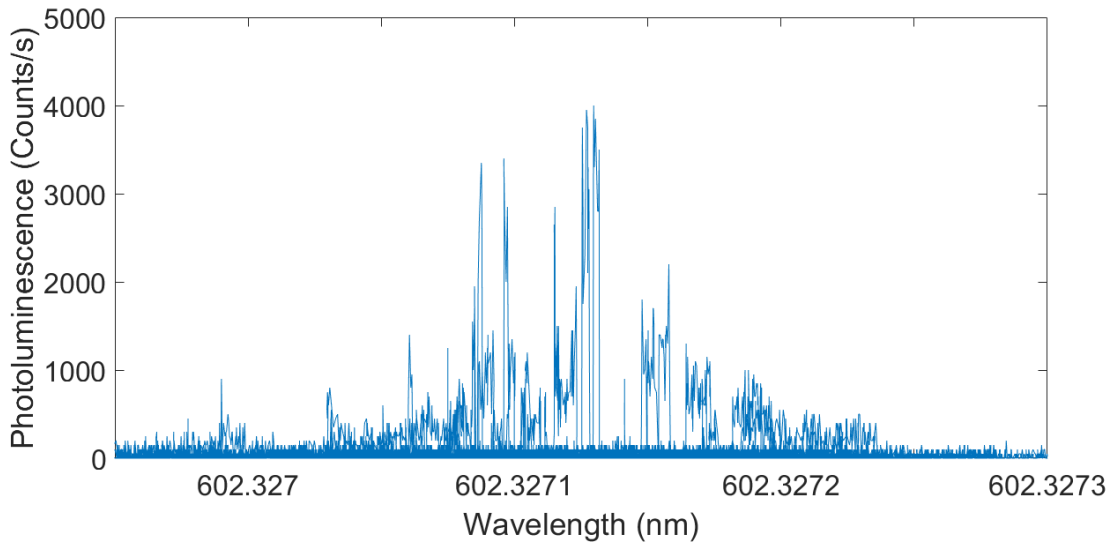
Figure 3.10: PLE spectrum of a GeV center found in sample UU602-2 (1 h annealing at 1200 °C), recorded with ≈ 1 nW of resonant laser light only. The probed emitter is affected by the blinking effect (fluorescence intermittence) and, therefore, it is not spectrally stable.
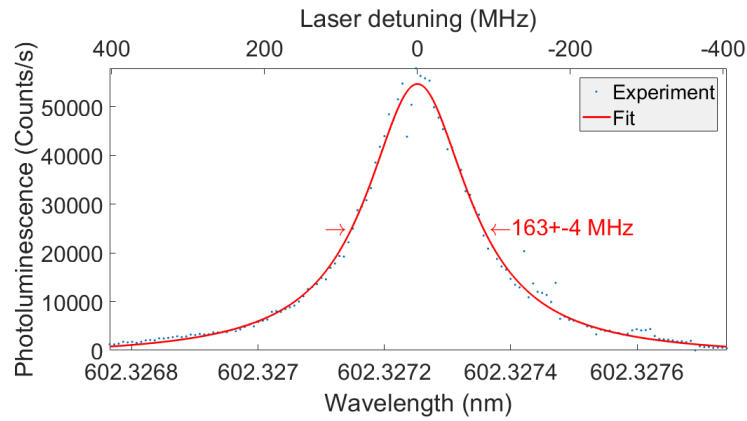
(a) GeV PLE spectrum acquired using ≈ 100 nW of resonant and ≈ 100 nW of off-resonant excitation.
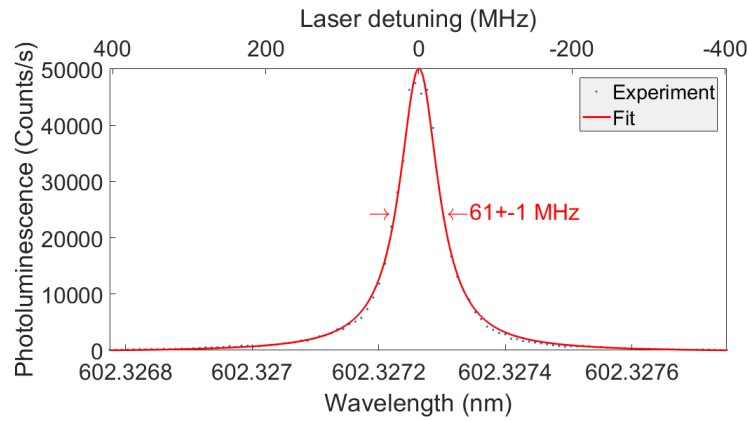
(b) GeV PLE spectrum acquired using ≈ 10 nW of resonant and ≈ 10 nW of off-resonant excitation.
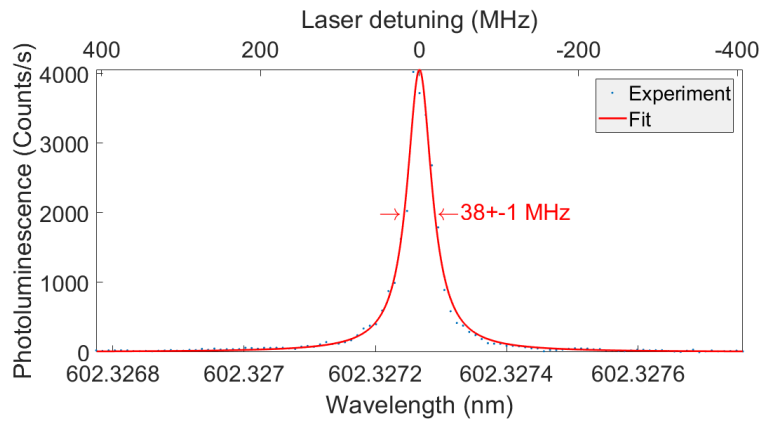
(c) GeV PLE spectrum acquired using ≈ 1 nW of resonant excitation only.

Figure 3.11: PLE spectra (blue dots) of a GeV center within sample UU601-3 and corresponding Lorentzian fits (red lines) for (a) high-power resonant plus off-resonant excitation, (b) mid-power resonant plus off-resonant excitation and (c) low-power resonant excitation only. Power broadening of the line width is observed.

Samples UU601-1 and UU602-1 were measured after 4 hours of annealing at 850 °C. No PLE spectra could be recorded in the case of sample UU601-1, probably due to severe spectral instability. In the case of sample UU602-1, one center was spectrally stable that few PLE spectra could be recorded. However, the center showed strong blinking behaviour, which was observed to be more pronounced for higher excitation power. One of the recorded PLE spectra showed a line width of $\mathbf{285 \pm 24}$ MHz for ≈ 1 nW of resonant excitation light only.

Samples UU601-2 and UU602-2. The first measurements on these samples were performed after 1 hour of annealing at 1200 °C. In the case of sample UU601-2, several emitters were not spectrally stable enough to record any PLE spectra, as they showed strong blinking and/or bleaching behaviour. Only one center was spectrally stable, and the relative PLE spectrum, acquired using ≈ 1 nW of resonant excitation light only, showed a line width of $\mathbf{77 \pm 5}$ MHz. Similar results were recorded for sample UU602-2. Some centers showed strong blinking behaviour (see figure 3.10), as well as spectral diffusion. However, three emitters were resonantly excited by ≈ 1 nW of orange light only and spectrally stable. The recorded PLE spectra have line widths of $\mathbf{180 \pm 55}$ MHz, $\mathbf{109 \pm 11}$ MHz and $\mathbf{72 \pm 6}$ MHz, respectively. The last one shows the narrowest line width among the three measured centers and similar to the one observed in sample UU601-2. Moreover, more centers were resonantly excited compared to the previous samples at approximately the same excitation wavelength, which is an indication of similarity of the created emitters. The measurements were repeated after 1 additional hour of annealing at 1200 °C. The additional annealing step did not produce any significant effect on the spectral stability properties of the emitters and the line widths of the measured PLE spectra. Blinking and bleaching behaviours were still observed in both samples, as well as spectral diffusion. However, the number of stable emitters increased for both samples. Regarding sample UU601-2, three emitters were resonantly excited by ≈ 1 nW of resonant excitation at approximately the same excitation wavelength used in all the other measurements and stable enough to record the corresponding PLE spectra, having line widths of $\mathbf{68 \pm 6}$ MHz, $\mathbf{112 \pm 13}$ MHz and $\mathbf{187 \pm 28}$ MHz, respectively. For sample UU602-2, PLE spectra were recorded for five GeV centers (line widths: $\mathbf{146 \pm 20}$ MHz, $\mathbf{70 \pm 5}$ MHz, $\mathbf{197 \pm 26}$ MHz, $\mathbf{97 \pm 9}$ MHz and $\mathbf{110 \pm 4}$ MHz). Clearly, in both cases, the narrowest measured line widths did not change with respect to the ones measured before the additional annealing step. However, the additional annealing treatment led to formation of more spectrally stable centers with resonance at approximately the same excitation frequency. This is illustrated in figure 3.12, where all the confocal scans were acquired at a fixed wavelength. Clearly, several centers show response to the resonant excitation in the 1200 °C annealing case.
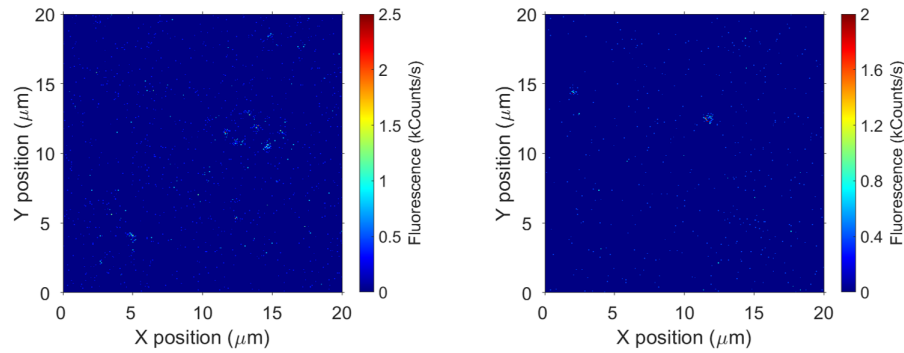
(a) Confocal microscope images of samples (left) UU601-1 (4 h annealing) and (right) UU602-1 (4 h annealing), acquired with resonant plus off-resonant excitation light.
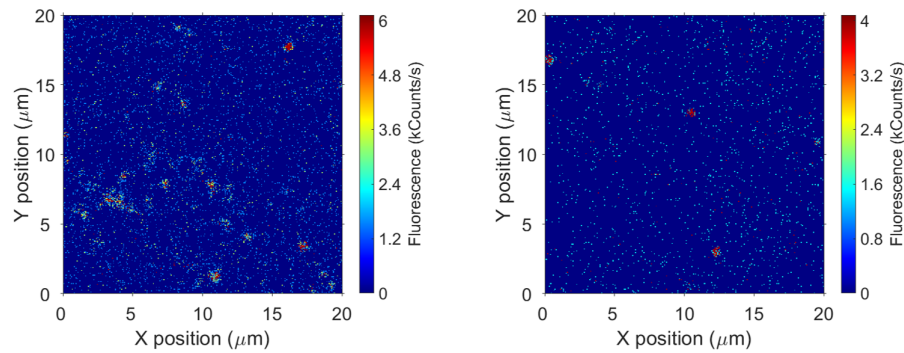
(b) Confocal microscope images of samples (left) UU601-2 (2 h annealing) and (right) UU602-2 (2 h annealing), acquired with resonant plus off-resonant excitation light.
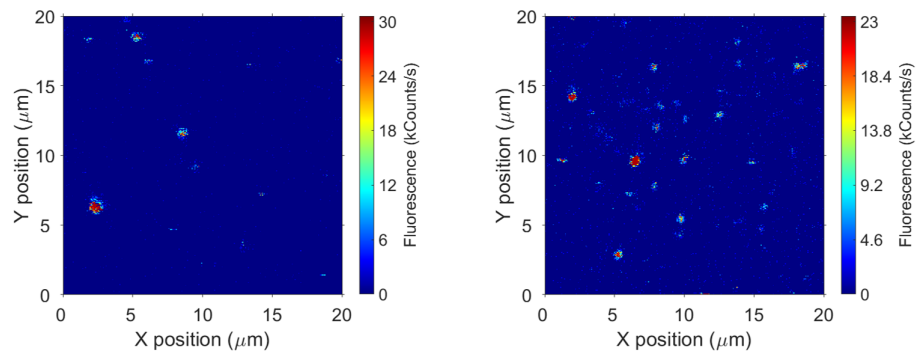
(c) Confocal microscope images of samples (left) UU601-3 and (right) UU602-3, acquired with resonant plus off-resonant excitation light.

Figure 3.12: Confocal microscope images of (a) samples UU601-1 and UU602-1 (4 h annealing at 850 °C), (b) samples UU601-2 and UU602-2 (2 h annealing at 1200 °C) and (c) samples UU601-3 and UU602-3 (1 h annealing at 1500 °C), acquired with resonant plus off-resonant excitation laser light. Multiple GeV centers show bright resonant excitation within the samples annealed at 1500 °C.

Samples UU601-3 and UU602-3. The blinking, bleaching and spectral diffusion (see figure 3.9) phenomena appeared to be strongly reduced for these two samples. A larger number of spectrally stable centers and significantly narrower PLE line widths were observed. An enhancement of the number of fluorescing centers was also visible in resonant confocal scans at fixed resonant excitation wavelength (figure 3.12c). In the case of sample UU601-3, five emitters were resonantly excited by ≈ 1 nW of orange light only, still using approximately the same excitation wavelength. The PLE spectra have line widths: **38 ± 1** MHz in figure 3.13, **81 ± 8** MHz, **61 ± 6** MHz, **85 ± 10** MHz and **91 ± 11** MHz. For sample UU602-3, the same behaviour was observed for six GeV centers (line widths: **38 ± 2** MHz in figure 3.14, **50 ± 5** MHz, **51 ± 3** MHz, **113 ± 8** MHz, **74 ± 4** MHz and **67 ± 4** MHz). The observed centers show spectral stability for up to ten minutes at least, which is traced by repetitive scanning over the resonances, see figures 3.13 and 3.14. Note that the centers blinked during the scans. This can be attributed to changes in the charge state of GeV [92]. However, the charge state (and consequently luminescence) is recovered under resonant excitation only. The narrowest recorded PLE line widths $\mathbf{\Delta\nu}_{\min}$ in MHz for the investigated samples are reported in table 3.3.

Table 3.3

Sample	Treatment	Narrowest PLE line width $\mathbf{\Delta\nu}_{\min}$ (MHz)
Lifetime-limited		26[26]
UU601-1	850 °C 4h	-
UU601-2	1200 °C 1h	**77 ± 5**
UU601-2	1200 °C 2h	**68 ± 6**
UU601-3	1500 °C 1h	**38 ± 1**
UU602-1	850 °C 4h	**285 ± 24**
UU602-2	1200 °C 1h	**72 ± 6**
UU602-2	1200 °C 2h	**70 ± 5**
UU602-3	1500 °C 1h	**38 ± 2**

Table 3.3: Narrowest recorded PLE line width $\mathbf{\Delta\nu}_{\min}$ in MHz for the investigated samples (utilized resonant excitation laser power of ≈ 1 nW without green repump in all cases, relative spectra are shown in appendix B) and lifetime-limited line width for GeV color centers [26].
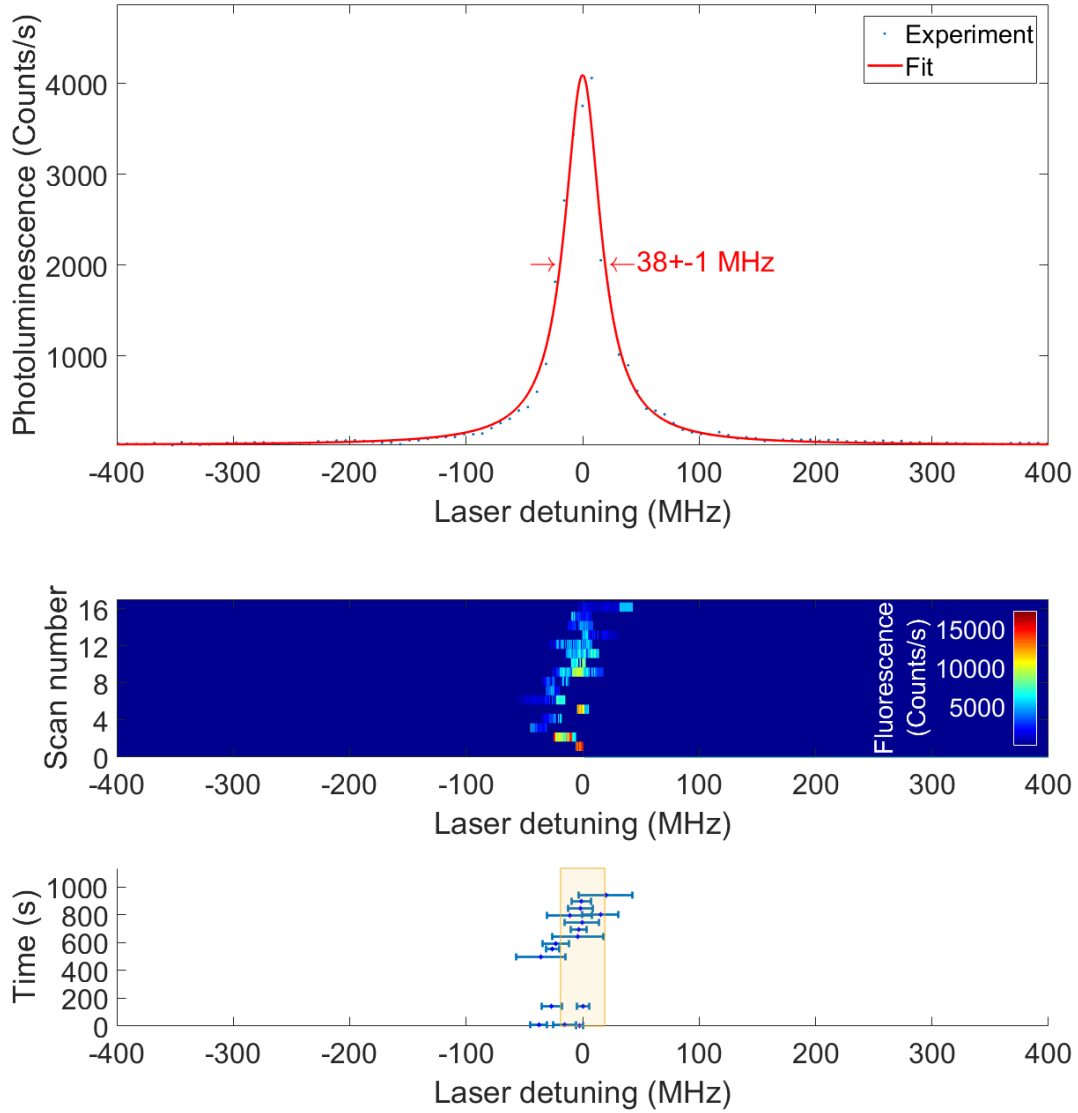
Figure 3.13: Top: Repetitive PLE measurements of transition C of a GeV center in sample UU601-3 (blue dotted line). In the low-intensity limit ($\approx$ 1 nW of resonant laser excitation only), a line width as narrow as 38 MHz was recorded (revealed by Lorentzian fit, red solid line).

Middle: The shown PLE spectrum is an aggregate of several scans (16).

Bottom: The GeV transition was stable in frequency for measurements of $\approx$ 15 minutes. An absolute drift of the transition frequency of less than its natural line width (orange shaded area) over such long periods highlights the quality of the investigated GeV emitter.
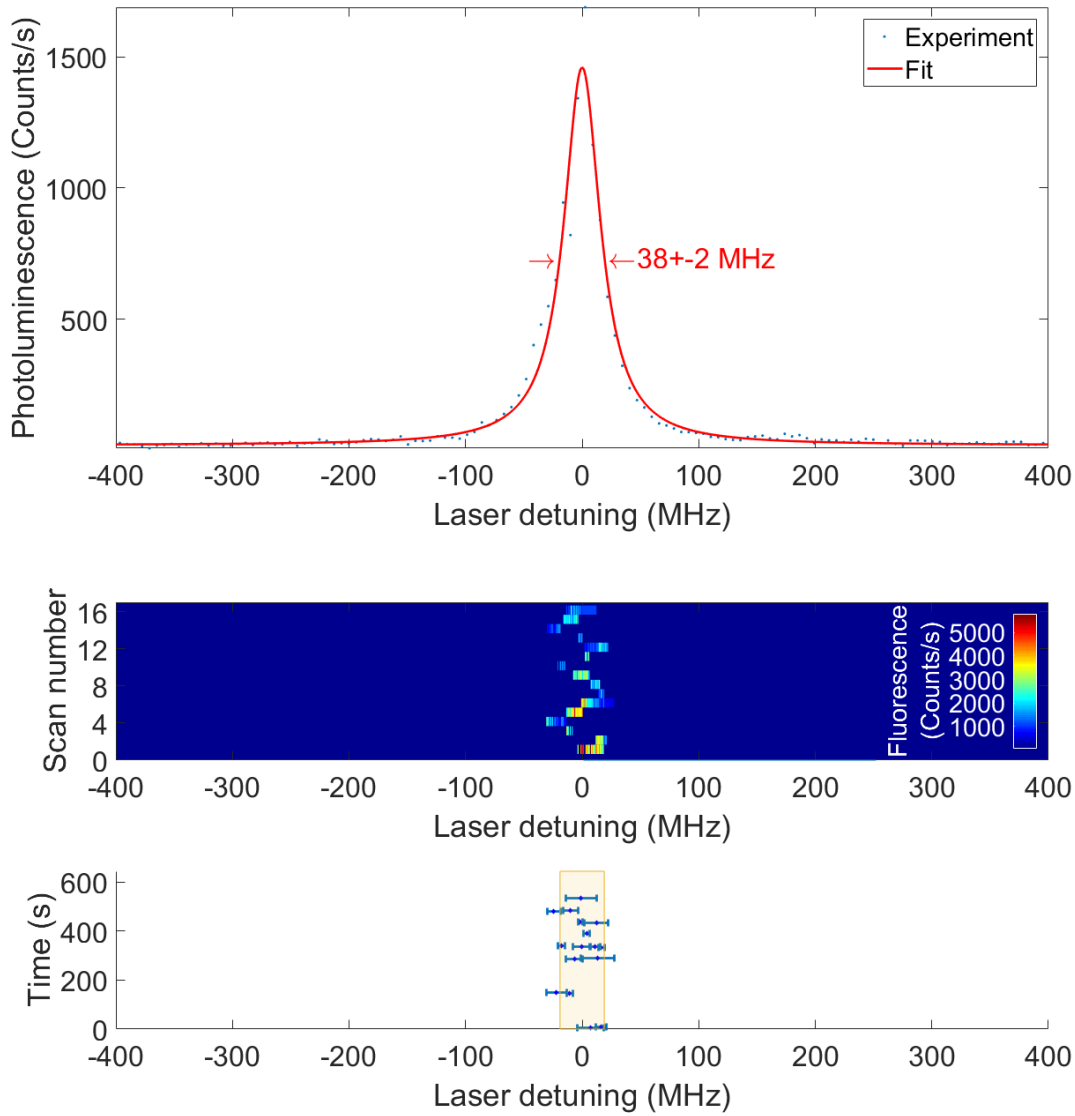
Figure 3.14: Top: Repetitive PLE measurements of transition C of a GeV center in sample UU602-3 (blue dotted line). In the low-intensity limit (≈ 1 nW of resonant laser excitation only), a line width as narrow as 38 MHz was recorded (revealed by Lorentzian fit, red solid line).

Middle: The shown PLE spectrum is an aggregate of several scans (16).

Bottom: The GeV transition was stable in frequency for measurements of ≈ 10 minutes. An absolute drift of the transition frequency of less than its natural line width (orange shaded area) over such long periods highlights the quality of the investigated GeV emitter.

From the results reported in table 3.3, it is clear that the narrowest PLE line widths $\boldsymbol{\Delta\nu}_{\mathrm{min}}$ of the probed GeV centers in each sample follow the same trend as the RT line widths of the GeV ZPLs $\boldsymbol{\Delta\lambda}$, discussed in section 3.1.1, and the average ground state splittings $\boldsymbol{\Delta}\mathrm{SO_g}$ of section 3.1.2. This clearly indicates the improvement in the local surroundings of the probed GeV centers for increasing annealing temperatures. This behaviour is explained by the fact that higher annealing temperatures result in lower residual implantation damage in the diamond samples, which is beneficial for the optical properties of the created defects. However, except for sample UU601-1, all the investigated diamond samples present GeV emitters that are spectrally stable even in absence of the off-resonant excitation. Moreover, it is possible to create several emitters with identical transition frequencies that can possibly be addressed several times and on-demand, as they are stable enough and do not bleach away when resonantly excited. The narrowest line widths observed for centers in samples annealed at 1500 °C are close to the lifetime-limited value of 26 MHz [26]. The difference can be attributed to remaining implantation damage that was not relieved during the annealing processes [65]. However, one can take into account the effect of residual laser power broadening of the line widths as well (or both). On the other hand, decreasing the laser excitation power (in the pW regime) would result in absence of response from the probed emitters, as the excitation power is too low to record any PLE signal. Nevertheless, together with the results obtained by RT and LT spectroscopy, the narrow PLE line widths are a sign of very low implantation damage remaining after the 1500 °C annealing treatment. Therefore, Germanium-Vacancy centers created in the samples annealed at high temperature show the best spectral stability and near lifetime-limited line widths, which makes them promising candidates for indistinguishable single-photon sources (section 1.3.4 and equation 1.12). Note that line widths of 38 MHz are even narrower than the line width of 42 MHz reported in [26] for in-grown GeV defects in diamond (figure 1.12).

The implantation depth of the Ge ions does not seem to play any significant role in determining the properties of the created GeV centers in all cases. The obtained $\boldsymbol{\Delta\nu}_{\mathrm{min}}$ are indeed practically the same for samples subject to analogous annealing treatments, irrespective of the depth of the implanted Ge ions.

3.3.   Excited state lifetime measurements

The excited state lifetime measurements were performed on the samples after completing all the annealing treatments, i.e., samples UU601-1 and UU602-1 were annealed for 4 hours in total, samples UU601-2 and UU602-2 were subject to 2 hours of treatment and samples UU601-3 and UU602-3 to 1 hour of treatment. The measurements were performed at the temperature of 4 K. The same regions of the samples were investigated as in the experiments discussed so far in sections 3.1.1, 3.1.2 and 3.2. The excitations were performed by 532 nm femtosecond laser pulses at powers of $\approx$ 300 μW.

For each of the six samples, 40 GeV emitters were probed and the resulting decay signals were fitted by a single exponential decay model in MATLAB. From the fits (see appendix C), the resulting excited state T_1 lifetimes were retrieved. Histograms for the lifetimes of the emitters are shown in figure 3.15. Subsequently, the predicted lifetime-limited line widths were estimated as $\Delta\nu = \frac{1}{2\pi T_1}$ (see section 1.2), see figure 3.16. The average values of lifetimes and estimated lifetime-limited line widths are summarized in table 3.4.

The values of average lifetimes obtained from all the samples are in agreement with the reported values of 1.4-5.5 ns [74]. The resulting average predicted lifetime-limited line widths are all broader than the intrinsic value of 26 MHz. Based on the results described above, this was expected as none of the investigated samples is strain-free. The average values of T_1 increase with annealing temperature and reach the maximum values of 5.3 ns and 5.4 ns for samples UU601-3 and UU602-3, respectively. Moreover, the corresponding expected average values of lifetime-limited line width $\Delta\nu$ are close to 30 MHz. The line widths of $\Delta\nu_{\min} = 38$ MHz measured by PLE investigations for both samples (section 3.2) are close to the $\Delta\nu$ values retrieved from the lifetime measurements. Moreover, the narrowest recorded line widths $\Delta\nu_{\min}$ are instead much broader than the estimated lifetime-limited values for all the other samples, which indicates high quality of GeV centers formed at 1500 °C. As the predicted average GeV line width decreases with increasing annealing temperature, these findings confirm and reinforce that higher annealing temperatures lead to better properties of the created emitters, as the diamond lattices benefit most from the high temperature annealing treatments.

It is important to point out that the obtained average lifetimes are independent of the implantation depth of the Ge ions for all samples. As already described for all the other relevant quantities discussed in the present work, the calculated average T_1 values are close to each other in samples subject to the same annealing treatments, regardless of the depth of the implanted Ge ions.
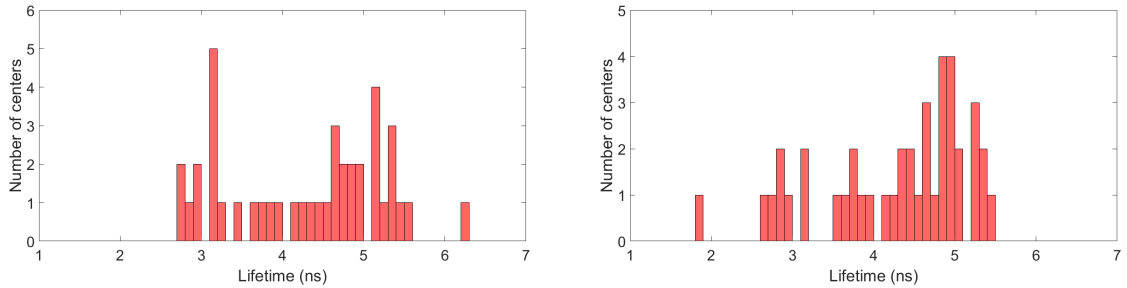
(a) Histograms of T_1 times for GeV emitters in samples (left) UU601-1 (4 h annealing) and (right) UU602-1 (4 h annealing).
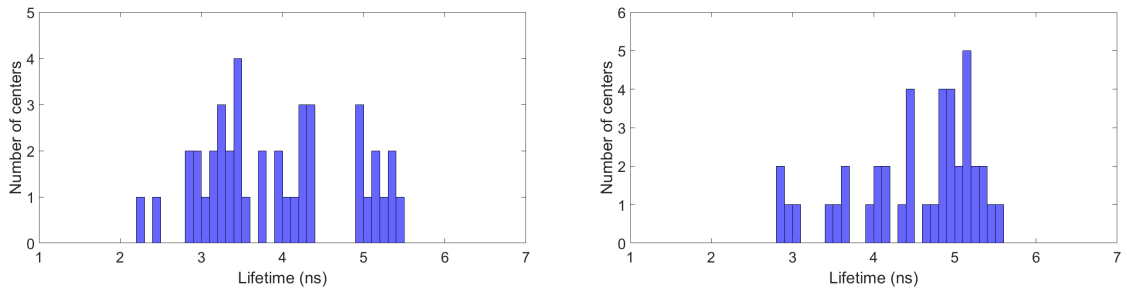
(b) Histograms of T_1 times for GeV emitters in samples (left) UU601-2 (2 h annealing) and (right) UU602-2 (2 h annealing).
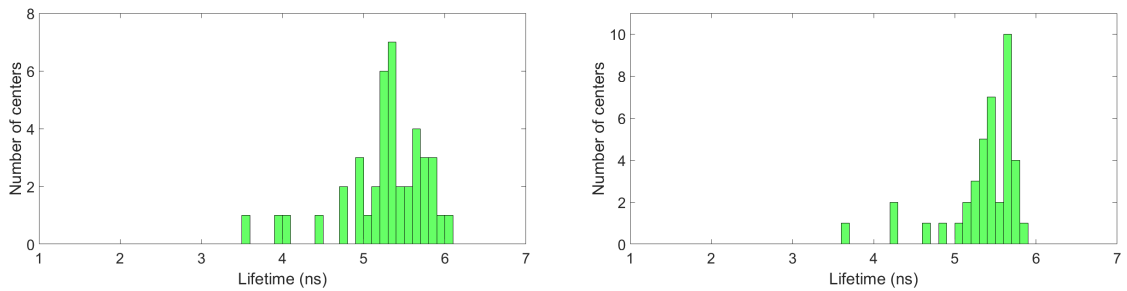
(c) Histograms of T_1 times for GeV emitters in samples (left) UU601-3 and (right) UU602-3.

Figure 3.15: Histograms of T_1 lifetimes for GeV emitters in (a) samples UU601-1 and UU602-1 (4 h annealing at 850 °C), (b) samples UU601-2 and UU602-2 (2 h annealing at 1200 °C) and (c) samples UU601-3 and UU602-3 (1 h annealing at 1500 °C). GeV centers measured in samples annealed at 1500 °C show narrower inhomogeneous distributions of the lifetimes.
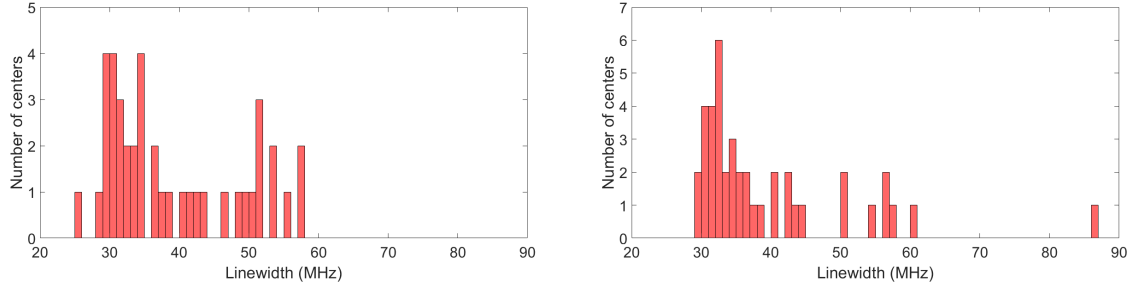
(a) Histograms of estimated lifetime-limited line widths $\mathbf{\Delta\nu}$ for GeV emitters in samples (left) UU601-1 (4 h annealing) and (right) UU602-1 (4 h annealing).
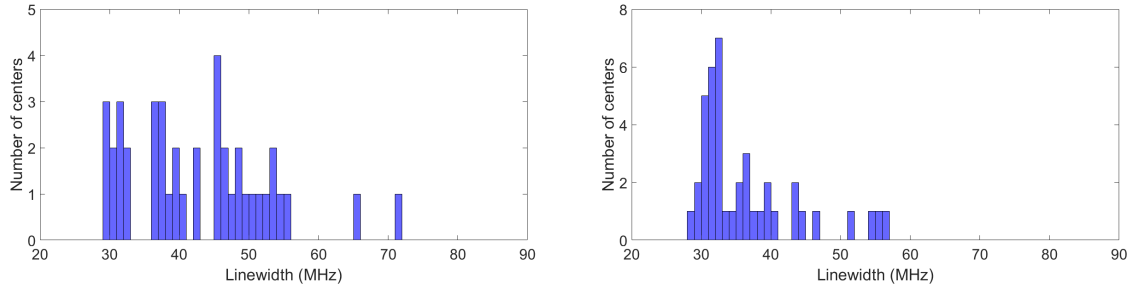
(b) Histograms of estimated lifetime-limited line widths $\mathbf{\Delta\nu}$ for GeV emitters in samples (left) UU601-2 (2 h annealing) and (right) UU602-2 (2 h annealing).
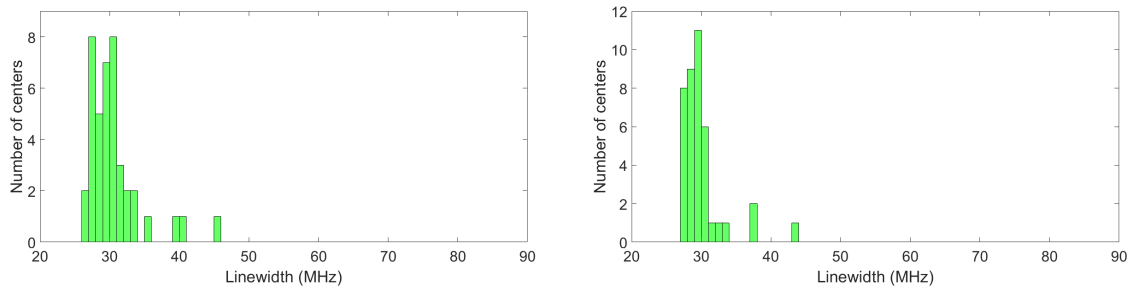
(c) Histograms of estimated lifetime-limited line widths $\mathbf{\Delta\nu}$ for GeV emitters in samples (left) UU601-3 and (right) UU602-3.

Figure 3.16: Histograms of estimated lifetime-limited line widths $\mathbf{\Delta\nu}$ for GeV emitters in (a) samples UU601-1 and UU602-1 (4 h annealing at 850 °C), (b) samples UU601-2 and UU602-2 (2 h annealing at 1200 °C) and (c) samples UU601-3 and UU602-3 (1 h annealing at 1500 °C). GeV centers measured in samples annealed at 1500 °C show narrower inhomogeneous distributions of the line widths.

Table 3.4

Sample	Treatment	Average Lifetime T_1 (ns)	Average Line width $\Delta\nu$ (MHz)
UU601-1	850 °C 4h	4.3 ± 0.9	39.0 ± 9.5
UU601-2	1200 °C 2h	3.9 ± 0.9	42.7 ± 10.0
UU601-3	1500 °C 1h	5.3 ± 0.5	30.5 ± 3.8
UU602-1	850 °C 4h	4.3 ± 0.9	39.5 ± 11.6
UU602-2	1200 °C 2h	4.5 ± 0.8	36.5 ± 7.5
UU602-3	1500 °C 1h	5.4 ± 0.5	30.0 ± 3.2

Table 3.4: Average T_1 lifetime in ns and estimated lifetime-limited line width $\Delta\nu$ in MHz for the six measured samples.

Combining the results of PLE and lifetime measurements, it is interesting to estimate the expected indistinguishability ξ of the created emitters within samples annealed at different temperatures. To that purpose, the average lifetime values calculated above as well as the narrowest recorded PLE line widths presented in section 3.2 can be inserted in equation 1.12, to give

$$\xi_{850\,°C} = (2\pi \; 4.3 \text{ ns } 285 \text{ MHz})^{-1} \approx 0.13, \tag{3.7}$$

$$\xi_{1200\,°C} = (2\pi \; 3.9 \text{ ns } 68 \text{ MHz})^{-1} \approx 0.60, \tag{3.8}$$

$$\xi_{1500\,°C} = (2\pi \; 5.3 \text{ ns } 38 \text{ MHz})^{-1} \approx 0.79. \tag{3.9}$$

The indistinguishability of the created GeV emitters increases with increasing annealing temperature of the diamonds. Clearly, the samples annealed at 850 °C show very poor degree of indistinguishability, whereas the value of ξ increases consistently for higher annealing temperatures. The Germanium-Vacancy centers formed in the samples annealed at 1500 °C show the highest expected indistinguishability, due to the near lifetime-limited PLE line widths. However, $\xi_{1500\,°C}$ is still significantly lower than 1, as the measured narrowest line widths are not lifetime-limited. The value of $\xi_{1500\,°C}$ would approach its

maximum fast for line widths even sightly narrower than the measured 38 MHz. Moreover, it is worth pointing out that the measured PLE line widths could still be affected by power broadening. Thus, it is in principle possible that the actual line widths are narrower than 38 MHz in the 1500 °C annealing case and, consequently, that the indistinguishability is higher than the estimated value of 79%. As an alternative, it would be possible to act on the lifetimes of the emitters: reducing the T_1 times would result in improved indistinguishability.

4 | Conclusions and future developments

In the context of this work, the impact of annealing on the optical properties of Germanium-Vacancy centers in diamonds is systematically studied. Six diamond samples implanted with ^{74}Ge ions at two different energies were subjected to various annealing treatments. The annealing process is expected to provide a recovery of the damage of diamond lattice that occurs during implantation. The optical properties of GeV centers were investigated by means of photoluminescence spectroscopy, Photoluminescence Excitation and lifetime measurements at room and cryogenic temperatures.

The obtained results show a strong dependence of formation and properties of GeV on the chosen annealing treatment. The room temperature PL spectroscopy reveals that short annealing time (1 hour) at 850 °C is insufficient for formation of GeV centers. Subsequent annealing at the same temperature results in the formation of color centers, evident by the characteristic PL spectra. However, the ZPLs of the investigated spectra are broad and accompanied by strong background. This indicates that annealing at 850 °C does not relieve the radiation damage produced upon the ion implantation. Improved results can be observed for higher annealing temperatures. By increasing the temperature, the relative amount of formed GeV centers as well as their brightness increase. This is accompanied by a gradual decrease in the ZPL line width and background signal. At the highest annealing temperature, i.e., 1500 °C, the PL spectra show the narrowest line widths and strong suppression of the background.

Cryogenic photoluminescence spetroscopy reveals information on the local surroundings of GeV centers, i.e, on the strain environment. For the samples annealed at lower temperatures, the recorded spectra show strong shifts in the positions of the C and D ZPL transitions, along with a large splitting between the spectral lines. These features are attributed to longitudinal and transversal strain, respectively. The situation improves with annealing at high temperature, i.e., the peaks group close to each other whereas the line splitting decreases. The extracted ground state splitting is decreasing with increasing

annealing temperature, thus indicating a reduction of strain. In the samples annealed at 1500 °C the ground state splitting approaches the reported value for non-strained GeV centers. This indicates that high annealing temperature is beneficial for producing unstrained color centers.

The Photoluminescense Excitation spectroscopy provides more information on the local environment and the quality of the produced color centers. Almost no stable resonant excitation can be detected within the samples annealed at 850 °C. The situation improves with increasing annealing temperature. Stable resonant excitation is observed in the samples annealed at both 1200 °C and 1500 °C. The line widths of the ZPL are decreasing with increasing annealing temperature. This is accompanied by a reduction in spectral diffusion. Notably, these measurements could be conducted without any optical off-resonant excitation in all cases. Moreover, near lifetime-limited line widths are observed for the centers created at 1500 °C. Narrow inhomogeneous distribution of transition frequencies is revealed in the samples annealed at high temperature.

The lifetime measurements support the spectroscopy results. The increase in the annealing temperature leads to an increase in radiative lifetime of the emitters and, consequently, narrower lifetime-limited line widths. Moreover, the distribution of the lifetimes becomes narrow for samples annealed at 1500 °C, indicating high degree of similarity between different color centers. The combination of the data acquired from PLE and lifetime measurements allows to estimate the degree of indistinguishability of the produced color centers.

No significant impact of the different implantation energies is observed. This indicates the robustness of the GeV with respect to location relative to the diamond surface.

The experimental findings demonstrate the reliable fabrication of high quality GeV centers via ion implantation and subsequent annealing treatment. The annealing temperature significantly influences the quality of the implanted GeV centers, with higher temperatures enhancing the quality of the emitters. The results suggest that even short annealing at high temperatures (1500 °C) yields low strained emitters with remarkable optical properties, such as spectral stability and near lifetime-limited line widths of the transitions, independent of the implantation energy. The results of this work are interesting with respect to the other group-IV centers in diamond. Compared to the reported annealing studies on SiV [49], formation of high quality GeV centers requires higher annealing temperatures. Taking this into account, one can expect that for heavier elements, such as Sn and Pb, even higher temperatures are required. Extending these studies to those elements might open the opportunity for reliable creation of the corresponding color centers.

Moreover, the properties of the implanted GeV emitters can be improved further. Thus, for future work, this study could be extended by performing the annealing in several steps. For instance, the diamond samples first undergo annealing at relatively low temperatures (e.g., 850 °C or 1200 °C), to be subsequently subjected to further annealing steps at higher temperature (e.g., 1500 °C). That might provide information on the impact of additional and intermediate annealing steps on the properties of the emitters. Another interesting route for future work could be the investigation of implantation of Ge ions at higher energies (in the MeV regime) into the diamond samples. In the present work, no difference in the properties of GeV centers implanted with different energies within ~ 100 nm inside the diamond surface was observed. However, deep implantation (in the μm depth range) might require different annealing treatments. Furthermore, the impact of the implantation dose could be another interesting and important parameter for future studies. Higher doses compared to the ones hereby investigated would lead to even higher damage of the lattice. This might require annealing at higher temperature or longer annealing time, in order to create high quality centers. In contrast, for lower doses the annealing conditions might be more gentle to produce color centers with good properties. Once the best possible procedure to produce high quality GeV centers is established, the following step would be to integrate these defects, via deterministic ion implantation, with nanophotonic devices, which can be used for different quantum applications.

Bibliography

[1] D. P. DiVincenzo, "Quantum computation.," *Science*, vol. 270, p. 255–261, 1995.

[2] E. Knill, R. Laflamme, and G. J. Milburn, "A scheme for efficient quantum computation with linear optics.," *Nature*, vol. 409, p. 46–52, 2001.

[3] L. Childress, J. M. Taylor, A. S. Sørensen, and M. D. Lukin, "Fault-tolerant quantum communication based on solid-state photon emitters.," *Physical Review Letters*, vol. 96, 2006.

[4] J. Wrachtrup and F. Jelezko, "Processing quantum information in diamond.," *Journal of Physics: Condensed Matter*, vol. 18, 2006.

[5] T. D. Ladd, F. Jelezko, R. Laflamme, Y. Nakamura, C. Monroe, and J. L. O'Brien, "Quantum computers.," *Nature*, vol. 464, p. 45–53, 2010.

[6] L. K. Grover, "A fast quantum mechanical algorithm for database search.," *In Proceedings of the Twenty-eighth Annual ACM Symposium on Theory of Computing*, vol. STOC '96, p. 212–219, 1996.

[7] P. Shor, "Polynomial-time algorithms for prime factorization and discrete logarithms on a quantum computer.," *SIAM Journal on Computing*, vol. 26, p. 1484–1509, 1997.

[8] E. Giese, A. Roura, G. Tackmann, E. M. Rasel, and W. P. Schleich, "Double Bragg diffraction: A tool for atom optics.," *Physical Review A*, vol. 88, 2013.

[9] H. Müntinga, H. Ahlers, M. Krutzik, A. Wenzlawski, S. Arnold, D. Becker, K. Bongs, H. Dittus, H. Duncker, N. Gaaloul, C. Gherasim, E. Giese, C. Grzeschik, T. W. Hänsch, O. Hellmig, W. Herr, S. Herrmann, E. Kajari, S. Kleinert, C. Lämmerzahl, W. Lewoczko-Adamczyk, J. Malcolm, N. Meyer, R. Nolte, A. Petersa, M. Popp, J. Reichel, A. Roura, J. Rudolph, M. Schiemangk, M. Schneider, S. T. Seidel, K. Sengstock, V. Tamma, T. Valenzuela, A. Vogel, R. Walser, T. Wendrich, P. Windpassinger, W. Zeller, T. van Zoest, W. Ertmer, W. P. Schleich, and E. M. Rasel, "Interferometry with Bose-Einstein condensates in microgravity.," *Physical Review Letters*, vol. 110, 2013.

[10] E. Giese, W. Zeller, S. Kleinert, M. Meister, V. Tamma, A. Roura, and W. P. Schleich, "The interface of gravity and quantum mechanics illuminated by Wigner phase space.," *Proceedings of the International School of Physics "Enrico Fermi", Course 188, "Atom Interferometry"*, vol. 171, 2014.

[11] R. P. Feynman, "Simulating physics with computers.," *International Journal of Theoretical Physics*, vol. 21, p. 467–488, 1982.

[12] S. Lloyd, "Universal quantum simulators.," *Science*, vol. 273, p. 1073–1078, 1996.

[13] J. I. Cirac and P. Zoller, "Goals and opportunities in quantum simulation.," *Nature Physics*, vol. 8, p. 264–266, 2012.

[14] C. H. Bennett and G. Brassard, "Quantum cryptography: Public key distribution and coin tossing.," *Proceedings of IEEE International Conference on Computers, Systems and Signal Processing*, p. 175–179, 1984.

[15] W. Pfaff, B. J. Hensen, H. Bernien, S. B. van Dam, M. S. Blok, T. H. Taminiau, M. J. Tiggelman, R. N. Schouten, M. Markham, D. J. Twitchen, and R. Hanson, "Unconditional quantum teleportation between distant solid-state quantum bits.," *Science*, vol. 345, p. 532–535, 2014.

[16] G. Balasubramanian, I. Y. Chan, R. Kolesov, M. Al-Hmoud, J. Tisler, C. Shin, C. Kim, A. Wojcik, P. R. Hemmer, A. Krueger, T. Hanke, A. Leitenstorfer, R. Bratschitsch, F. Jelezko, and J. Wrachtrup, "Nanoscale imaging magnetometry with diamond spins under ambient conditions.," *Nature*, vol. 455, p. 648–651, 2008.

[17] P. Maletinsky, S. Hong, M. S. Grinolds, B. Hausmann, M. D. Lukin, R. L. Walsworth, M. Loncar, and A. Yacoby, "A robust scanning diamond sensor for nanoscale imaging with single nitrogen-vacancy centres.," *Nature Nanotechnology*, vol. 7, p. 320–324, 2012.

[18] A. Ermakova, G. Pramanik, J. M. Cai, G. Algara-Siller, U. Kaiser, T. Weil, Y. K. Tzeng, H. C. Chang, L. P. McGuinness, M. B. Plenio, B. Naydenov, and F. Jelezko, "Detection of a few metallo-protein molecules using color centers in nanodiamonds.," *Nano Letters*, vol. 13, p. 3305–3309, 2013.

[19] C. Müller, X. Kong, J. M. Cai, K. Melentijević, A. Stacey, M. Markham, D. Twitchen, J. Isoya, S. Pezzagna, J. Meijer, J. F. Du, M. B. Plenio, B. Naydenov, L. P. McGuinness, and F. Jelezko, "Nuclear magnetic resonance spectroscopy with single spin sensitivity.," *Nature Communications*, vol. 5, 2014.

[20] Y. Romach, C. Müller, T. Unden, L. J. Rogers, T. Isoda, K. M. Itoh, M. Markham,

A. Stacey, J. Meijer, S. Pezzagna, B. Naydenov, L. P. McGuinness, N. Bar-Gill, and F. Jelezko, "Spectroscopy of surface-induced noise using shallow spins in diamond.," *Physical Review Letters*, vol. 114, 2015.

[21] H. J. Kimble, "The quantum internet.," *Nature*, vol. 453, p. 1023–1030, 2008.

[22] Z. S. Yuan, Y. A. Chen, B. Zhao, S. Chen, J. Schmiedmayer, and J. W. Pan, "Experimental demonstration of a BDCZ quantum repeater node.," *Nature*, vol. 454, p. 1098–1101, 2008.

[23] P. Neumann, R. Kolesov, B. Naydenov, J. Beck, F. Rempp, M. Steiner, V. Jacques, G. Balasubramanian, M. L. Markham, D. J. Twitchen, S. Pezzagna, J. Meijer, J. Twamley, F. Jelezko, and J. Wrachtrup, "Quantum register based on coupled electron spins in a room temperature solid.," *Nature Physics*, vol. 6, p. 249–253, 2010.

[24] E. Togan, Y. Chu, A. S. Trifonov, L. Jiang, J. Maze, L. Childress, M. V. G. Dutt, A. S. Sørensen, P. R. Hemmer, A. S. Zibrov, and M. D. Lukin, "Quantum entanglement between an optical photon and a solid-state spin qubit.," *Nature*, vol. 466, p. 730–734, 2010.

[25] L. Childress, R. Walsworth, and M. Lukin, "From quantum computers to biological sensors.," *Physics Today*, vol. 67, p. 38–43, 2014.

[26] P. Siyushev, M. H. Metsch, A. Ijaz, J. M. Binder, M. K. Bhaskar, D. D. Sukachev, A. Sipahigil, R. E. Evans, C. T. Nguyen, M. D. Lukin, P. R. Hemmer, Y. N. Palyanov, I. N. Kupriyanov, Y. M. Borzdov, L. J. Rogers, and F. Jelezko, "Optical and microwave control of germanium-vacancy center spins in diamond.," *Phys. Rev. B*, vol. 96, 2017.

[27] C. Kittel, *Introduction to Solid State Physics*. Oldenbourg, 2006.

[28] A. M. Zaitsev, *Optical Properties of Diamond: A Data Handbook*. Springer, 2001.

[29] T. Ruf, M. Cardona, C. S. J. Pickles, and R. Sussmann, "Temperature dependence of the refractive index of diamond up to 925 K.," *Phys. Rev. B*, vol. 62, 2000.

[30] R. Robertson, J. J. Fox, and A. E. Martin, "Two types of diamond," *Philosophical Transactions of the Royal Society of London. Series A, Containing Papers of a Mathematical or Physical Character*, vol. 232, p. 463–535, 1934.

[31] H. B. Dyer, F. A. Raal, L. D. Preez, and J. H. N. Loubser, "Optical absorption features associated with paramagnetic nitrogen in diamond.," *The Philosophical Maga-*

zine: A Journal of Theoretical Experimental and Applied Physics, vol. 11, p. 763–774, 1965.

[32] R. Berman, P. R. W. Hudson, and M. Martinez, "Nitrogen in diamond: evidence from thermal conductivity.," *Journal of Physics C: Solid State Physics*, vol. 8, 1975.

[33] R. P. Mildren and J. R. Rabeau, *Optical Engineering of Diamond.* Wiley-VCH, 2013.

[34] R. S. Balmer, J. R. Brandon, S. L. Clewes, H. K. Dhillon, J. M. Dodson, I. Friel, P. N. Inglis, T. D. Madgwick, M. L. Markham, T. P. Mollart, N. Perkins, G. A. Scarsbrook, D. J. Twitchen, A. J. Whitehead, J. J. Wilman, and S. M. Woollard, "Chemical vapour deposition synthetic diamond: materials, technology and applications.," *Journal of Physics: Condensed Matter*, vol. 21, 2009.

[35] A. J. Neves and M. H. Nazare, *Properties, growth and applications of diamond.* INSPEC, 2001.

[36] F. P. Bundy, H. T. Hall, H. M. Strong, and R. H. Wentorf, "Man-made diamonds.," *Nature*, vol. 176, pp. 51–55, 1955.

[37] H. T. Hall, "Some high pressure, high temperature apparatus design considerations: Equipment for use at 100 000 atmospheres and 3000 °C.," *Review of Scientific Instruments*, vol. 29, p. 267–275, 1958.

[38] N. Pal'yanov, A. Sokol, M. Borzdov, and A. Khokhryakov, "Fluid-bearing alkaline carbonate melts as the medium for the formation of diamonds in the Earth's mantle: an experimental study.," *Lithos: Mineral Equilibria in Mantle Derived Rocks*, vol. 60, p. 145–159, 2002.

[39] R. Burns, J. Hansen, R. Spits, M. Sibanda, C. Welbourn, and D. Welch, "Growth of high purity large synthetic diamond crystals.," *Diamond and Related Materials*, vol. 8, p. 1433–1437, 1999.

[40] H. Sumiya, N. Toda, and S. Satoh, "Growth rate of high-quality large diamond crystals.," *Journal of Crystal Growth*, vol. 237-239, p. 1281–1285, 2002.

[41] C. B. Dischler, *Low-Pressure Synthetic Diamond Manufacturing and Applications.* Springer Verlag, 1998.

[42] J. Herlinger, "sp3's experience using hot filament CVD reactors to grow diamond for an expanding set of applications.," *Thin Solid Films*, vol. 501, p. 65–69, 2006.

[43] E. A. B. J. Luque, W. Juchmann, and J. B. Jeffries, "Excited state density distributions of H, C, C_2, and CH by spatially resolved optical emission in a diamond

depositing dc-arc jet reactor.," *Journal of Vacuum Science & Technology A: Vacuum, Surfaces, and Films*, vol. 16, p. 397, 1998.

[44] M. Schreck, S. Gsell, R. Brescia, and M. Fischer, "Ion bombardment induced buried lateral growth: the key mechanism for the synthesis of single crystal diamond wafers.," *Scientific Reports*, vol. 7, 2017.

[45] Y. N. Palyanov, I. N. Kupriyanov, Y. M. Borzdov, and N. V. Surovtsev, "Germanium: a new catalyst for diamond synthesis and a new optically active impurity in diamond.," *Scientific Reports*, vol. 5, 2015.

[46] C. Bradac, W. Gao, J. Forneris, M. E. Trusheim, and I. Aharonovich, "Quantum nanophotonics with group IV defects in diamond.," *Nature Communications*, vol. 10, 2019.

[47] J. Lang, *Creation of Color Centers in Diamond by Focused Ion Implantation.* Diplomarbeit University Ulm, 2016.

[48] J. R. Rabeau, P. Reichart, G. Tamanyan, D. N. Jamieson, S. Prawer, F. Jelezko, T. Gaebel, I. Popa, M. Domhan, and J. Wrachtrup, "Implantation of labelled single nitrogen vacancy centers in diamond using ^{15}N.," *Applied Physics Letters*, vol. 88, 2006.

[49] J. Lang, , S. Häußler, J. Fuhrmann, R. Waltrich, S. Laddha, J. Scharpf, A. Kubanek, B. Naydenov, and F. Jelezko, "Long optical coherence times of shallow-implanted, negatively charged silicon vacancy centers in diamond.," *Appl. Phys. Lett.*, vol. 116, 2020.

[50] C. D. Clark and C. B. Dickerson, "The 1.681 eV centre in polycrystalline diamond.," *Surface and Coatings Technology*, vol. 47, pp. 336–343, 1991.

[51] T. Basché, W. E. Moerner, M. Orrit, and U. P. Wild, *Single-Molecule Optical Detection, Imaging and Spectroscopy.* Wiley, 2008.

[52] W. E. Moerner and L. Kador, "Optical detection and spectroscopy of single molecules in a solid.," *Phys. Rev. Lett.*, vol. 62, pp. 2535–2538, 1989.

[53] A. Gruber, A. Dräbenstedt, C. Tietz, L. Fleury, J. Wrachtrup, and C. V. Borczyskowski, "Scanning confocal optical microscopy and magnetic resonance on single defect centers.," *Science*, vol. 276, pp. 2012–2014, 1997.

[54] A. Hughes, "Zero-phonon transitions and vibrational structure.," *Journal de Physique Colloques*, vol. 28 (C4), pp. C4–55–C4–65, 1967.

[55] J. J. Friedrich and D. Haarer, "Photochemical hole burning: A spectroscopic study of relaxation processes in polymers and glasses.," *Angewandte Chemie International Edition in English*, vol. 23, pp. 113–140, 1984.

[56] O. Sild and K. Haller, *Zero-phonon lines and spectral hole burning in spectroscopy and photochemistry.* Berlin: Springer-Verlag., 1988.

[57] H. Q. Zhao, M. Fujiwara, and S. Takeuchi, "Suppression of fluorescence phonon sideband from nitrogen vacancy centers in diamond nanocrystals by substrate effect.," *Opt. Express*, vol. 20, p. 15628–15635, 2012.

[58] A. M. White, "Applications of Photoluminescence Excitation spectroscopy to the study of indium gallium phosphide alloys.," *J. Phys. D: Appl. Phys.*, vol. 3, p. 1322–1328, 1970.

[59] J. Lee, V. Leong, D. Kalashnikov, J. Dai, A. Gandhi, and L. A. Krivitsky, "Integrated single photon emitters.," *AVS Quantum Sci.*, vol. 2, 2020.

[60] C. Hepp, T. Müller, V. Waselowski, J. N. Becker, B. Pingault, H. Sternschulte, D. Steinmüller-Nethl, A. Gali, J. R. Maze, M. Atatüre, and C. Becher, "Electronic structure of the silicon vacancy color center in diamond.," *Phys. Rev. Lett.*, vol. 112, 2014.

[61] L. J. Rogers, K. D. Jahnke, M. W. Doherty, A. Dietrich, L. P. McGuinness, C. Müller, T. Teraji, H. Sumiya, J. Isoya, N. B. Manson, and F. Jelezko, "Electronic structure of the negatively charged silicon-vacancy center in diamond.," *Phys. Rev. B*, vol. 89, 2014.

[62] M. Ruf, N. H. Wan, H. Choi, D. Englund, and R. Hanson, "Quantum networks based on color centers in diamond.," *Journal of Applied Physics*, vol. 130, 2021.

[63] A. Dietrich, K. D. Jahnke, J. M. Binder, T. Teraji, J. Isoya, L. J. Rogers, and F. Jelezko, "Isotopically varying spectral features of silicon-vacancy in diamond.," *New Journal of Physics*, vol. 16, 2014.

[64] A. Gali and J. R. Maze, "Ab initio study of the split silicon-vacancy defect in diamond: Electronic structure and related properties.," *Phys. Rev. B*, vol. 88, 2013.

[65] T. Iwasaki, Y. Miyamoto, T. Taniguchi, P. Siyushev, M. H. Metsch, F. Jelezko, and M. Hatano, "Tin-vacancy quantum emitters in diamond.," *Phys. Rev. Lett.*, vol. 119, 2017.

[66] S. D. Tchernij, A. Damin, M. Signorile, E. Moreva, P. Olivero, and J. Forneris,

"Single-photon emitters in lead-implanted single-crystal diamond.," *ACS Photonics*, vol. 5, pp. 4864–4871, 2018.

[67] J. P. Goss, R. Jones, S. J. Breuer, P. R. Briddon, and S. Öberg, "The twelve-line 1.682 eV luminescence center in diamond and the vacancy-silicon complex.," *Physical Review Letters*, vol. 77, pp. 3041–3044, 1996.

[68] M. Tinkham, *Group Theory and Quantum Mechanics.* Dover Publications, Inc., Mineola, New York, 1 edition., 2004.

[69] G. Watkins, "Defects in irradiated silicon: EPR of the tin-vacancy pair.," *Physical Review B*, vol. 12, pp. 4383–4390, 1975.

[70] G. F. Koster, J. O. Dimmock, R. G. Wheeler, and H. Statz, *The Properties of the Thirty-Two Point Groups.* M.I.T. Press, Cambridge, Massachusetts, 3 edition., 1963.

[71] K. D. Jahnke, *Low temperature spectroscopy of single colour centres in diamond.* PhD thesis, Universität Ulm, 2015.

[72] M. H. Metsch, *Group-IV Defects as Candidates for Light-Matter Interface in Quantum Communication.* PhD thesis, Universität Ulm, 2021.

[73] P. Wang, T. Taniguchi, Y. Miyamoto, M. Hatano, and T. Iwasaki, "Low-temperature spectroscopic investigation of lead-vacancy centers in diamond fabricated by high-pressure and high-temperature treatment.," *ACS Photonics*, vol. 8, pp. 2947–2954, 2021.

[74] T. Iwasaki, F. Ishibashi, Y. Miyamoto, Y. Doi, S. Kobayashi, T. Miyazaki, K. Tahara, K. D. Jahnke, L. J. Rogers, B. Naydenov, F. Jelezko, S. Yamasaki, S. Nagamachi, T. Inubushi, N. Mizuochi, and M. Hatano, "Germanium-vacancy single color centers in diamond.," *Scientific Reports*, vol. 5, 2015.

[75] M. K. Bhaskar, D. D. Sukachev, A. Sipahigil, R. E. Evans, M. J. Burek, C. T. Nguyen, L. J. Rogers, P. Siyushev, M. H. Metsch, H. Park, F. Jelezko, M. Lončar, and M. D. Lukin, "Quantum nonlinear optics with a germanium-vacancy color center in a nanoscale diamond waveguide.," *Phys. Rev. Lett.*, vol. 118, 2017.

[76] S. I. Azzam, K. Parto, and G. Moody, "Prospects and challenges of quantum emitters in 2D materials.," *Appl. Phys. Lett.*, vol. 118, 2021.

[77] L. J. Rogers, K. D. Jahnke, T. Teraji, L. Marseglia, C. Müller, B. Naydenov, H. Schauffert, C. Kranz, J. Isoya, L. P. McGuinness, and F. Jelezko, "Multiple intrin-

sically identical single-photon emitters in the solid state.," *Nature Communications*, vol. 5, 2014.

[78] I. B. W. Harris, C. P. Michaels, K. C. Chen, R. A. Parker, M. Titze, J. A. Martinez, M. Sutula, I. R. Christen, A. M. Stramma, W. Roth, C. M. Purser, M. H. Appel, C. Li, M. E. Trusheim, N. L. Palmer, M. L. Markham, E. S. Bielejec, M. Atatüre, and D. Englund, "Hyperfine spectroscopy of isotopically engineered group-IV color centers in diamond.," *arXiv - PHYS - Quantum Physics*, 2023.

[79] F. G. Kondev, M. Wang, W. J. Huang, S. Naimi, and G. Audi, "The nubase2020 evaluation of nuclear physics properties*.," *Chinese Phys. C*, vol. 45, 2021.

[80] A. Sipahigil, K. D. Jahnke, L. J. Rogers, T. Teraji, J. Isoya, A. S. Zibrov, F. Jelezko, and M. D. Lukin, "Indistinguishable photons from separated silicon-vacancy centers in diamond.," *Phys. Rev. Lett.*, vol. 113, 2014.

[81] L. J. Rogers, K. D. Jahnke, M. H. Metsch, A. Sipahigil, J. M. Binder, T. Teraji, H. Sumiya, J. Isoya, M. D. Lukin, P. Hemmer, and F. Jelezko, "All-optical initialization, readout, and coherent preparation of single silicon-vacancy spins in diamond.," *Phys. Rev. Lett.*, vol. 113, 2014.

[82] J. F. Ziegler, J. P. Biersack, and U. Littmark, *The Stopping and Range of Ions in Matter.* New York: Pergamon Press., 1985.

[83] K. J. Brown, E. Chartier, E. M. Sweet, D. A. Hopper, and L. C. Bassett, "Cleaning diamond surfaces using boiling acid treatment in a standard laboratory chemical hood.," *J. Chem. Health Saf.*, vol. 26, p. 40–44, 2019.

[84] C. Wang, C. Kurtsiefer, H. Weinfurter, and B. Burchard, "Single photon emission from SiV centres in diamond produced by ion implantation.," *Journal of Physics B Atomic Molecular and Optical Physics*, vol. 39, 2005.

[85] R. Cole, T. Jinadasa, and C. M. Brown, "Measuring and interpreting point spread functions to determine confocal microscope resolution and ensure quality control.," *Nature Protocols*, vol. 6, pp. 1929–1941, 2011.

[86] J. M. Binder, A. Stark, N. Tomek, J. Scheuer, F. Frank, K. D. Jahnke, C. Müller, S. Schmitt, M. H. Metsch, T. Unden, T. Gehring, A. Huck, U. L. Andersen, L. J. Rogers, and F. Jelezko, "Qudi: A modular python suite for experiment control and data processing.," *SoftwareX*, vol. 6, pp. 85–90, 2017.

[87] The MathWorks Inc., *MATLAB version: 9.3 (R2017b).* The MathWorks Inc., Natick, Massachusetts, United States, 2017.

[88] T. Ida, M. Ando, and H. Toraya, "Extended pseudo-Voigt function for approximating the Voigt profile.," *J. Appl. Cryst.*, vol. 33, pp. 1311–1316, 2000.

[89] S. Häußler, G. Thiering, A. Dietrich, N. Waasem, T. Teraji, J. Isoya, T. Iwasaki, M. Hatano, F. Jelezko, and A. Gali, "Photoluminescence excitation spectroscopy of SiV⁻ and GeV⁻ color center in diamond.," *New Journal of Physics*, vol. 19, 2017.

[90] S. A. Grudinkin, N. A. Feoktistov, K. V. Bogdanov, M. A. Baranov, V. G. Golubev, and A. V. Baranov, "Effect of reactive ion etching on the luminescence of GeV color centers in CVD diamond nanocrystals.," *Nanomaterials*, vol. 11, 2021.

[91] D. Chen, J. E. Fröch, S. Ru, H. Cai, N. Wang, G. Adamo, J. Scott, F. Li, N. Zheludev, I. Aharonovich, and W. Gao, "Quantum interference of resonance fluorescence from Germanium-Vacancy color centers in diamond.," *Nano Lett.*, vol. 22, p. 6306–6312, 2022.

[92] J. Geng, T. Shalomayeva, M. Gryzlova, A. Mukherjee, S. Santonocito, D. Dzhavadzade, D. Dasari, H. Kato, R. Stöhr, A. Denisenko, N. Mizuochi, and J. Wrachtrup, "Dopant-assisted stabilization of negatively charged single nitrogen-vacancy centers in phosphorus-doped diamond at low temperatures.," *arXiv:2305.15160*, 2023.

[93] L. Robledo, H. Bernien, I. van Weperen, and R. Hanson, "Control and coherence of the optical transition of single nitrogen vacancy centers in diamond.," *Phys. Rev. Lett.*, vol. 105, 2010.

A | Annealing temperature profiles
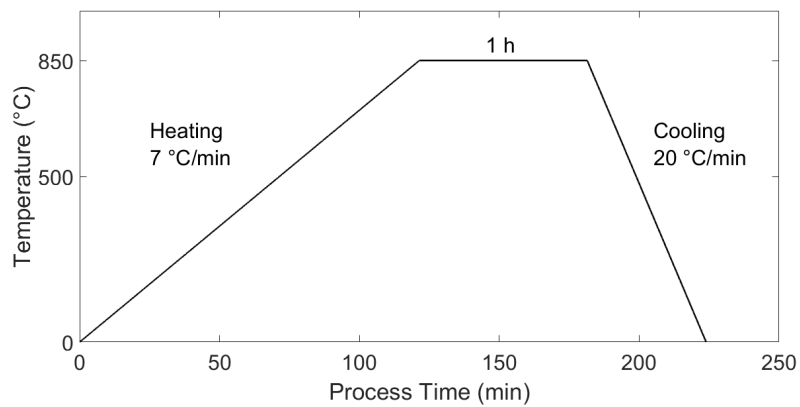
Figure A.1: Temperature profile of the GeV first high-vacuum annealing process, starting from room temperature, for samples UU601-1 and UU602-1. The time duration for which the temperature of 850 °C is hold is 1 hour.
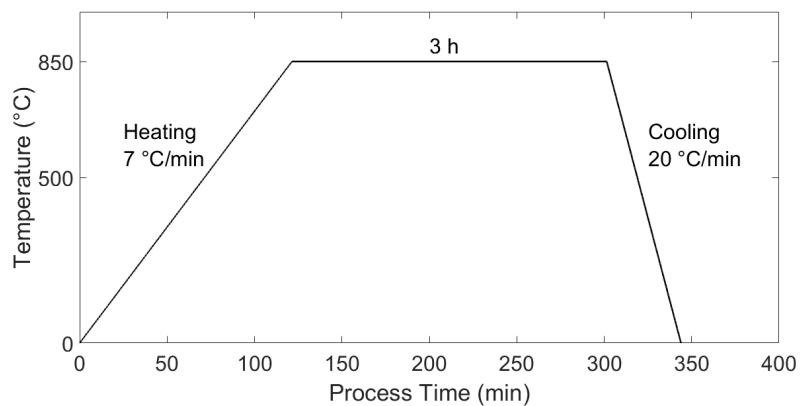
Figure A.2: Temperature profile of the GeV second high-vacuum annealing process, starting from room temperature, for samples UU601-1 and UU602-1. The time duration for which the temperature of 850 °C is hold is 3 hours.
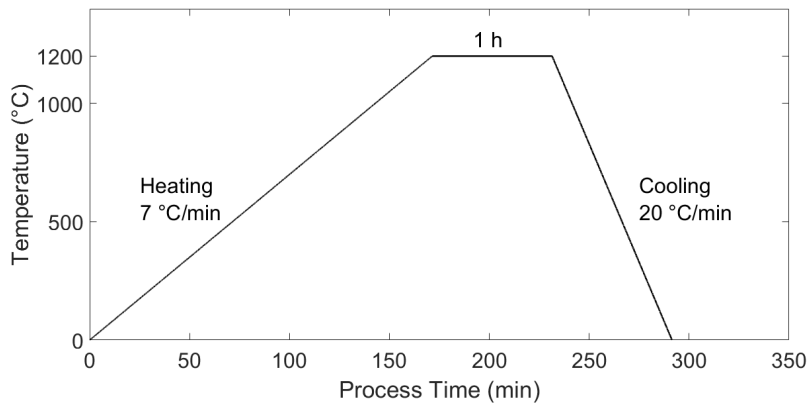
Figure A.3: Temperature profile of the GeV first and second high-vacuum annealing processes, starting from room temperature, for samples UU601-2 and UU602-2. The time duration for which the temperature of 1200 °C is hold is 1 hour.
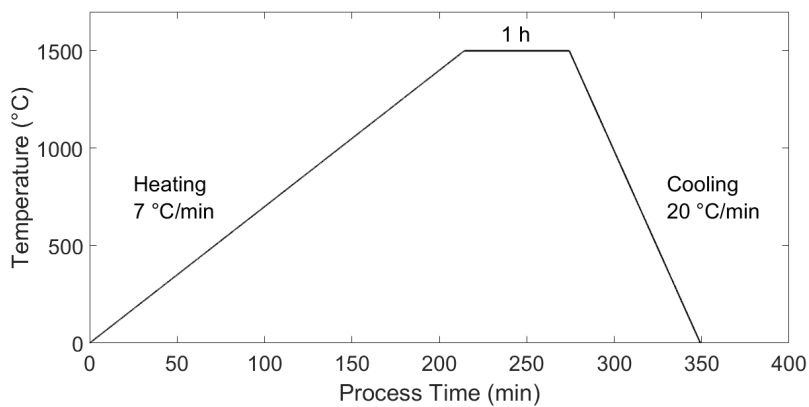
Figure A.4: Temperature profile of the GeV high-vacuum annealing process, starting from room temperature, for samples UU601-3 and UU602-3. The time duration for which the temperature of 1500 °C is hold is 1 hour.

B | PLE spectra
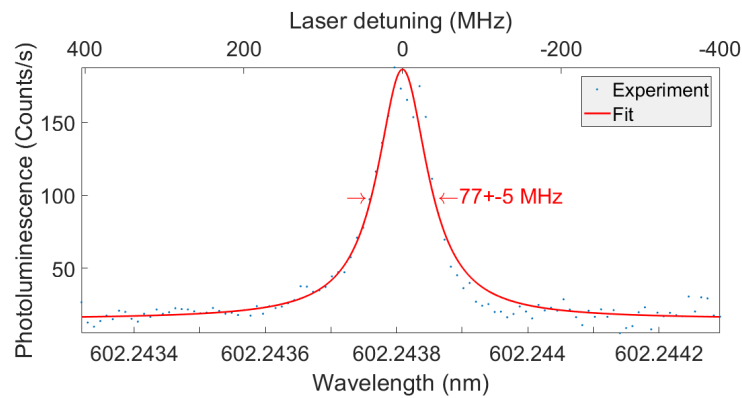
Figure B.1: Narrowest PLE spectrum of transition C of a GeV center within sample UU601-2 (1 h annealing at 1200 °C, blue dotted line). In the low-intensity limit (i.e., $\approx$ 1 nW of resonant laser excitation only), a line width as narrow as 77 MHz was recorded (revealed by Lorentzian fit, red solid line).
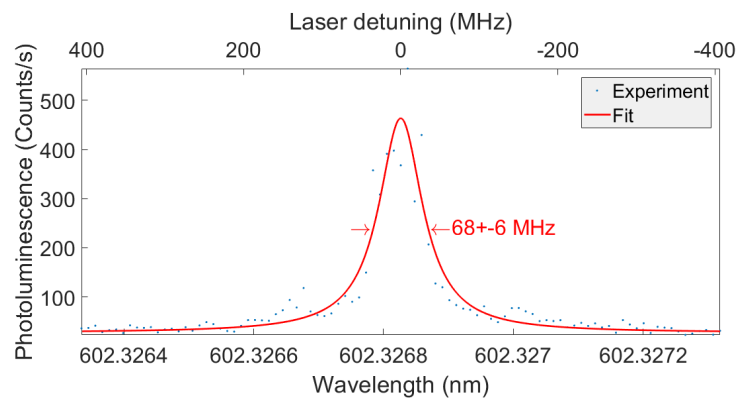
Figure B.2: Narrowest PLE spectrum of transition C of a GeV center within sample UU601-2 (2 h annealing at 1200 °C, blue dotted line). In the low-intensity limit (i.e., $\approx$ 1 nW of resonant laser excitation only), a line width as narrow as 68 MHz was recorded (revealed by Lorentzian fit, red solid line).
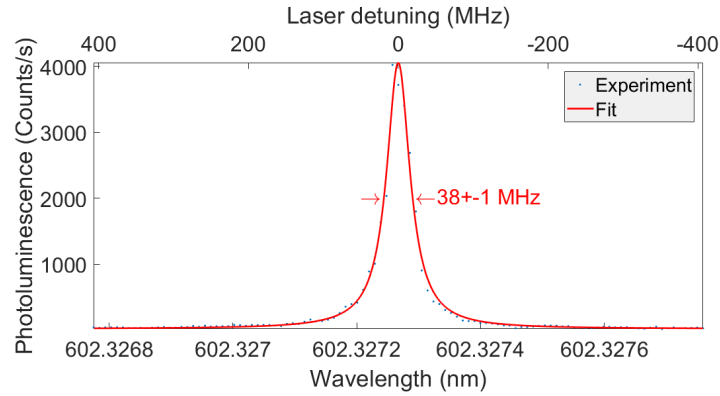
Figure B.3: Narrowest PLE spectrum of transition C of a GeV center within sample UU601-3 (1 h annealing at 1500 °C, blue dotted line). In the low-intensity limit (i.e., $\approx$ 1 nW of resonant laser excitation only), a line width as narrow as 38 MHz was recorded (revealed by Lorentzian fit, red solid line). The same PLE spectrum is shown in figure 3.13.
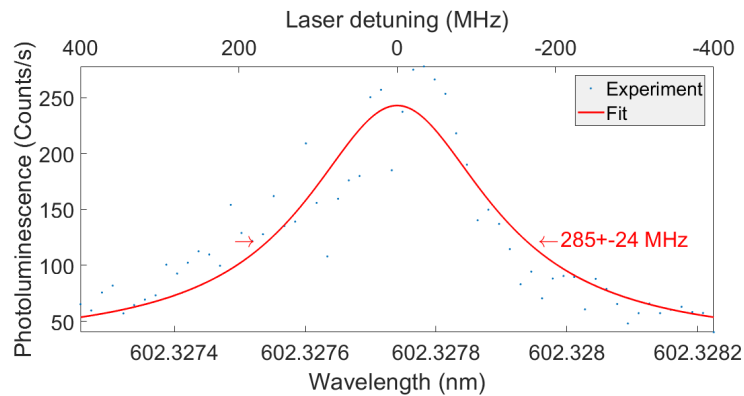
Figure B.4: Narrowest PLE spectrum of transition C of a GeV center within sample UU602-1 (4 h annealing at 850 °C, blue dotted line). In the low-intensity limit (i.e., $\approx$ 1 nW of resonant laser excitation only), a line width as narrow as 285 MHz was recorded (revealed by Lorentzian fit, red solid line).
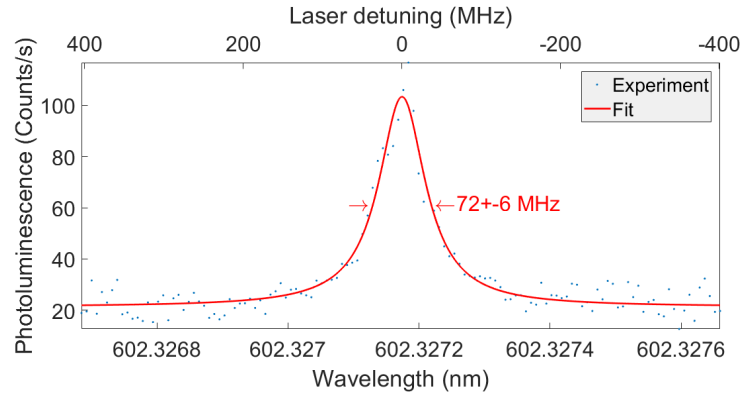
Figure B.5: Narrowest PLE spectrum of transition C of a GeV center within sample UU602-2 (1 h annealing at 1200 °C, blue dotted line). In the low-intensity limit (i.e., ≈ 1 nW of resonant laser excitation only), a line width as narrow as 72 MHz was recorded (revealed by Lorentzian fit, red solid line).
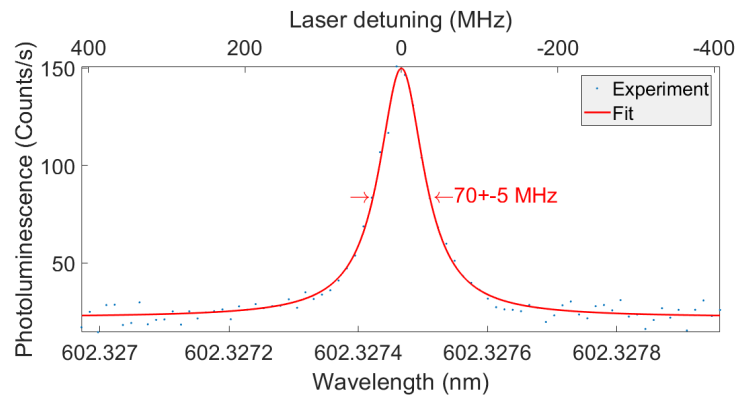
Figure B.6: Narrowest PLE spectrum of transition C of a GeV center within sample UU602-2 (2 h annealing at 1200 °C, blue dotted line). In the low-intensity limit (i.e., ≈ 1 nW of resonant laser excitation only), a line width as narrow as 70 MHz was recorded (revealed by Lorentzian fit, red solid line).
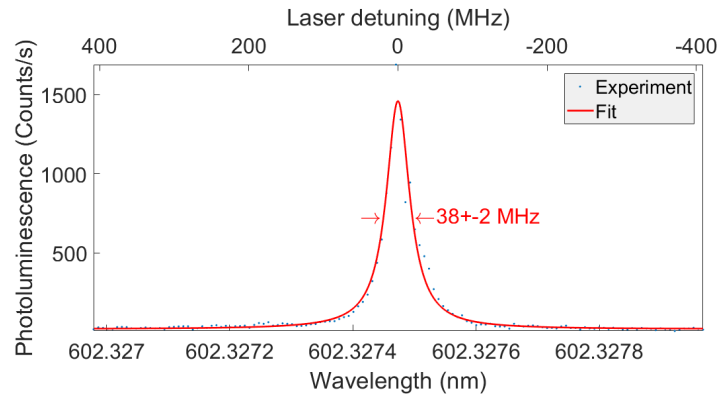
Figure B.7: Narrowest PLE spectrum of transition C of a GeV center within sample UU602-3 (1 h annealing at 1500 °C, blue dotted line). In the low-intensity limit (i.e., ≈ 1 nW of resonant laser excitation only), a line width as narrow as 38 MHz was recorded (revealed by Lorentzian fit, red solid line). The same PLE spectrum is shown in figure 3.14.

C | Lifetime measurements
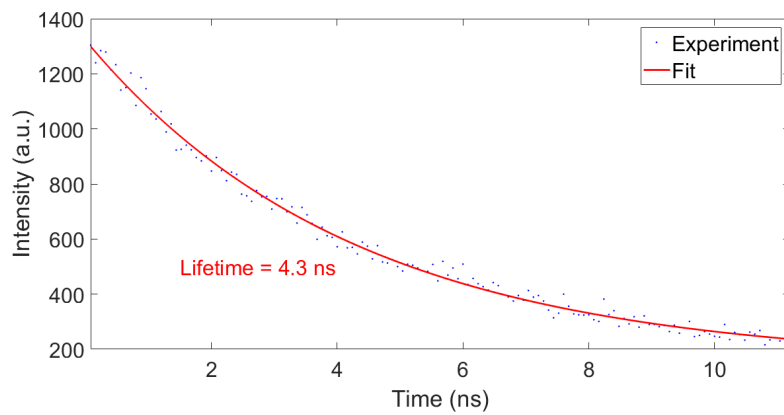
Figure C.1: Lifetime data for one exemplifying GeV center measured in sample UU601-1 (4 h annealing at 850 °C, blue dotted line) and corresponding exponential decay fit (red solid line).
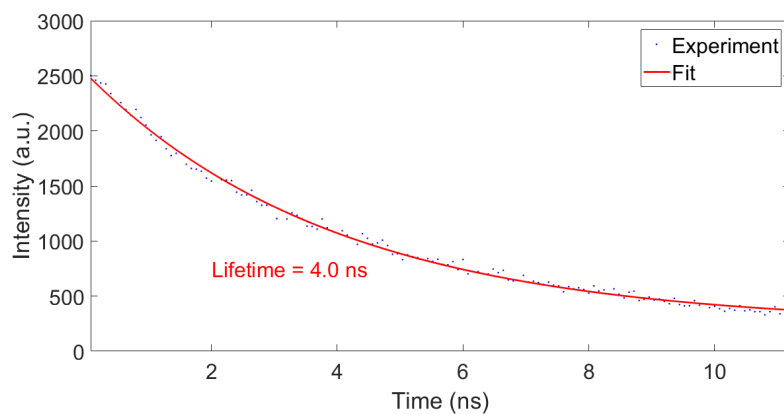
Figure C.2: Lifetime data for one exemplifying GeV center measured in sample UU601-2 (2 h annealing at 1200 °C, blue dotted line) and corresponding exponential decay fit (red solid line).
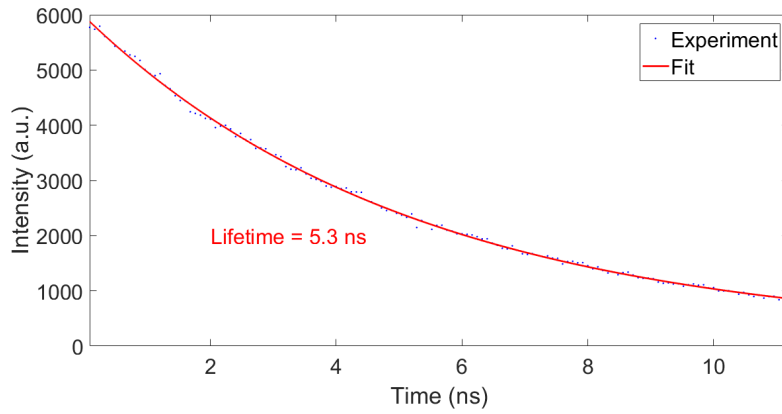
Figure C.3: Lifetime data for one exemplifying GeV center measured in sample UU601-3 (1 h annealing at 1500 °C, blue dotted line) and corresponding exponential decay fit (red solid line).
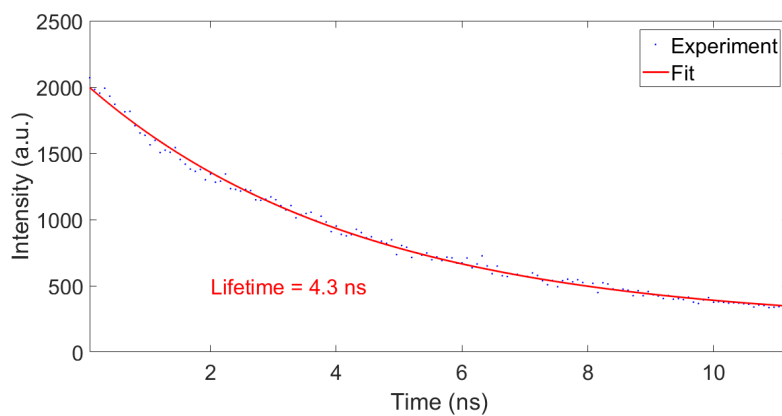
Figure C.4: Lifetime data for one exemplifying GeV center measured in sample UU602-1 (4 h annealing at 850 °C, blue dotted line) and corresponding exponential decay fit (red solid line).
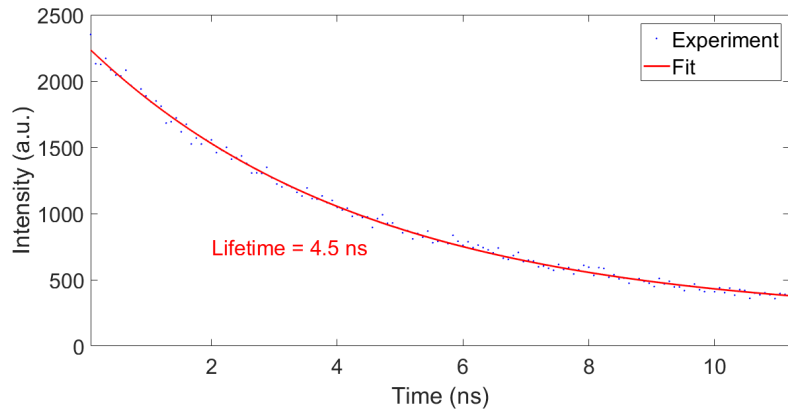
Figure C.5: Lifetime data for one exemplifying GeV center measured in sample UU602-2 (2 h annealing at 1200 °C, blue dotted line) and corresponding exponential decay fit (red solid line).
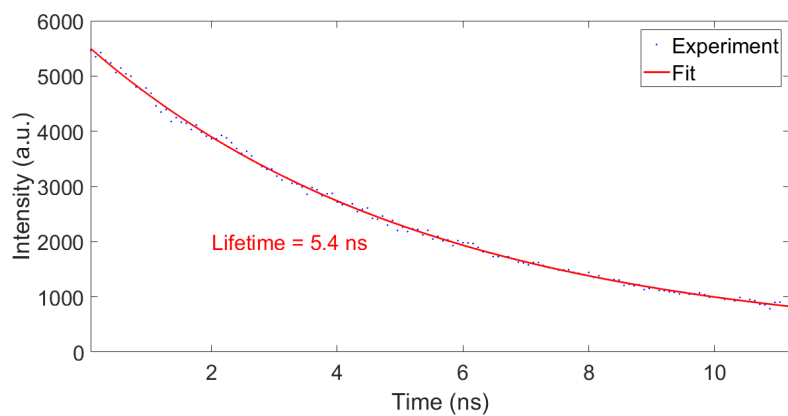
Figure C.6: Lifetime data for one exemplifying GeV center measured in sample UU602-3 (1 h annealing at 1500 °C blue dotted line) and corresponding exponential decay fit (red solid line).

List of Figures

List of Tables

List of Symbols

Variable	Description	SI unit
$\boldsymbol{\sigma}_{\mathrm{P}}$	absorption cross section	m^2
AU	airy unit	m
$\boldsymbol{\omega}$	angular frequency	rads^{-1}
$\boldsymbol{k_B}$	Boltzmann constant	JK^{-1}
T_2	coherence time	s
$\boldsymbol{\Theta}_{\mathrm{D}}$	Debye temperature	K
$\boldsymbol{\alpha}$	Debye-Waller factor	1
$\mathrm{T}_2{}^*$	dephasing time	s
$\boldsymbol{\gamma}_{\mathrm{S}}$	electron gyromagnetic ratio	$\mathrm{rads}^{-1}\mathrm{T}^{-1}$
E	energy	J
T_1	excited state lifetime	s
$\boldsymbol{\Delta}\mathrm{SO}_{\mathrm{e}}$	excited state splitting	Hz
f	focal length	m
$\boldsymbol{\nu}$	frequency	Hz
$\boldsymbol{\Delta}\mathrm{SO}_{\mathrm{g}}$	ground state splitting	Hz
$\boldsymbol{\xi}$	indistinguishability	1
S	integrated absorption	m^{-2}
I	intensity	Wm^{-2}
$\mathbf{B}$	magnetic field	T
$\boldsymbol{\Omega}$	normal mode vibrational frequency	rads^{-1}
N	number density of absorbers	m^{-3}
NA	numerical aperture	1
M	objective magnification	1
$\boldsymbol{\sigma}$	Pauli matrices	1
$\hbar$	Planck reduced constant	Js

Variable	Description	SI unit
P	pressure	Pa
r	radius (pinhole)	m
R_r	recombination rate	m^3s^{-1}
R	reflectivity	1
n	refractive index	1
c	speed of light	ms^{-1}
S	spin operator	Js
T	temperature	K
λ	wavelength	m

Acknowledgements

I want to thank Prof. Fedor Jelezko for giving me the opportunity to carry out my Master's thesis project in the Institute for Quantum Optics of the University of Ulm.

Special thanks to Dr. Lev Kazak. He always provided the perfect working atmosphere. He was always available to discuss any topic and always ready to help. I highly appreciated the discussions on physics, that helped me understand better and improve my research, and the countless hours spent in the lab together.

Special thanks to Katharina Senkalla and Stefan Dietel. They were both always really helpful in solving experimental challenges as well as helping me understand the underlying theoretical concepts.

I also want to thank Dr. Petr Siyushev, Ilia Chuprina, Florian Frank and Prithvi Gundla-palli for fruitfull discussions. Furthermore, I want to thank Jens Fuhrmann for annealing the samples investigated in this thesis and all the members of the Institute for Quantum Optics for their support and the pleasant working environment.

Ringrazio il professor Roberto Osellame per il suo costante supporto durante la realizzazione di questo progetto di tesi.

Ringrazio i miei colleghi e amici dell'università, per aver reso le giornate al Politecnico più belle, leggere e produttive allo stesso tempo.

Ringrazio la mia famiglia, per essere stata sempre al mio fianco nel corso di questi anni universitari. Non ce l'avrei fatta senza il sostegno di voi tutti. Non sarei qui oggi se non fosse per voi. In particolare, ringrazio mamma, papà e Alessandro: grazie per aver creduto in me e nelle mie scelte, grazie per averle sempre supportate.

Ringrazio Pierpaolo, Valentina e tutti i miei amici, per essere stati presenti e per avermi regalato momenti belli anche nei periodi più stressanti o difficili. Grazie, ragazzi, per le risate e le emozioni che mi avete regalato in questi anni. Grazie per tutte le volte che mi avete dato dei consigli, che mi avete ascoltato o che semplicemente mi avete chiesto come fosse stata la mia giornata. Grazie per tutte le volte che abbiamo scherzato insieme e anche per le volte che abbiamo affrontato discorsi seri e mi avete sostenuto.

Ringrazio Paolo, il compagno di viaggio perfetto. Quando tutto questo è iniziato non avrei mai immaginato che sarebbe nato un rapporto di amicizia così bello tra di noi, e questo oggi mi rende ancora più felice e orgoglioso. Quando ripenserò agli anni universitari, per prima cosa non potrò che pensare a te. A tutte le risate, gli scherzi, le uscite, le mangiate, le idee stupide. Ma anche e soprattutto a tutte le volte che ci siamo aiutati e supportati a vicenda, a tutti i discorsi che abbiamo fatto e i consigli che ci siamo dati. Non penserò alle grandi cose, ma a quelle piccole. Grazie per le piccole cose di questi anni, che prese insieme fanno qualcosa di immenso.

Ringrazio zio Tonino, la mia "Roccia". Ti ringrazio per essermi sempre stato vicino e per essere stato ed essere ancora la persona su cui poter sempre fare affidamento, in qualsiasi momento e per qualsiasi motivo. Grazie per avermi sempre sostenuto e incoraggiato. Grazie per tutti i consigli e le dritte che mi hai dato. Grazie anche per aver compreso i miei momenti di difficoltà. Grazie per aver avuto e avere fiducia in me. Soprattutto, grazie per aver sempre creduto in me.